

Identification of b-quark jets with the CMS experiment

This article has been downloaded from IOPscience. Please scroll down to see the full text article.

2013 JINST 8 P04013

(<http://iopscience.iop.org/1748-0221/8/04/P04013>)

View [the table of contents for this issue](#), or go to the [journal homepage](#) for more

Download details:

IP Address: 131.215.71.79

The article was downloaded on 23/05/2013 at 15:18

Please note that [terms and conditions apply](#).

LHC REFERENCE VOLUME

Identification of b-quark jets with the CMS experiment



The CMS collaboration

E-mail: cms-publication-committee-chair@cern.ch

ABSTRACT: At the Large Hadron Collider, the identification of jets originating from b quarks is important for searches for new physics and for measurements of standard model processes. A variety of algorithms has been developed by CMS to select b-quark jets based on variables such as the impact parameters of charged-particle tracks, the properties of reconstructed decay vertices, and the presence or absence of a lepton, or combinations thereof. The performance of these algorithms has been measured using data from proton-proton collisions at the LHC and compared with expectations based on simulation. The data used in this study were recorded in 2011 at $\sqrt{s} = 7$ TeV for a total integrated luminosity of 5.0 fb^{-1} . The efficiency for tagging b-quark jets has been measured in events from multijet and t-quark pair production. CMS has achieved a b-jet tagging efficiency of 85% for a light-parton misidentification probability of 10% in multijet events. For analyses requiring higher purity, a misidentification probability of only 1.5% has been achieved, for a 70% b-jet tagging efficiency.

KEYWORDS: Large detector-systems performance; Pattern recognition, cluster finding, calibration and fitting methods; Performance of High Energy Physics Detectors

ARXIV EPRINT: [1211.4462](https://arxiv.org/abs/1211.4462)



Contents

| | | |
|----------|---|-----------|
| 1 | Introduction | 2 |
| 2 | The CMS detector | 2 |
| 3 | Data samples and simulation | 3 |
| 4 | Algorithms for b-jet identification | 5 |
| 4.1 | Reconstructed objects used in b-jet identification | 5 |
| 4.2 | Identification using track impact parameters | 6 |
| 4.3 | Identification using secondary vertices | 9 |
| 4.4 | Performance of the algorithms in simulation | 10 |
| 4.5 | Impact of running conditions on b-jet identification | 12 |
| 5 | Efficiency measurement with multijet events | 14 |
| 5.1 | Efficiency measurement with kinematic properties of muon jets | 15 |
| 5.2 | Efficiency measurement with the System8 method | 16 |
| 5.3 | Efficiency measurement using a reference lifetime algorithm | 18 |
| 5.4 | Systematic uncertainties on efficiency measurements | 20 |
| 6 | Efficiency measurement with $t\bar{t}$ events | 23 |
| 6.1 | Event selection | 23 |
| 6.2 | Systematic uncertainties | 25 |
| 6.3 | Profile likelihood ratio method | 27 |
| 6.4 | Flavour tag consistency method | 29 |
| 6.5 | Flavour tag matching method | 31 |
| 6.6 | Efficiency measurement from a b-enriched jet sample | 33 |
| 7 | Efficiency measurement results | 35 |
| 7.1 | Results from multijet events | 35 |
| 7.2 | Results from $t\bar{t}$ events | 38 |
| 7.3 | Comparison of results | 40 |
| 8 | Misidentification probability measurement | 40 |
| 9 | Conclusions | 46 |
| | The CMS collaboration | 52 |

1 Introduction

Jets that arise from bottom-quark hadronization (b jets) are present in many physics processes, such as the decay of top quarks, the Higgs boson, and various new particles predicted by supersymmetric models. The ability to accurately identify b jets is crucial in reducing the otherwise overwhelming background to these channels from processes involving jets from gluons (g) and light-flavour quarks (u, d, s), and from c-quark fragmentation.

The properties of the bottom and, to a lesser extent, the charm hadrons can be used to identify the hadronic jets into which the b and c quarks fragment. These hadrons have relatively large masses, long lifetimes and daughter particles with hard momentum spectra. Their semileptonic decays can be exploited as well. The Compact Muon Solenoid (CMS) detector, with its precise charged-particle tracking and robust lepton identification systems, is well matched to the task of b-jet identification (b-jet tagging). The first physics results using b-jet tagging have been published [1–3] from the first data samples collected at the Large Hadron Collider (LHC).

This paper describes the b-jet tagging algorithms used by the CMS experiment and measurements of their performance. A description of the apparatus is given in section 2. The event samples and simulation are discussed in section 3. The algorithms for b-jet tagging are defined in section 4. The distributions of the relevant observables are compared between simulation and proton-proton collision data collected in 2011 at a centre-of-mass energy of 7 TeV. The robustness of the algorithms with respect to running conditions, such as the alignment of the detector elements and the presence of additional collisions in the same bunch crossing (pileup), is also discussed.

Physics analyses using b-jet identification require the values of the efficiency and misidentification probability of the chosen algorithm, and, in general, these are a function of the transverse momentum (p_T) and pseudorapidity (η) of a jet. They can also depend on parameters such as the efficiency of the track reconstruction, the resolution of the reconstructed track parameters, or the track density in a jet. While the CMS simulation reproduces the performance of the detector to a high degree of precision, it is difficult to model all the parameters relevant for b-jet tagging. Therefore it is essential to measure the performance of the algorithms directly from data. These measurements are performed with jet samples that are enriched in b jets, either chosen by applying a discriminating variable on jets in multijet events or by selecting jets from top-quark decays. The methods that are used to measure the performance are described in sections 5 and 6. The measurements are complementary: multijet events cover a wider range in p_T , while the results obtained from $t\bar{t}$ events are best suited for some studies of top-quark physics. The efficiency measurements are summarized and compared in section 7. The measurement of the misidentification probability of light-parton (u, d, s, g) jets as b jets in the data is presented in section 8.

2 The CMS detector

The central feature of the CMS apparatus is a superconducting solenoid, of 6 m internal diameter, which provides a magnetic field of 3.8 T. Within the field volume are the silicon tracker, the crystal electromagnetic calorimeter, and the brass/scintillator hadron calorimeter. Muons are measured in gas-ionization detectors embedded in the steel return yoke.

CMS uses a right-handed coordinate system, with the origin at the nominal interaction point, the x axis pointing to the centre of the LHC ring and the z axis along the counterclockwise-beam direction. The polar angle, θ , is measured from the positive z axis and the azimuthal angle, ϕ , is measured in the x - y plane. The pseudorapidity is defined as $\eta \equiv -\ln[\tan(\theta/2)]$. A more detailed description of the CMS detector can be found elsewhere [4].

The most relevant detector elements for the identification of b jets and the measurement of algorithm performance are the tracking system and the muon detectors. The inner tracker consists of 1440 silicon pixel and 15 148 silicon strip detector modules. It measures charged particles up to a pseudorapidity of $|\eta| < 2.5$. The pixel modules are arranged in three cylindrical layers in the central part of CMS and two endcap disks on each side of the interaction point. The silicon strip detector comprises two cylindrical barrel detectors with a total of 10 layers and two endcap systems with a total of 12 layers at each end of CMS. The tracking system provides an impact parameter (IP) resolution of about 15 (30) μm at a p_T of 100 (5) GeV/c . In comparison typical IP values for tracks from b -hadron decays are at the level of a few 100 μm . Muons are measured and identified in detection layers that use three technologies: drift tubes, cathode-strip chambers, and resistive-plate chambers. The muon system covers the pseudorapidity range $|\eta| < 2.4$. The combination of the muon and tracking systems yields muon candidates of high purity with a p_T resolution of about 1 to 3%, for p_T values from 5 to 100 GeV/c .

3 Data samples and simulation

Samples of inclusive multijet events for the measurement of efficiencies and misidentification probabilities were collected using jet triggers with p_T thresholds of 30 to 300 GeV/c . For efficiency measurements, dedicated triggers were used to enrich the data sample with jets from semimuonic b -hadron decays. These triggers required the presence of at least two jets with p_T thresholds ranging from 20 to 110 GeV/c . One of these jets was required to include a muon with $p_T > 5 \text{ GeV}/c$ within a cone of $\Delta R = 0.4$ around the jet axis, where ΔR is defined as $\sqrt{(\Delta\phi)^2 + (\Delta\eta)^2}$. Triggers with low- p_T thresholds were prescaled in order to limit the overall trigger rates. Depending on the prescale applied to the trigger, the multijet analyses used datasets with integrated luminosities of up to 5.0 fb^{-1} .

Data for the analysis of $t\bar{t}$ events were collected with single- (e or μ) and double-lepton (ee or $e\mu$ or $\mu\mu$) triggers. The samples were collected in the first part of the 2011 data taking with an integrated luminosity of 2.3 fb^{-1} . The precision on the b -jet tagging efficiency from $t\bar{t}$ events is limited by systematic uncertainties. Using the full dataset collected in 2011 would not significantly reduce the overall uncertainty.

Monte Carlo (MC) simulated samples of multijet events were generated with PYTHIA 6.424 [5] using the Z2 tune [6]. For b -jet tagging efficiency studies, dedicated multijet samples have been produced with the explicit requirement of a muon in the final state.

In the simulation, a reconstructed jet is matched with a generated parton if the direction of the parton is within a cone of radius $\Delta R = 0.3$ around the jet axis. The jet is then assigned the flavour of the parton. Should more than one parton be matched to a given jet, the flavour assigned is that of the heaviest parton. The b flavour is given priority over the c flavour, which in turn is given priority

over light partons. According to this definition jets originating from gluon splitting to $b\bar{b}$, which constitute an irreducible background for all tagging algorithms, are classified as b jets.

Events involving $t\bar{t}$ production were simulated using the MADGRAPH [7] event generator (v. 5.1.1.0), where the top quark pairs were generated with up to four additional partons in the final state. A top quark mass of $m_t = 172.5 \text{ GeV}/c^2$ was assumed. The parton configurations generated by MADGRAPH were processed with PYTHIA to provide showering of the generated particles. The soft radiation was matched with the contributions from the matrix element computation using the k_T -MLM prescription [8]. The tau-lepton decays were handled with TAUOLA (v. 27.121.5) [9].

The electroweak production of single top quarks is considered as a background process for analyses using $t\bar{t}$ events, and was simulated using POWHEG 301 [10]. The production of $W/Z + \text{jets}$ events, where the vector boson decays leptonically, has a signature similar to $t\bar{t}$ and constitutes the main background. These events were simulated using MADGRAPH + PYTHIA, with up to four additional partons in the final state. The bottom and charm components are separated from the light-parton components in the analysis by matching reconstructed jets to partons in the simulation.

Signal and background processes used in the analysis of $t\bar{t}$ events were normalized to next-to-leading-order (NLO) and next-to-next-to-leading-order (NNLO) cross sections, with the exception of the QCD background.

The top-quark pair production NLO cross section was calculated to be $\sigma_{t\bar{t}} = 157_{-24}^{+23} \text{ pb}$, using MCFM [11]. The uncertainty in this cross section includes the scale uncertainties, estimated by varying simultaneously the factorization and renormalization scales by factors of 0.5 or 2 with respect to the nominal scale of $(2m_t)^2 + (\sum p_T^{\text{parton}})^2$, where p_T^{parton} are the transverse momenta of the partons in the event. The uncertainties from the parton distribution functions (PDF) and the value of the strong coupling constant α_s were estimated following the procedures from the MSTW2008 [12], CTEQ6.6 [13], and NNPDF2.0 [14] sets. The uncertainties were then combined according to the PDF4LHC prescriptions [15].

The t -channel single top NLO cross section was calculated to be $\sigma_t = 64.6_{-3.2}^{+3.4} \text{ pb}$ using MCFM [11, 16–18]. The uncertainty was evaluated in the same way as for top-quark pair production. The single top-quark associated production (tW) cross section was set to $\sigma_{tW} = 15.7 \pm 1.2 \text{ pb}$ [19]. The s -channel single top-quark next-to-next-to-leading-log (NNLL) cross section was determined to be $\sigma_s = 4.6 \pm 0.1 \text{ pb}$ [20].

The NNLO cross section of the inclusive production of W bosons multiplied by its branching fraction to leptons was determined to be $\sigma_{W \rightarrow \ell\nu} = 31.3 \pm 1.6 \text{ nb}$ using FEWZ [21], setting the renormalization and factorization scales to $(m_W)^2 + (\sum p_T^{\text{jet}})^2$ with $m_W = 80.398 \text{ GeV}/c^2$. The uncertainty was determined in the same way as in top-quark pair production. The normalizations of the $W+b$ jets and $W+c$ jets components were determined in a measurement of the top pair production cross section in the lepton+jet channel [1], where a simultaneous fit of the $t\bar{t}$ cross section and the normalization of the main backgrounds was performed.

The Drell–Yan production cross section at NNLO was calculated using FEWZ as $\sigma_{Z/\gamma^* \rightarrow \ell\ell}(m_{\ell\ell} > 20 \text{ GeV}) = 5.00 \pm 0.27 \text{ nb}$, where $m_{\ell\ell}$ is the invariant mass of the two leptons and the scales were set using the Z boson mass $m_Z = 91.1876 \text{ GeV}/c^2$ [22].

All generated events were passed through the full simulation of the CMS detector based on GEANT4 [23]. The samples were generated with a different pileup distribution than that observed in the data. The simulated events were therefore reweighted to match the observed pileup distribution.

4 Algorithms for b-jet identification

A variety of reconstructed objects — tracks, vertices and identified leptons — can be used to build observables that discriminate between b and light-parton jets. Several simple and robust algorithms use just a single observable, while others combine several of these objects to achieve a higher discrimination power. Each of these algorithms yields a single discriminator value for each jet. The minimum thresholds on these discriminators define loose (“L”), medium (“M”), and tight (“T”) operating points with a misidentification probability for light-parton jets of close to 10%, 1%, and 0.1%, respectively, at an average jet p_T of about 80 GeV/c. Throughout this paper, the tagging criteria will be labelled with the letter characterizing the operating point appended to the acronym of one of the algorithms described in sections 4.2 and 4.3. The application of such a tagging criterion will be called a “tagger”.

After a short description of the reconstructed objects used as inputs, details on the tagging algorithms are given in the following subsections, proceeding in order of increasing complexity. Muon-based b-jet identification is mainly used as a reference method for performance measurements. It is described in more detail in section 5.

4.1 Reconstructed objects used in b-jet identification

Jets are clustered from objects reconstructed by the particle-flow algorithm [24, 25]. This algorithm combines information from all subdetectors to create a consistent set of reconstructed particles for each event. The particles are then clustered into jets using the anti- k_T clustering algorithm [26] with a distance parameter of 0.5. The raw jet energies are corrected to obtain a uniform response in η and an absolute calibration in p_T [27]. Although particle-flow jets are used as the default, the b-jet tagging algorithms can be applied to jets clustered from other reconstructed objects.

Each algorithm described in the next section uses the measured kinematic properties of charged particles, including identified leptons, in a jet. The trajectories of these particles are reconstructed in the CMS tracking system in an iterative procedure using a standard Kalman filter-based method. Details on the pattern recognition, the track-parameter estimation, and the tracking performance in proton-proton collisions can be found in refs. [4, 28].

A “global” muon reconstruction, using information from multiple detector systems, is achieved by first reconstructing a muon track in the muon chambers. This is then matched to a track measured in the silicon tracker [29]. A refit is then performed using the measurements on both tracks.

Primary vertex candidates are selected by clustering reconstructed tracks based on the z coordinate of their closest approach to the beam line. An adaptive vertex fit [30] is then used to estimate the vertex position using a sample of tracks compatible with originating from the interaction region. Among the primary vertices found in this way, the one with the highest $\sum (p_T^{\text{track}})^2$ is selected as a candidate for the origin of the hard interaction, where the p_T^{track} are the transverse momenta of the tracks associated to the vertex.

The b-jet tagging algorithms require a sample of well-reconstructed tracks of high purity. Specific requirements are imposed in addition to the selection applied in the tracking step. The fraction of misreconstructed or poorly reconstructed tracks is reduced by requiring a transverse momentum of at least 1 GeV/c. At least eight hits must be associated with the track. To ensure a good fit, $\chi^2/\text{n.d.o.f.} < 5$ is required, where n.d.o.f. stands for the number of degrees of freedom in

the fit. At least two hits are required in the pixel system since track measurements in the innermost layers provide most of the discriminating power. A loose selection on the track impact parameters is used to further increase the fraction of well-reconstructed tracks and to reduce the contamination by decay products of long-lived particles, e.g. neutral kaons. The impact parameters d_{xy} and d_z are defined as the transverse and longitudinal distance to the primary vertex at the point of closest approach in the transverse plane. Their absolute values must be smaller than 0.2 cm and 17 cm, respectively. Tracks are associated to jets in a cone $\Delta R < 0.5$ around the jet axis, where the jet axis is defined by the primary vertex and the direction of the jet momentum. The distance of a track to the jet axis is defined as the distance of closest approach of the track to the axis. In order to reject tracks from pileup this quantity is required to be less than $700 \mu\text{m}$. The point of closest approach must be within 5 cm of the primary vertex. This sample of associated tracks is the basis for all algorithms that use impact parameters for discrimination.

Properties of the tracks and the average multiplicity after the selection (except for the variable plotted) are shown in figure 1. The uncertainties shown in this and all following figures are statistical unless otherwise stated. The data were recorded with a prescaled jet trigger in the second part of 2011 when the number of pileup events was highest. The jet p_T threshold was 60 GeV/c. The distributions show satisfactory agreement with the expectations from simulation. The track multiplicity and the lower part of the momentum spectrum are particularly sensitive to the modelling of the particle multiplicity and kinematics by the Monte Carlo generator, as are other distributions such as the number of hits in the innermost pixel layers. Detector effects that are not modelled by the simulation, such as the dynamic readout inefficiency in the pixel system, can also contribute to the remaining discrepancies. In figure 1 and the following figures, simulated events with gluon splitting to $b\bar{b}$ are shown as a special category. The b jets in these events tend to be close in space and can be inadvertently merged by the clustering algorithm, resulting in a higher average track multiplicity per jet.

The combinatorial complexity of the reconstruction of the decay points (secondary vertices) of b or c hadrons is more challenging in the presence of multiple proton-proton interactions. In order to minimize this complexity a different track selection is applied. Tracks must be within a cone of $\Delta R = 0.3$ around the jet axis with a maximal distance to this axis of 0.2 cm and pass a “high-purity” criterion [28]. The “high-purity” criterion uses the normalized χ^2 of the track fit, the track length, and impact parameter information to optimize the purity for each of the iterations in track reconstruction. The vertex finding procedure begins with tracks defined by this selection and proceeds iteratively. A vertex candidate is identified by applying an adaptive vertex fit [30], which is robust in the presence of outliers. The fit estimates the vertex position and assigns a weight between 0 and 1 to each track based on its compatibility with the vertex. All tracks with weights > 0.5 are then removed from the sample. The fit procedure is repeated until no new vertex candidate can be found. In the first iteration the interaction region is used as a constraint in order to identify the prompt tracks in the jet. The subsequent iterations produce decay vertex candidates.

4.2 Identification using track impact parameters

The impact parameter of a track with respect to the primary vertex can be used to distinguish the decay products of a b hadron from prompt tracks. The IP is calculated in three dimensions by taking advantage of the excellent resolution of the pixel detector along the z axis. The impact parameter has the same sign as the scalar product of the vector pointing from the primary vertex to the point

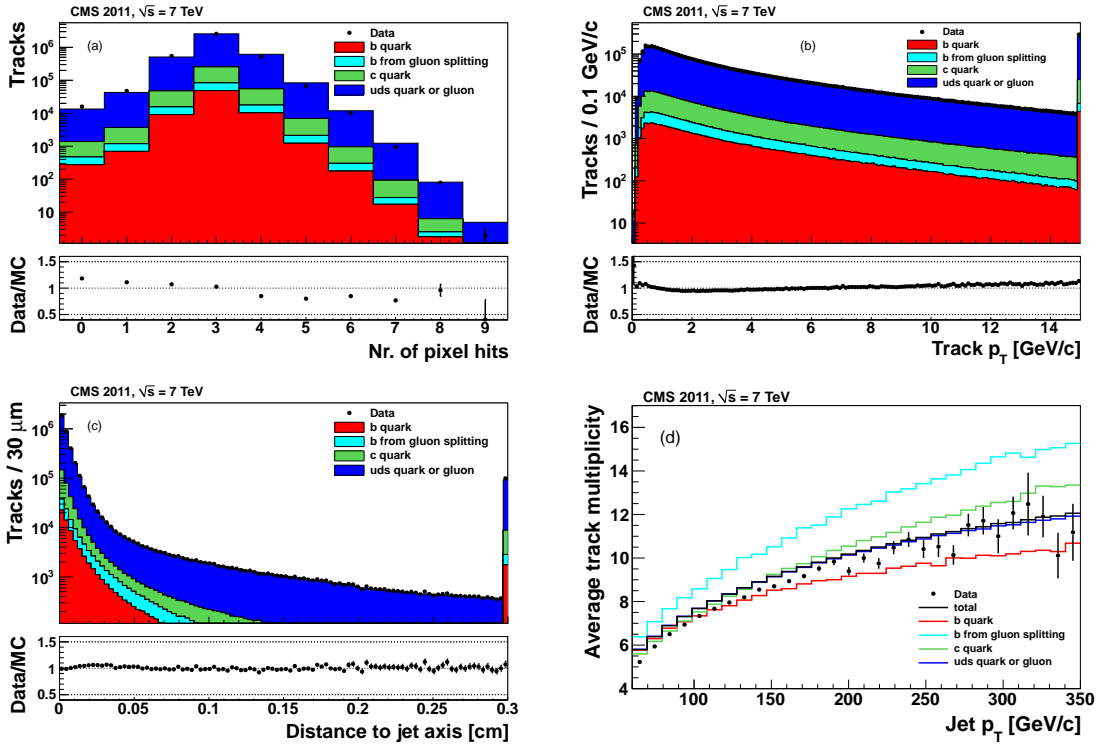


Figure 1. Track properties after basic selection (except for the variable plotted): (a) number of hits in the pixel system, (b) transverse momentum, (c) distance to the jet axis. The average number of tracks passing the basic selection is shown in (d) as a function of the transverse momentum of the jet. In (a)–(c) the distributions from simulation have been normalized to match the counts in data. The filled circles correspond to data. The stacked, coloured histograms indicate the contributions of different components from simulated multijet (“QCD”) samples. Simulated events involving gluon splitting to b quarks (“b from gluon splitting”) are indicated separately from the other b production processes (“b quark”). In each histogram, the rightmost bin includes all events from the overflow. The sample corresponds to a trigger selection with jet $p_T > 60 \text{ GeV}/c$.

of closest approach with the jet direction. Tracks originating from the decay of particles travelling along the jet axis will tend to have positive IP values. In contrast, the impact parameters of prompt tracks can have positive or negative IP values. The resolution of the impact parameter depends strongly on the p_T and η of a track. The impact parameter significance S_{IP} , defined as the ratio of the IP to its estimated uncertainty, is used as an observable. The distributions of IP values and their significance are shown in figure 2. In general, good agreement with simulation is observed with the exception of a small difference in the width of the core of the IP significance distribution.

By itself the impact parameter significance has discriminating power between the decay products of b and non-b jets. The *Track Counting* (TC) algorithm sorts tracks in a jet by decreasing values of the IP significance. Although the ranking tends to bias the values for the first track to high positive IP significances, the probability to have several tracks with high positive values is low for light-parton jets. Therefore the two different versions of the algorithm use the IP significance of the second and third ranked track as the discriminator value. These two versions of the algorithm are called *Track Counting High Efficiency* (TCHE) and *Track Counting High Purity* (TCHP), respectively. The distribution of the TCHE discriminator is shown in figure 3 (a).

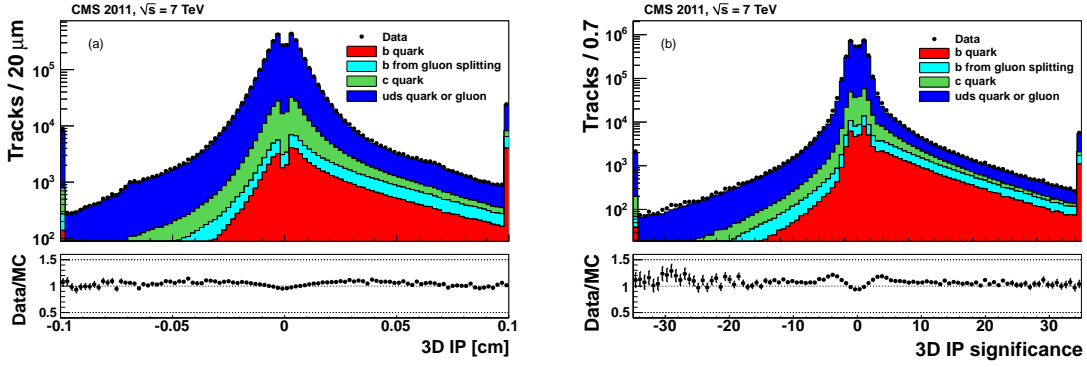


Figure 2. Distributions of (a) the 3D impact parameter and (b) the significance of the 3D impact parameter for all selected tracks. Selection and symbols are the same as in figure 1. Underflow and overflow are added to the first and last bins, respectively.

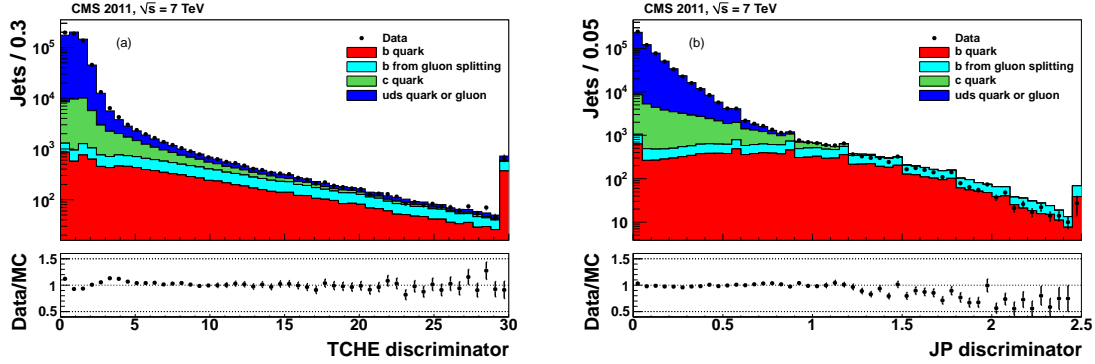


Figure 3. Discriminator values for (a) the TCHE and (b) the JP algorithms. Selection and symbols are the same as in figure 1. The small discontinuities in the JP distributions are due to the single track probabilities which are required to be greater than 0.5%.

A natural extension of the TC algorithms is the combination of the IP information of several tracks in a jet. Two discriminators are computed from additional algorithms. The *Jet Probability* (JP) algorithm uses an estimate of the likelihood that all tracks associated to the jet come from the primary vertex. The *Jet B Probability* (JBP) algorithm gives more weight to the tracks with the highest IP significance, up to a maximum of four such tracks, which matches the average number of reconstructed charged particles from b-hadron decays. The estimate for the likelihood, P_{jet} , is defined as

$$P_{\text{jet}} = \Pi \cdot \sum_{i=0}^{N-1} \frac{(-\ln \Pi)^i}{i!} \quad \text{with} \quad \Pi = \prod_{i=1}^N \max(P_i, 0.005), \quad (4.1)$$

where N is the number of tracks under consideration and P_i is the estimated probability for track i to come from the primary vertex [31, 32]. The P_i are based on the probability density functions for the IP significance of prompt tracks. These functions are extracted from data for different track quality classes, using the shape of the negative part of the S_{IP} distribution. Eight quality classes are defined for tracks with $\chi^2/\text{n.d.o.f} < 2.5$, depending on the momentum (< 8 or $> 8 \text{ GeV}/c$) and

pseudorapidity ($|\eta|$ within 0-0.8, 0.-1.6, 1.6-2.4 if there are at least three pixel hits or $|\eta| < 2.4$ if there are only two pixel hits). A ninth quality class is defined for tracks with $\chi^2/\text{n.d.o.f} > 2.5$. The cut-off parameter for P_i at 0.5% limits the effect of single, poorly reconstructed tracks on the global estimate. The discriminators for the jet probability algorithms have been constructed to be proportional to $-\ln P_{\text{jet}}$. The distribution of the JP discriminator in data and simulation is shown in figure 3 (b).

4.3 Identification using secondary vertices

The presence of a secondary vertex and the kinematic variables associated with this vertex can be used to discriminate between b and non-b jets. Two of these variables are the flight distance and direction, using the vector between primary and secondary vertices. The other variables are related to various properties of the system of associated secondary tracks such as the multiplicity, the mass (assuming the pion mass for all secondary tracks), or the energy. Secondary-vertex candidates must meet the following requirements to enhance the b purity:

- secondary vertices must share less than 65% of their associated tracks with the primary vertex and the significance of the radial distance between the two vertices has to exceed 3σ ;
- secondary vertex candidates with a radial distance of more than 2.5 cm with respect to the primary vertex, with masses compatible with the mass of K^0 or exceeding $6.5 \text{ GeV}/c^2$ are rejected, reducing the contamination by vertices corresponding to the interactions of particles with the detector material and by decays of long-lived mesons;
- the flight direction of each candidate has to be within a cone of $\Delta R < 0.5$ around the jet direction.

The *Simple Secondary Vertex* (SSV) algorithms use the significance of the flight distance (the ratio of the flight distance to its estimated uncertainty) as the discriminating variable. The algorithms' efficiencies are limited by the secondary vertex reconstruction efficiency to about 65%. Similar to the *Track Counting* algorithms, there exist two versions optimized for different purity: the *High Efficiency* (SSVHE) version uses vertices with at least two associated tracks, while for the *High Purity* (SSVHP) version at least three tracks are required. In figure 4 the flight distance significance and the mass associated with the secondary vertex are shown.

A more complex approach involves the use of secondary vertices, together with track-based lifetime information. By using these additional variables, the *Combined Secondary Vertex* (CSV) algorithm provides discrimination also in cases when no secondary vertices are found, increasing the maximum efficiency with respect to the SSV algorithms. In many cases, tracks with an $S_{\text{IP}} > 2$ can be combined in a “pseudo vertex”, allowing for the computation of a subset of secondary-vertex-based quantities even without an actual vertex fit. When even this is not possible, a “no vertex” category reverts to track-based variables that are combined in a way similar to that of the JP algorithm.

The following set of variables with high discriminating power and low correlations is used (in the “no vertex” category only the last two variables are available):

- the vertex category (real, “pseudo,” or “no vertex”);

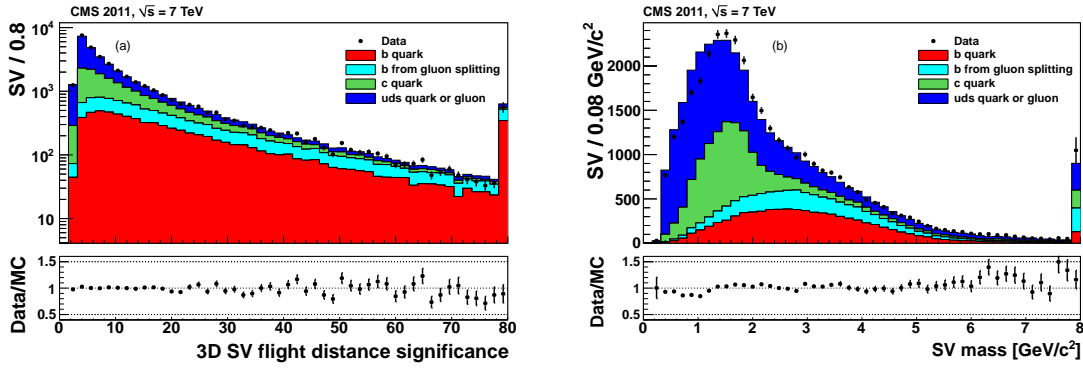


Figure 4. Properties of reconstructed decay vertices: (a) the significance of the 3D secondary vertex (3D SV) flight distance and (b) the mass associated with the secondary vertex. Selection and symbols are the same as in figure 1.

- the flight distance significance in the transverse plane (“2D”);
- the vertex mass;
- the number of tracks at the vertex;
- the ratio of the energy carried by tracks at the vertex with respect to all tracks in the jet;
- the pseudorapidities of the tracks at the vertex with respect to the jet axis;
- the 2D IP significance of the first track that raises the invariant mass above the charm threshold of $1.5 \text{ GeV}/c^2$ (tracks are ordered by decreasing IP significance and the mass of the system is recalculated after adding each track);
- the number of tracks in the jet;
- the 3D IP significances for each track in the jet.

Two likelihood ratios are built from these variables. They are used to discriminate between b and c jets and between b and light-parton jets. They are combined with prior weights of 0.25 and 0.75, respectively. The distributions of the vertex multiplicity and of the CSV discriminator are presented in figure 5.

4.4 Performance of the algorithms in simulation

The performance of the algorithms described above is summarized in figure 6 where the predictions of the simulation for the misidentification probabilities (the efficiencies to tag non-b jets) are shown as a function of the b-jet efficiencies. Jets with $p_T > 60 \text{ GeV}/c$ in a sample of simulated multijet events are used to obtain the efficiencies and misidentification probabilities. For loose selections with 10% misidentification probability for light-parton jets a b-jet tagging efficiency of $\sim 80\text{--}85\%$ is achieved. In this region the JBP has the highest b-jet tagging efficiency. For tight selections with misidentification probabilities of 0.1%, the typical b-jet tagging efficiency values are $\sim 45\text{--}55\%$. For medium and tight selections the CSV algorithm shows the best performance. As can be seen in

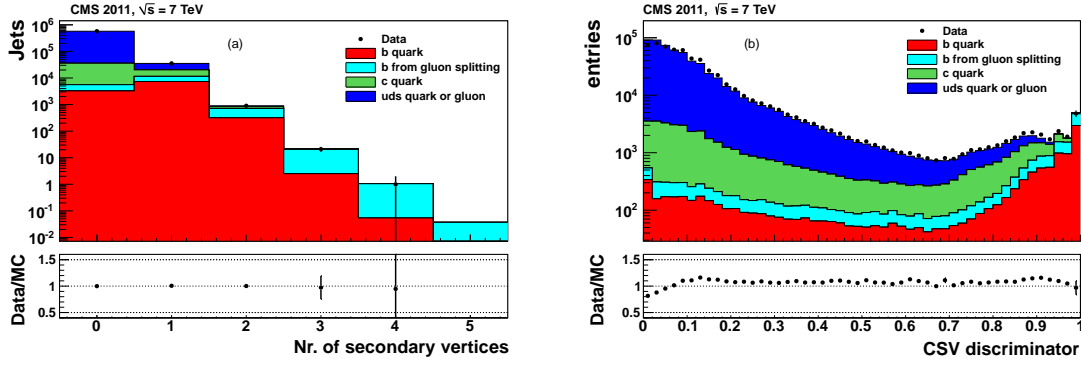


Figure 5. Distributions of (a) the secondary vertex multiplicity and (b) the CSV discriminator. Selection and symbols are the same as in figure 1.

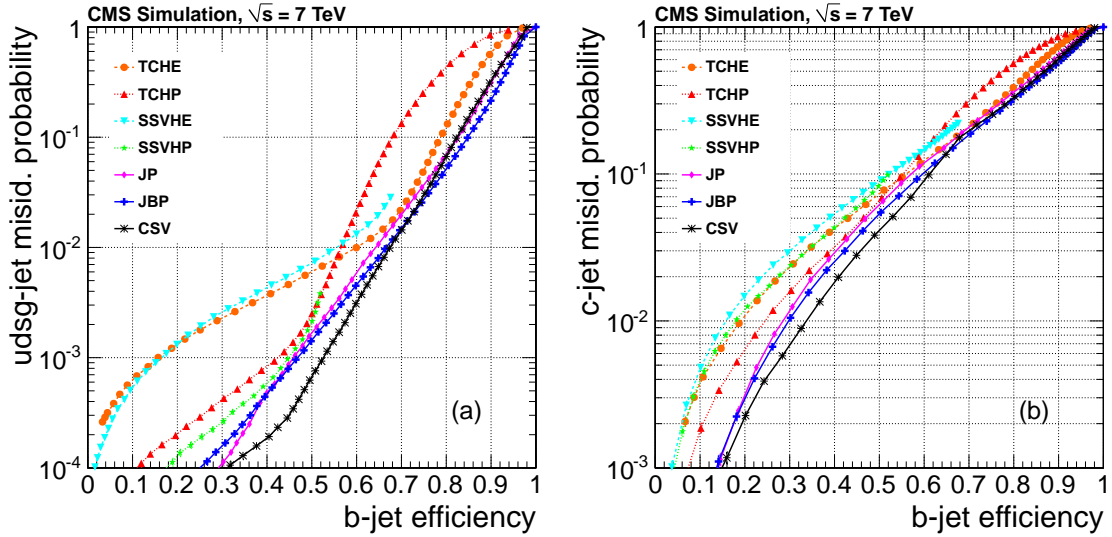


Figure 6. Performance curves obtained from simulation for the algorithms described in the text. (a) light-parton- and (b) c-jet misidentification probabilities as a function of the b-jet efficiency. Jets with $p_T > 60 \text{ GeV}/c$ in a sample of simulated multijet events are used to obtain the efficiency and misidentification probability values.

figure 6, the TC and SSV algorithms cannot be tuned to provide good performance for the whole range of operating points. Therefore two versions of these algorithms are provided, with the “high efficiency” version to be used for loose to medium operating points and the “high purity” version for tighter selections. Because of the non-negligible lifetime of c hadrons the separation of c from b jets is naturally more challenging. Due to the explicit tuning of the CSV algorithm for light-parton- and c-jet rejection it provides the best c-jet rejection values in the high-purity region.

Figure 7 presents the efficiencies and misidentification probabilities as a function of jet p_T and pseudorapidity for the JPL and CSVM taggers. Two simulated samples are used: a QCD multijet sample with a jet p_T trigger threshold of $60 \text{ GeV}/c$ applied to the leading jet, and a $t\bar{t}$ sample. Jets with $p_T > 30 \text{ GeV}/c$ and $|\eta| < 2.4$ are considered in both cases. The b-jet identification efficiency

is slightly larger in $t\bar{t}$ events at small jet p_T ($< 100 \text{ GeV}/c$) due to the presence of more central jets. At large jet p_T ($> 200 \text{ GeV}/c$), the presence of b and c jets from gluon splitting explains the apparent higher identification efficiency in the QCD multijet sample. The b-jet efficiency and the c-jet misidentification probability rise with jet p_T for values below $100 \text{ GeV}/c$ and decrease above $200 \text{ GeV}/c$. This dependence is due to a convolution of the track impact parameter resolution (which is larger at low p_T), of the heavy-hadron decay lengths (which scale with jet p_T) and of the track-selection criteria. The misidentification probability for light-parton jets rises continuously with jet p_T due to the logarithmic increase of the number of particles in jets and the higher fraction of merged hits in the innermost layers of the tracking system. However, both the identification efficiencies and misidentification probabilities stay roughly constant over most of the pixel detector acceptance.

4.5 Impact of running conditions on b-jet identification

All tagging algorithms rely on a high track identification efficiency and a reliable estimation of the track parameters and their uncertainties. These are both potentially sensitive to changes in the running conditions of the experiment. The robustness of the algorithms with respect to the misalignment of the tracking system and an increase in the density of tracks due to pile up, which are the most important of the changes in conditions, has been studied.

The alignment of the CMS tracker is performed using a mixture of tracks from cosmic rays and minimum bias collisions [33, 34], and is regularly monitored. During the 2011 data taking, the most significant movements were between the two halves of the pixel barrel detector, where discrete changes in the relative z position of up to $30 \mu\text{m}$ were observed. The sensitivity of b-jet identification to misalignment was studied on simulated $t\bar{t}$ samples. With the current estimated accuracy of the positions of the active elements, no significant deterioration is observed with respect to a perfectly aligned detector. The effect of displacements between the two parts of the pixel barrel detector was studied by introducing artificial separations of 40, 80, 120, and $160 \mu\text{m}$ in the detector simulation. The movements observed in 2011 were not found to cause any significant degradation of the performance.

Because of the luminosity profile of the 2011 data, the number of proton collisions taking place simultaneously in one bunch crossing was of the order of 5 to 20 depending on the time period. Although these additional collisions increase the total number of tracks in the event, the track selection is able to reject tracks from nearby primary vertices. The multiplicity distribution of selected tracks is almost independent of the number of primary vertices, as shown in figure 8 (a). There is an indication of a slightly lower tracking efficiency in events with high pileup. The rejection of the additional tracks is mainly due to the requirement on the distance of the tracks with respect to the jet axis. This selection criterion is very efficient for the rejection of tracks from pileup. The reconstruction of track parameters is hardly affected. The distribution of the second-highest IP significance is stable, as shown in figure 8 (b). The impact of high pileup on the b-jet tagging performance is illustrated in figure 9. This shows the light-parton misidentification probability versus the b-jet tagging efficiency for the TCHP and SSVHP algorithms. In order to focus on the changes due to the b-jet tagging algorithms, the performance curves have been compared using a jet p_T threshold of $60 \text{ GeV}/c$ at the generator level. The changes are small and concentrated in the regions of very high purity.

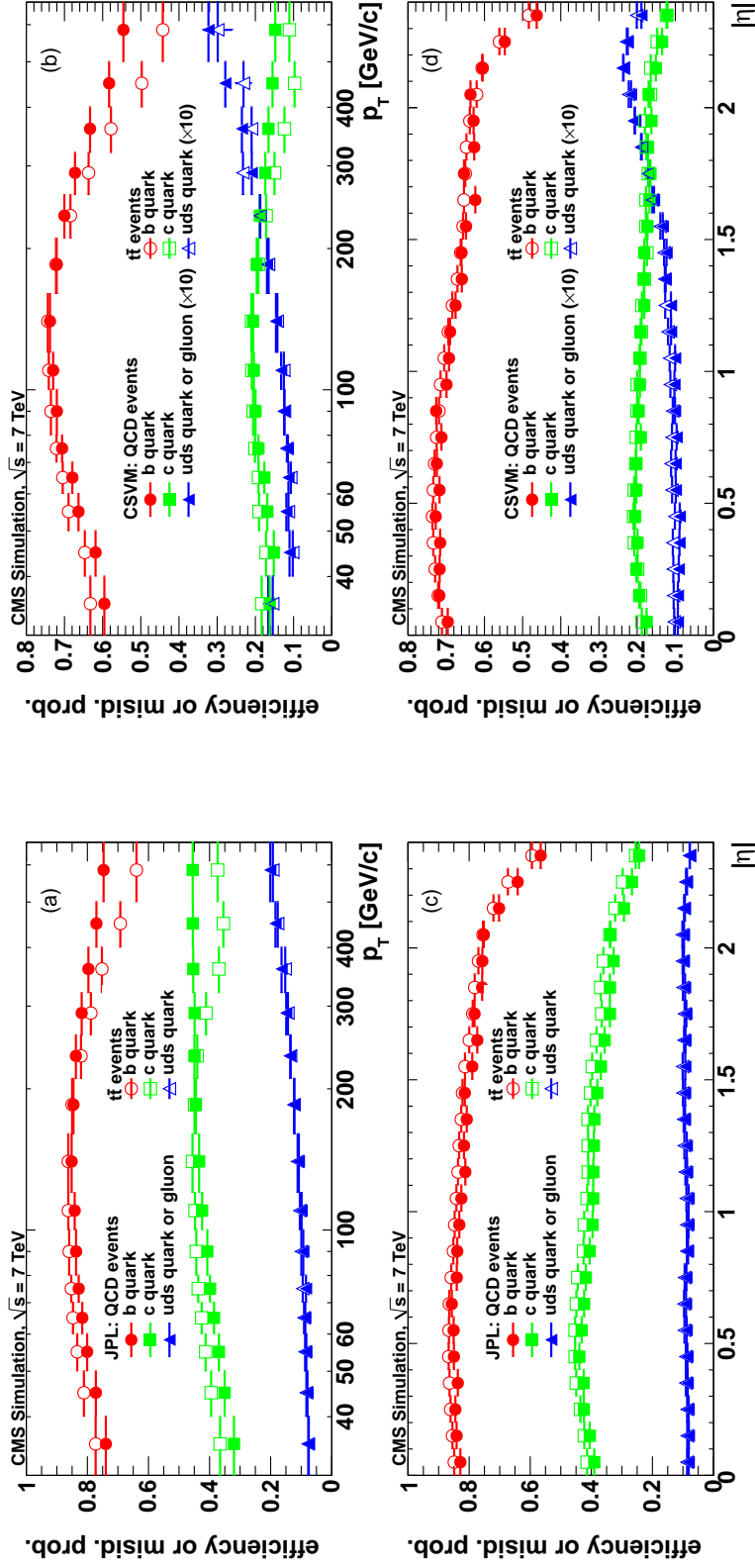


Figure 7. Efficiency for b-jets and misidentification probabilities for c and light-parton jets of the (a, c) JPL and (b, d) CSV taggers as a function of (a, b) jet p_T and (c, d) jet pseudorapidity in QCD multijet events and $t\bar{t}$ events (open symbols). A trigger threshold of $p_T > 60 \text{ GeV}/c$ is applied to the leading jet in the QCD events. Jets with $p_T > 30 \text{ GeV}/c$ and $|\eta| < 2.4$ are used in both samples. In (a) and (b), the rightmost bins include all jets with $p_T > 500 \text{ GeV}/c$. For the CSV tagger, the misidentification probability for light partons is scaled up by a factor of ten.

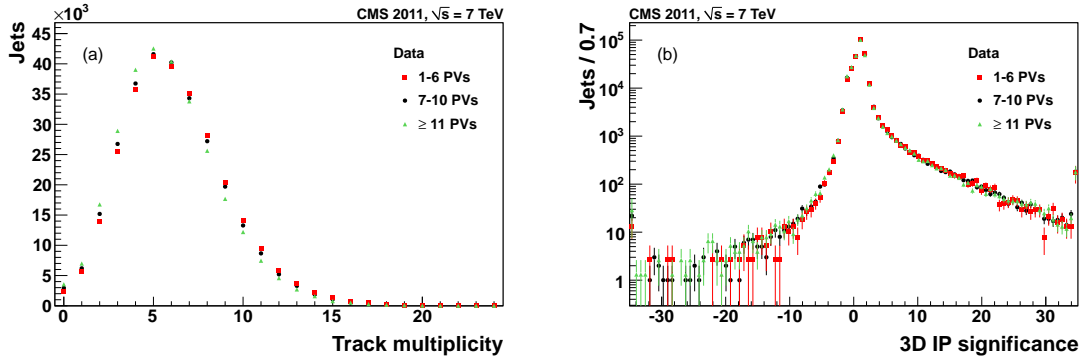


Figure 8. (a) the number of tracks associated with the selected jets for three ranges of primary vertex (PV) multiplicity. (b) the IP significance of the second-most significant track, for the three ranges of primary vertex multiplicity. The selection is the same as in figure 1. The distributions are normalized to the event count for 1–6 PV range. Underflow and overflow entries are added to the first and last bins, respectively.

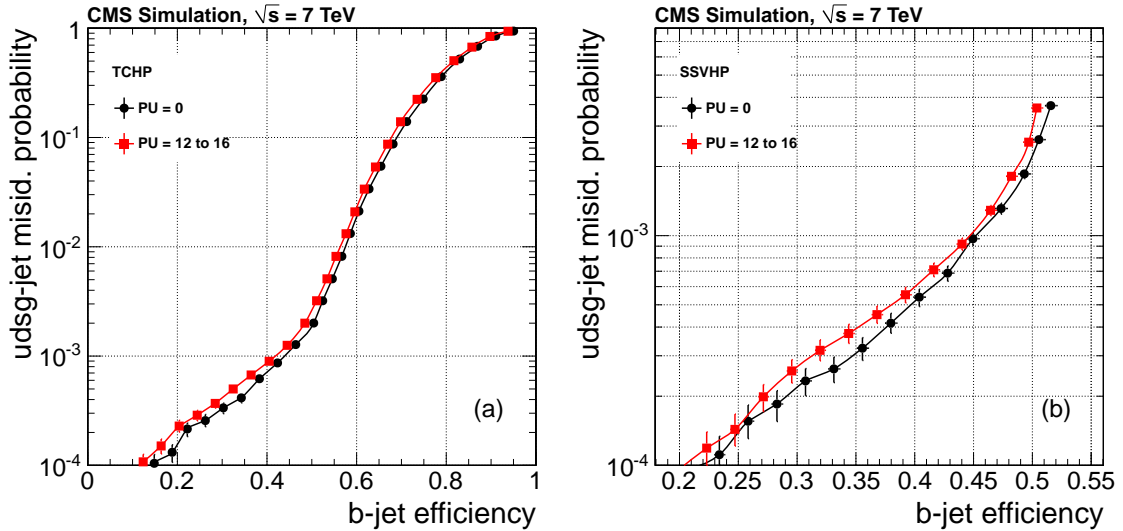


Figure 9. Light-parton misidentification probability versus b-jet tagging efficiency for jets with $p_T > 60 \text{ GeV}/c$ at generator level for the (a) TCHP and (b) SSVHP algorithms for different pileup (PU) scenarios.

5 Efficiency measurement with multijet events

For the b-jet tagging algorithms to be used in physics analyses, it is crucial to know the efficiency for each algorithm to select genuine b jets. There are a number of techniques that can be applied to CMS data to measure the efficiencies *in situ*, and thus reduce the reliance on simulations. If event distributions from MC simulation match those observed in data reasonably well, then the simulation can be used for a wide range of topologies after applying corrections determined from specific data samples. Corrections can be applied to simulated events using a scale factor SF_b , defined as the ratio of the efficiency measured with collision data to the efficiency found in the equivalent simulated samples, using MC generator-level information to identify the jet flavour.

Furthermore, the measurement techniques used for data are also applied to the simulation in order to validate the different algorithms.

Some efficiency measurements are performed using samples that include a jet with a muon within $\Delta R = 0.4$ from the jet axis (a “muon jet”). Because the semileptonic branching fraction of b hadrons is significantly larger than that for other hadrons (about 11%, or 20% when $b \rightarrow c \rightarrow \ell$ cascade decays are included), these jets are more likely to arise from b quarks than from another flavour. Muons are identified very efficiently in the CMS detector, making it straightforward to collect samples of jets with at least one muon. These muons can be used to measure the performance of the lifetime-based tagging algorithms, since the efficiencies of the muon- and lifetime-based b-jet identification techniques are largely uncorrelated. Sections 5.1 and 5.2 describe efficiency measurements that use muon jets, while the technique of section 5.3 makes use of a more generic dijet sample. The results are given in section 7.

5.1 Efficiency measurement with kinematic properties of muon jets

Due to the large b-quark mass, the momentum component of the muon transverse to the jet axis, p_T^{rel} , is larger for muons from b-hadron decays than for muons in light-parton jets or from charm hadrons. This component is used as the discriminant for the “PtRel” method. In addition, the impact parameter of the muon track, calculated in three dimensions, is also larger for b hadrons than for other hadrons. This parameter is used as the discriminant for the “IP3D” method. Both of these variables can thus be used as a discriminant in the b-jet tagging efficiency determination. In both cases, the discriminating power of the variable depends on the muon jet p_T . The muon p_T^{rel} (IP) distributions provide better separation for jets with p_T smaller (greater) than about 120 GeV/c. The PtRel and IP3D methods rely on fits to the p_T^{rel} [35] and muon IP distributions in the data with respect to simulated spectra for the b signal and charm+light-parton background.

In the two methods, the p_T^{rel} and IP spectra for muon jets are modelled using simulated distributions that represent the spectra expected for different jet flavours to obtain the b-jet content of the sample. The efficiency for a particular tagger is obtained by measuring the fraction of muon jets that satisfy the requirements of the tagger. To make the treatment of the statistical uncertainty more straightforward, the muon jet sample is separated into those jets that satisfy and those that fail the requirements of the tagger. These jets are referred to as “tagged” and “untagged.”

A dijet sample with high b-jet purity is obtained by requiring that events have exactly two reconstructed jets: the muon jet as defined above and another jet fulfilling the TCHPM b-jet tagging criterion (the “medium” operating point for the TCHP algorithm). Simulated MC events are used to establish p_T^{rel} and IP spectra for muon jets resulting from the fragmentation of b, c, and light partons. Muons in light-parton jets mostly arise from the decay of charged pions or kaons and from misidentified muons or hadronic punch-through in the calorimeters, effects that might not be modelled well in the simulation. The spectra for light-parton jets from simulation can be validated against control samples of collision data. In figure 10 the distributions of p_T^{rel} and $\ln(|\text{IP}|[\text{cm}])$ derived from the simulation are compared to the ones obtained for tracks in inclusive jet data by applying the same kinematic selection and track reconstruction quality requirements as for the muon candidates. In order to measure the ability of the simulation to model the investigated spectra, we apply the same procedure to a sample of simulated inclusive jet events. The spectra derived for

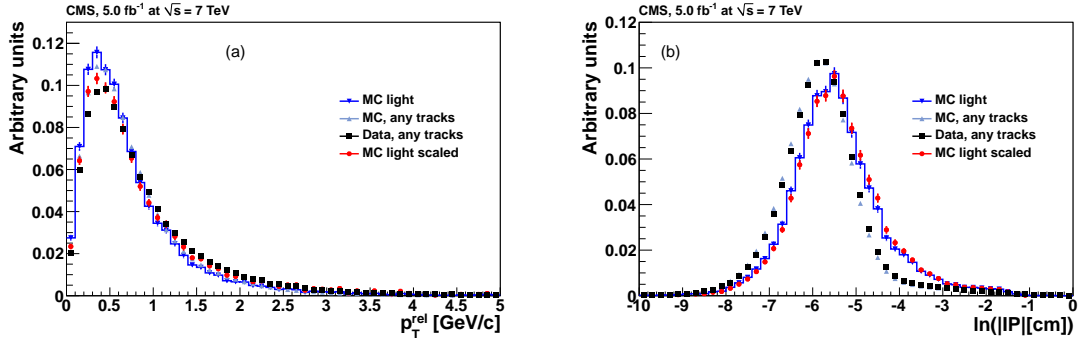


Figure 10. Comparison of distributions of (a) muon p_T^{rel} for jets with p_T between 80 and 120 GeV/c and (b) $\ln(|IP|[cm])$ for jets with p_T between 160 and 320 GeV/c for muons in simulated light-parton jets (“MC light”), tracks from simulated inclusive jet events (“any tracks”), tracks from data, and muons in simulated light-parton jets after corrections based on data (“MC light scaled”).

low- p_T muons from light-parton jets in simulation are corrected by multiplying them with the ratio of shapes of the inclusive distributions obtained in data and simulation on a bin-by-bin basis.

The fractions of each jet flavour in the dijet sample are extracted with a binned maximum likelihood fit using p_T^{rel} and IP templates for b, c and light-parton jets derived from simulation or inclusive jet data. The fits are performed independently in the tagged and untagged subsamples of the muon jets. Results of representative fits are shown in figures 11 and 12.

From each fit the fractions of b jets (f_b^{tag} , f_b^{untag}) are extracted from the data. With these fractions and the total yields of tagged and untagged muon jets ($N_{\text{data}}^{\text{tag}}$, $N_{\text{data}}^{\text{untag}}$), the number of b jets in these samples are calculated, and the efficiency ϵ_b^{tag} for tagging b jets in the data is inferred:

$$\epsilon_b^{\text{tag}} = \frac{f_b^{\text{tag}} \cdot N_{\text{data}}^{\text{tag}}}{f_b^{\text{tag}} \cdot N_{\text{data}}^{\text{tag}} + f_b^{\text{untag}} \cdot N_{\text{data}}^{\text{untag}}} . \quad (5.1)$$

To obtain SF_b , the efficiency for tagging b jets in the simulation is obtained from jets that have been identified as b jets with MC generator-level matching.

5.2 Efficiency measurement with the System8 method

The “System8” method [36, 37] is applied to events with a muon jet and at least one other, “away-tag”, jet. The muon jet is used as a probe. The reference lifetime tagger and a supplementary p_T^{rel} -based selection are tested on this jet. The away-tag jet is tested with a separate lifetime tagger. There are eight quantities that can be counted from the full data sample. The quantities depend on the number of passing or failing tags. A set of equations correlates these eight quantities with the tagging efficiencies.

A muon jet can be tagged as a b jet using either a lifetime tagger, or by requiring that the muon has large p_T^{rel} . In this analysis, the requirement is $p_T^{\text{rel}} > 0.8 \text{ GeV}/c$. These two tagging criteria have efficiencies ϵ_b^{tag} and $\epsilon_b^{\text{PtRel}}$, respectively, for b jets. The third tagging criterion is the requirement that another jet in the event passes also a lifetime-based tagger. This last requirement defines the “away-tag sample”. It enriches the b content of the events, and thus makes it more likely that the muon jet is a b jet. Correlations between the efficiencies of the two tagging criteria are estimated

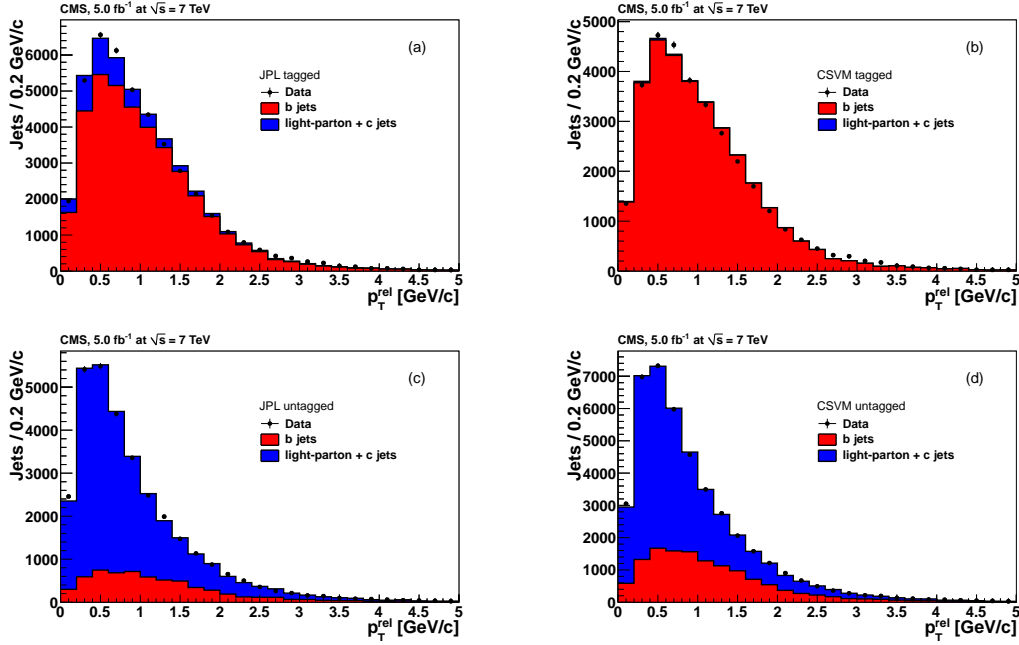


Figure 11. Fits of the summed b and non-b templates, for simulated muon jets, to the muon p_T^{rel} distributions from data. (a) and (c) show the results for muon jets that pass (tagged) or fail (untagged) the b-jet tagging criteria of the JPL method, respectively. (b) and (d) are the equivalent plots for the CSVM method. The muon jet p_T is between 80 and 120 GeV/c.

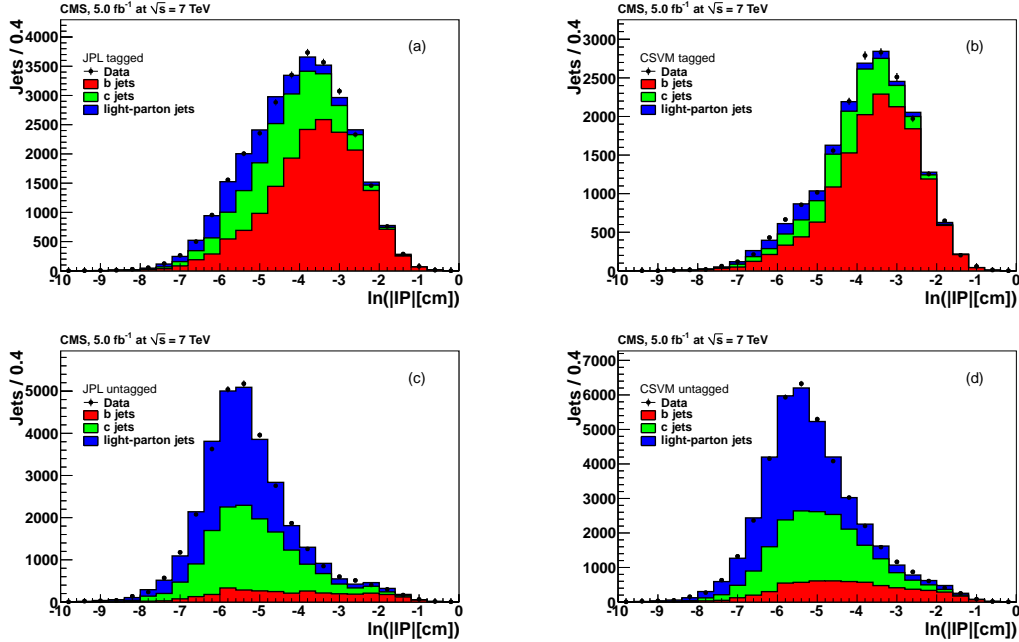


Figure 12. Same as figure 11 using the $\ln(|\text{IP}|[\text{cm}])$ distributions. The muon jet p_T is between 160 and 320 GeV/c.

from simulation. As p_T^{rel} provides less discrimination between jet flavours at higher jet energies, the System8 method loses sensitivity for jet $p_T > 120 \text{ GeV}/c$.

With these criteria eight quantities are measured. The four quantities for the muon jets are: the total number of muon jets in the sample n , the number of muon jets that pass the lifetime-tagging criterion n^{tag} , the number of muon jets that pass the p_T^{rel} requirement n^{PtRel} , and the number of muon jets that pass both criteria $n^{\text{tag,PtRel}}$. Likewise, the four quantities for the away-tag sample are labelled p , p^{tag} , p^{PtRel} , $p^{\text{tag,PtRel}}$. The away-tag jets are tagged with the TCHPL criterion.

The full muon jet sample, n , and the away-tag sample, p , are each composed of an unknown mix of b and non-b jets. The non-b jets are labelled “c ℓ ”. The muon sample thus comprises n_b and $n_{c\ell}$, and the away-tag sample, p_b and $p_{c\ell}$. The efficiencies of the two tagging criteria on b jets (ϵ_b^{tag} , $\epsilon_b^{\text{PtRel}}$) and on non-b jets ($\epsilon_{c\ell}^{\text{tag}}$, $\epsilon_{c\ell}^{\text{PtRel}}$) are also unknown, for a total of eight unknown quantities. Thus, a system of eight equations can be written that relates the measurable quantities to the unknowns:

$$\begin{aligned}
 n &= n_b + n_{c\ell} , \\
 p &= p_b + p_{c\ell} , \\
 n^{\text{tag}} &= \epsilon_b^{\text{tag}} n_b + \epsilon_{c\ell}^{\text{tag}} n_{c\ell} , \\
 p^{\text{tag}} &= \beta^{\text{tag}} \epsilon_b^{\text{tag}} p_b + \alpha^{\text{tag}} \epsilon_{c\ell}^{\text{tag}} p_{c\ell} , \\
 n^{\text{PtRel}} &= \epsilon_b^{\text{PtRel}} n_b + \epsilon_{c\ell}^{\text{PtRel}} n_{c\ell} , \\
 p^{\text{PtRel}} &= \beta^{\text{PtRel}} \epsilon_b^{\text{PtRel}} p_b + \alpha^{\text{PtRel}} \epsilon_{c\ell}^{\text{PtRel}} p_{c\ell} , \\
 n^{\text{tag,PtRel}} &= \beta^n \epsilon_b^{\text{tag}} \epsilon_b^{\text{PtRel}} n_b + \alpha^n \epsilon_{c\ell}^{\text{tag}} \epsilon_{c\ell}^{\text{PtRel}} n_{c\ell} , \\
 p^{\text{tag,PtRel}} &= \beta^p \epsilon_b^{\text{tag}} \epsilon_b^{\text{PtRel}} p_b + \alpha^p \epsilon_{c\ell}^{\text{tag}} \epsilon_{c\ell}^{\text{PtRel}} p_{c\ell} .
 \end{aligned} \tag{5.2}$$

The method assumes that the efficiencies for a combination of tagging criteria are factorizable. Thus eight correlation factors are introduced to solve the system of equations: α^{tag} , β^{tag} , α^{PtRel} , β^{PtRel} , α^n , β^n , α^p , and β^p . These factors are obtained from the simulation as a function of the muon jet p_T and $|\eta|$. The factors α and β are determined for non-b and b jets, respectively. The superscripts “tag” and “PtRel” of α and β indicate the efficiency ratio of the p to the n samples for the lifetime and p_T^{rel} criteria. The superscripts “n” and “p” refer to the correlation between the two tagging efficiencies, “tag” and “PtRel”, in the n and p samples.

The simulation predicts that the correlation coefficients typically range between 0.95 and 1.05 for those associated with the b-jet tagging efficiencies, and between 0.7 and 1.2 for those associated with the c+ ℓ -tagging efficiencies. A numerical computation is applied to solve the system of eight equations in the data to determine the eight unknowns, thus simultaneously determining the tagging efficiencies and flavour contents of both the full and away-tag samples.

5.3 Efficiency measurement using a reference lifetime algorithm

While muon p_T^{rel} provides less discrimination power between jet flavours at large jet p_T , the lifetime-based algorithms described in sections 4.2 and 4.3 (TCHE, TCHP, JP, JBP, SSVHE, SSVHP and CSV) retain their sensitivity to distinguish different jet flavours. In particular, the discriminant for the jet probability algorithm has different distributions for different jet flavours for jet momenta in the range $30 < p_T < 700 \text{ GeV}/c$. The JP algorithm can be calibrated directly with data. Tracks

with negative impact parameter are used to compute the probability that those tracks come from the primary vertex. The same calibration is performed separately in simulated samples. As a result, the JP algorithm serves as a reference for estimating the fraction of b jets in a data sample, and also for estimating the fraction of b jets in a subsample that has been selected by an independent tagging algorithm. In this manner the efficiency of the independent algorithm can be measured. This method is called the lifetime tagging method (“LT”). It can be performed on both inclusive and muon jet samples. The resulting scale factors are compared to obtain an estimate of the systematic uncertainty.

The efficiency measurement is performed in inclusive jet events in which at least one jet must be above a given p_T threshold, and separately in dijet events in which at least one jet is a muon jet. To increase the fraction of b jets in the inclusive sample, an additional jet tagged by the JPM algorithm is also required. The sample with muon jets is already sufficiently enriched in b jets by the muon requirement. The same set of samples can be established with simulated events, so that the true tagging efficiency can be measured there and a scale factor computed.

Because a value of the JP discriminant can be defined for jets that have as few as one track with a positive impact parameter significance, the discriminant can be calculated for most b jets, regardless of their p_T . The fraction of b jets that have JP information, C_b , rises from about 0.91 at $p_T = 20 \text{ GeV}/c$ to more than 0.98 for $p_T > 50 \text{ GeV}/c$.

Figure 13 shows the JP discriminant distributions in the muon jet sample and the inclusive sample, before and after tagging the jets with an independent tagger, in this case the CSV tagger. Also shown is a fit to the distributions using JP-discriminant templates derived from simulations of b, c, and light-parton jets. The normalization of the relative flavour fractions f_b , f_c and f_{light} is left free, with the constraint that $f_b + f_c + f_{\text{light}} = 1$. The b-jet tagging efficiency is the ratio of the number of b jets that are tagged by the independent tagger to the number of b jets before the tagging. The numbers are calculated using the fit. The b-jet tagging efficiency is corrected for the fraction of jets that have JP information,

$$\epsilon_b^{\text{tag}} = \frac{C_b \cdot f_b^{\text{tag}} \cdot N_{\text{data}}^{\text{tag}}}{f_b^{\text{before tag}} \cdot N_{\text{data}}^{\text{before tag}}}, \quad (5.3)$$

where the superscripts “before tag” and “tag” refer to the samples before and after application of the tagging criterion.

Examples of the efficiencies measured for the JPL and CSV taggers are shown in figure 14. In both cases the results from simulation are close to those obtained from data.

This technique cannot be used to measure the efficiency of the JP algorithm itself, as the JP discriminant is used in the fit to determine the b-jet content of the sample. However, the CSV discriminant, which is mostly based on information from secondary vertices, can be used in its place to determine the flavour content. More than 90% of jets have CSV information, as is the case with the JP discriminant. But unlike the JP discriminant, the CSV discriminant cannot be calibrated solely with the data. To remedy this, the CSV discriminant is used to estimate the tagging efficiency of the TC algorithms. By comparing these results to those using the JP discriminant, the bias due to using the CSV discriminant is determined to be (0–2%, 4–6%, 6–9%) for the (loose, medium, tight) operating points. The efficiencies and scale factors for the JP algorithm are corrected for these biases.

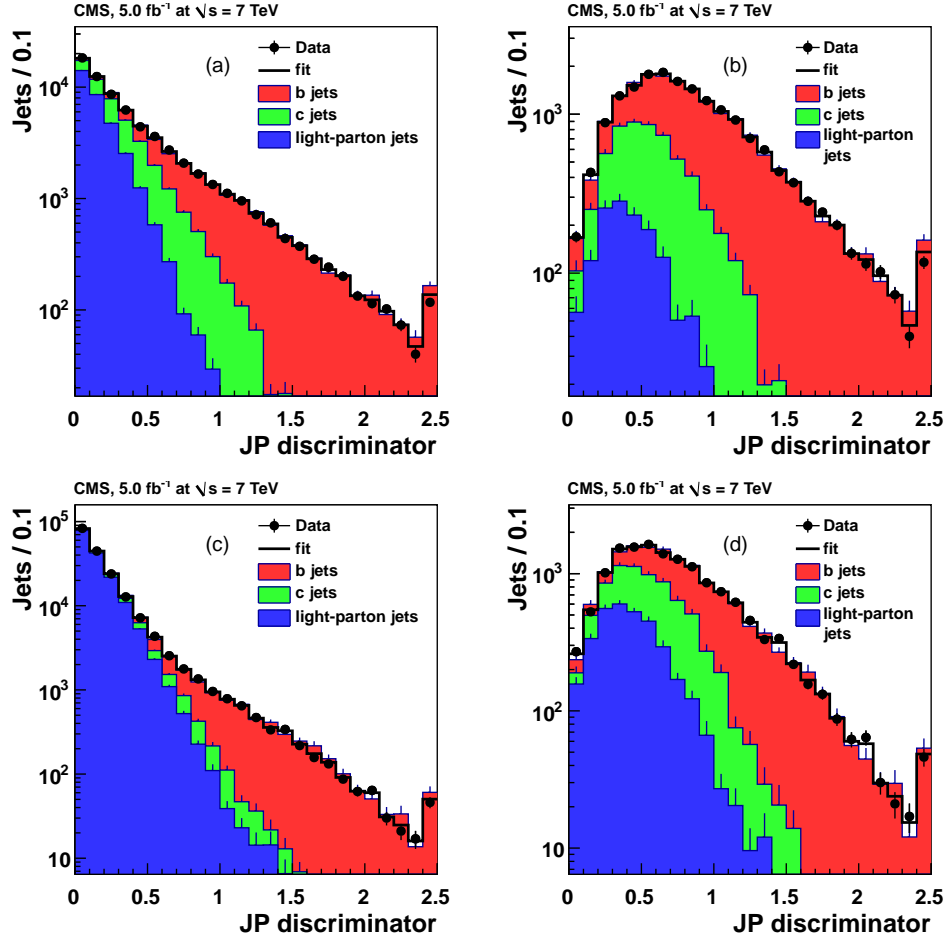


Figure 13. Fits of the summed b, c and light-parton templates, for simulated jets, to the JP-discriminant distributions from data. (a) and (b) show the results for muon jets before and after identification with the CSVM tagger, respectively. (c) and (d), the equivalent plots for inclusive jets. The black line is the sum of the contributions from the templates. The jet p_T is in the range $260 < p_T < 320 \text{ GeV}/c$. Overflows are displayed in the rightmost bins.

5.4 Systematic uncertainties on efficiency measurements

Several systematic uncertainties affect the measurement of the b-jet tagging efficiency. Some are common to all four methods (PtRel, IP3D, System8, LT), some are common to a subset of them, and some are unique to a particular method.

Common systematic uncertainties for all methods:

- **Pileup:** the measured b-jet tagging efficiency depends on the number of pp collisions superimposed on the primary interaction of interest. The systematic uncertainty is computed by varying the average value of the pileup in data by 10% and calculating the difference in the values of SF_b after reweighting the simulation with the modified distribution.
- **Gluon splitting:** studies of angular correlation between b jets at the LHC [38] indicate that QCD events may have a larger fraction of gluon splitting into $b\bar{b}$ pairs than is assumed in the

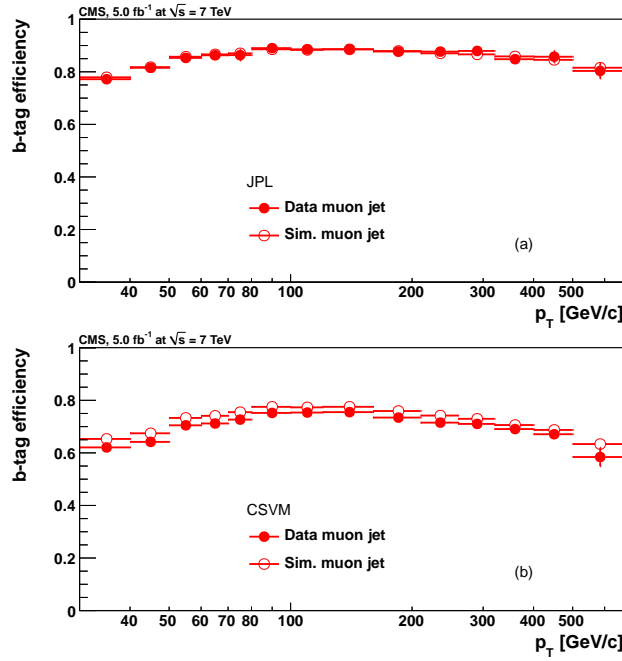


Figure 14. Efficiencies for the identification of b-jets measured for (a) the JPL and (b) the CSVM tagger with the LT method in the muon jet sample. Filled and open circles correspond to data and simulation, respectively.

generation of the simulation. A study was carried out with the MC sample where the number of events with gluon splitting was artificially changed by 50%. Results obtained with this modified gluon splitting MC sample are then compared to those with the original sample. The observed deviation is quoted as a systematic uncertainty.

- **Muon p_T^μ :** the central value of the b-jet tagging efficiency is extracted from data with muon $p_T^\mu > 5$ GeV/c. The choice of the selection affects the shape of the template distributions used in fits, and also the number of events used to measure the tagging efficiencies. The p_T^μ threshold is varied up to 9 GeV/c to test the sensitivity to this choice.

Common uncertainty for the PtRel, IP3D and System8 methods:

- **Away-jet tagger:** the dependency of the calculated b-jet tagging efficiency on the away-jet tagger is studied by comparing the results obtained by tagging the away jets with different variants of the TC algorithm (TCHEL, TCHEM, TCHPM). The measured SF_b tends to increase when the away tag is tighter. The maximum deviation from the default away-jet tagger is taken as a systematic uncertainty.

Uncertainty unique to the PtRel method:

- **Ratio of light-parton to charm jets in simulation:** the shapes of the p_T^{rel} and IP spectra for light-parton jets have been obtained from control samples in data, which minimizes the bias due to a mismodelling of the muon kinematics in the simulation. However, since the p_T^{rel} distribution in data is fitted with a sum of templates for b jets and for c+udsg jets, uncertainties

on the ratio between light-parton and charmed jets in the simulation must be considered. To do so, the predicted ratio is varied by $\pm 20\%$, and the fit is repeated, taking the variation in the results as a systematic uncertainty. This uncertainty does not apply to the IP method, where a three-component fit is performed that determines the light-parton and charm contributions independently.

Uncertainties unique to the System8 method:

- **Selection on p_T^{rel} :** one of the System8 criteria is a selection on the muon $p_T^{\text{rel}} > 0.8 \text{ GeV}/c$. In order to test the sensitivity to the b purity in the muon jet sample and the relative charm/light-parton fraction in the non-b background, this selection was changed from 0.5 to $1.2 \text{ GeV}/c$ in the data. The correlation factors were recomputed accordingly in the simulation and the System8 method was applied again to the data in order to compute the b-jet tagging efficiency. The largest deviation observed from the central value is quoted as a systematic uncertainty.
- **MC closure test:** the b-jet tagging efficiency can be directly calculated from the simulated QCD muon-enriched sample, as the flavour of the jets at generator level is known. In this case, the efficiency can be measured by taking the number of identified true b jets over all true b jets. The resulting value is denoted as the MC truth b-jet tagging efficiency. The System8 method is also applied to this MC sample. The resulting b-jet tagging efficiencies are in good agreement with the MC truth, giving a negligible systematic uncertainty. (This systematic uncertainty does not appear for the other methods as they rely on template fits, making such a test trivial.)

Uncertainties unique to the LT method:

- **Fraction of b jets with JP information:** the fraction of inclusive jets with JP information is well described by the simulation. As explained above, the number of b jets before tagging is measured by a fit to the JP distribution and corrected by the fraction C_b of b jets with JP information. A systematic uncertainty of half the residual correction, $(1 - C_b)/(2C_b)$, is estimated from the simulation as a function of the b-jet p_T . A corresponding factor with a similar uncertainty is needed for measuring the efficiency of the JP and JBP taggers with the CSV discriminator spectrum.
- **Difference between muon jets and inclusive jets:** in the fits to the Jet Probability discriminator, the shape for the light-parton contribution is mostly calibrated from the data. However, as the LT method relies on a lifetime discriminator, a systematic effect may arise from some mismodelling of correlations for b jets between the JP discriminator and the other tagging criterion under study. This effect is specific to the LT method. In order to estimate the uncertainty due to this effect, two independent samples with different b-jet fractions are considered: the muon-jet sample and an inclusive jet sample (where another jet is tagged by the JPM criterion). The difference between the measured SF_b in muon jets and in inclusive b jets is taken as a systematic uncertainty. This is the largest contribution to the systematic uncertainty on SF_b with the LT method. Due to the large statistical uncertainty on SF_b for inclusive jets with $p_T < 80 \text{ GeV}/c$, the same systematic uncertainty is used for $p_T < 80 \text{ GeV}/c$

and for the range 80–210 GeV/c. If the difference on SF_b between muon jets and inclusive jets is smaller than the statistical error on SF_b for inclusive jets, this uncertainty is used for the systematic uncertainty estimate.

- **Bias for the JP and JBP taggers:** the uncertainty on the measurement of the bias, when using the CSV discriminant to measure the efficiency of the JP and JBP taggers as estimated for the TC taggers, is propagated into the uncertainty on the scale factors for these taggers.

The systematic uncertainties on the data/MC scale factors for different tagging criteria are detailed in tables 1–4 for the PtRel and System8 methods at low jet p_T ($80 < p_T < 120$ GeV/c) and for the IP3D and LT methods at higher jet p_T ($160 < p_T < 320$ GeV/c). In these momentum ranges the average uncertainty is about 3% for the PtRel method, 6–10% for the System8 method, 3–4% for the IP3D method, and 2–7% for the LT method.

6 Efficiency measurement with $t\bar{t}$ events

In the framework of the standard model, the top quark is expected to decay to a W boson and a b quark about 99.8% of the time [22]. Experimentally, the measurement of the heavy-flavour content of $t\bar{t}$ events can provide either a direct measurement of the branching fraction of the decay of the top quark to a W boson and a b quark, $B(t \rightarrow Wb)$, or, assuming $B(t \rightarrow Wb) = 1$, the b-jet tagging efficiency. The b jets in $t\bar{t}$ events have an average p_T of about 80 GeV/c and cover a p_T range relevant for many processes both within the standard model and for many models beyond the standard model.

In this section, we present several methods to study the heavy-flavour content of $t\bar{t}$ events. The profile likelihood ratio (PLR) method, described in section 6.3, and the flavour tag matching (FTM) method, described in section 6.5, use $t\bar{t}$ events in the dilepton channel in which both W bosons decay into leptons. The flavour tag consistency (FTC) method, described in section 6.4, and the bSample method (section 6.6) use $t\bar{t}$ events in the lepton+jets channel, in which one W boson decays into quarks and the other into a charged lepton and a neutrino. These methods are used to measure the efficiency of tagging b jets in the data and the simulation over the average p_T and η range of jets in the top-quark events. The differences in efficiencies observed between the data and MC simulation are provided as a data/MC scale factor SF_b similar to the techniques described in section 5.

6.1 Event selection

The event reconstruction used herein follows closely the event selection performed for the $t\bar{t}$ production cross section measurements [1, 39], with the exception of the b-jet tagging requirements. All objects are reconstructed using a particle-flow algorithm.

In the lepton+jets channel, the final state is composed of four jets, one energetic isolated muon and missing transverse energy. Events are required to pass a single-muon trigger. After offline reconstruction, events are selected requiring exactly one isolated muon with $p_T > 30$ GeV/c and $|\eta| < 2.1$ and at least four jets with $p_T > 30$ GeV/c and $|\eta| < 2.4$. The FTC method further requires

Table 1. Relative systematic uncertainties on SF_b for the PtRel method in the muon jet p_T range 80–120 GeV/c, using the medium operating point of the b-jet tagging algorithms.

| b tagger | pileup | $g \rightarrow b\bar{b}$ | p_T^μ | away jet | light / charm | total |
|----------|--------|--------------------------|-----------|----------|---------------|-------|
| JPM | 1.6% | 1.6% | 1.1% | 1.9% | 0.4% | 3.2% |
| JBPM | 0.9% | 0.5% | 1.8% | 1.2% | 0.5% | 2.5% |
| TCHEM | 1.5% | 0.5% | 1.4% | 1.6% | 0.4% | 2.7% |
| TCHPM | 1.1% | 0.1% | 2.3% | 1.1% | 0.6% | 2.8% |
| SSVHEM | 0.7% | 1.3% | 2.0% | 0.4% | 0.4% | 2.5% |
| CSVM | 1.4% | 1.3% | 1.3% | 1.2% | 0.5% | 2.6% |

Table 2. Relative systematic uncertainties on SF_b for the System8 method in the muon jet p_T range 80–120 GeV/c, using the medium operating point of the b-jet tagging algorithms.

| b tagger | pileup | $g \rightarrow b\bar{b}$ | p_T^μ | away jet | p_T^{rel} | MC closure | total |
|----------|--------|--------------------------|-----------|----------|--------------------|------------|-------|
| JPM | 1.4% | 0.6% | 4.2% | 3.9% | 1.6% | 0.1% | 6.1% |
| JBPM | 1.5% | 1.9% | 6.5% | 1.5% | 4.0% | <0.1% | 8.2% |
| TCHEM | 1.3% | 1.3% | 6.6% | 2.1% | 2.4% | <0.1% | 7.5% |
| TCHPM | 1.3% | 2.7% | 8.2% | 1.9% | 4.0% | 0.1% | 9.7% |
| SSVHEM | 1.3% | 0.1% | 3.7% | 2.8% | 3.0% | <0.1% | 5.6% |
| CSVM | 1.5% | 0.4% | 4.3% | 1.3% | 4.5% | 0.1% | 6.5% |

Table 3. Relative systematic uncertainties on SF_b for the IP3D method in the muon jet p_T range 160–320 GeV/c, using the medium operating point of the b-jet tagging algorithms.

| b tagger | pileup | $g \rightarrow b\bar{b}$ | p_T^μ | away jet | total |
|----------|--------|--------------------------|-----------|----------|-------|
| JPM | 0.1% | 0.7% | 0.1% | 3.2% | 3.2% |
| JBPM | 0.2% | 1.7% | 0.4% | 2.8% | 3.3% |
| TCHEM | 0.1% | 1.2% | 0.4% | 2.4% | 2.7% |
| TCHPM | 0.2% | 2.3% | 0.7% | 2.2% | 3.3% |
| SSVHEM | 0.6% | 2.2% | 0.3% | 2.9% | 3.6% |
| CSVM | 0.6% | 2.3% | 0.1% | 3.2% | 4.0% |

Table 4. Relative systematic uncertainty on SF_b with the LT method in the muon jet p_T range 160–320 GeV/c, using the medium operating point of the b-jet tagging algorithms.

| b tagger | pileup | $g \rightarrow b\bar{b}$ | p_T^μ | C_b | inc. jets | bias | total |
|----------|--------|--------------------------|-----------|-------|-----------|------|-------|
| JPM | 0.1% | 0.8% | 0.5% | 0.1% | 4.4% | 4.0% | 6.0% |
| JBPM | 0.1% | 0.4% | 0.8% | 0.1% | 4.3% | 4.0% | 5.9% |
| TCHEM | 0.1% | 1.6% | 0.3% | 0.2% | 2.8% | — | 3.2% |
| TCHPM | 0.2% | 0.5% | 0.5% | 0.2% | 1.7% | — | 1.9% |
| SSVHEM | 0.1% | 2.3% | 0.8% | 0.2% | 6.6% | — | 7.0% |
| CSVM | 0.2% | 2.3% | 0.7% | 0.2% | 5.2% | — | 5.7% |

that the two leading jets have transverse momenta greater than 70 GeV/c and 50 GeV/c respectively, and that the transverse momentum of the muon is greater than 35 GeV/c. The reconstructed missing transverse energy (\cancel{E}_T) is required to be above 20 GeV.

In the dilepton channel, the final state is composed of two jets, two energetic isolated leptons (electron or muon) and missing transverse energy. Events are required to pass dilepton triggers in which two muons, two electrons, or one electron and one muon are required to be present. After offline reconstruction, events are selected with two isolated, oppositely charged leptons with $p_T > 20 \text{ GeV/c}$ and $|\eta| < 2.5$ (2.4) for electrons (muons), at least two jets with $p_T > 30 \text{ GeV/c}$ and $|\eta| < 2.4$, and $\cancel{E}_T > 30 \text{ GeV}$ for $ee/\mu\mu$ events. The selected leptons and jets are required to originate from the same primary interaction vertex. Events with same-flavour lepton pairs in the dilepton mass window ($76 < m_{\ell\ell} < 106 \text{ GeV/c}^2$) are removed to suppress the dominant Z+jet background. Dilepton pairs from heavy-flavour resonances and low-mass Drell–Yan production are also removed by requiring a minimum dilepton invariant mass of 12 GeV/c^2 .

The numbers of observed and predicted events in the lepton+jets channel and the dilepton channel are given in tables 5 and 6, respectively. The uncertainties include the uncertainties on the luminosity measurement and the cross sections. For all MC predictions, events are reweighted to take into account differences in trigger and lepton selection efficiencies between data and simulation [1, 39]. The lepton selection efficiency scale factors are estimated from data using Z events. For dilepton events, the trigger efficiencies are estimated on a data sample using a trigger that is weakly correlated to the dilepton triggers. The dilepton trigger selection efficiency is estimated on events which contain two leptons that fulfil the complete dilepton event selection.

The Drell–Yan background is measured using data. Two different methods are used, and the two estimates are compatible. In the PLR method, for the ee and $\mu\mu$ channels, the ratio of Drell–Yan events outside and inside the dilepton invariant mass window, $R_{\text{out/in}}$, is estimated from the simulation. This is used to estimate the Drell–Yan background using the number of data events inside the dilepton invariant mass window [39]. A contamination from other backgrounds can still be present in the Z-mass window, and this contribution is subtracted using the $e\mu$ channel scaled according to the event yields in the ee and $\mu\mu$ channels. For the $e\mu$ channel, the DY background yield is estimated after performing a binned maximum-likelihood fit to the dilepton invariant mass distribution. In the FTM method, the number of Drell–Yan events in the ee and $\mu\mu$ channels is estimated from the shape of the distribution of the angle between the momentum vectors of the two leptons. For the $e\mu$ channel, the predictions are taken from simulation.

6.2 Systematic uncertainties

Most of the sources of systematic uncertainties are common to all methods, and several methods have specific additional contributions. A description of the common systematic uncertainties is given in this section. The description of the procedure to estimate the systematic uncertainties in each analysis and the influence of the different sources will be given separately for each analysis in its relevant section.

There are different sources of uncertainties originating from the detector knowledge or related to the theory and the simulation. These uncertainties can affect the normalization factor for each process or they can distort the distributions themselves.

Table 5. Number of observed and predicted events in the lepton+jets sample after applying all selection requirements of the FTC method. All MC samples have been scaled to an integrated luminosity of 2.3 fb^{-1} . The uncertainties include the uncertainties on the luminosity and the cross sections. The CSVM operating point has been used for the b-jet tagging requirement.

| | no tagging | ≥ 1 b-tagged jets | ≥ 2 b-tagged jets |
|------------------|------------------|------------------------|------------------------|
| $t\bar{t}$ | 8504 ± 1275 | 7425 ± 1113 | 3744 ± 561 |
| Single top | 477 ± 82 | 394 ± 118 | 162 ± 49 |
| W+jets | 6170 ± 1851 | 1367 ± 410 | 214 ± 64 |
| Z+jets | 459 ± 138 | 83 ± 25 | 15 ± 5 |
| QCD | 23 ± 7 | 3 ± 1 | 0.20 ± 0.06 |
| Total prediction | 15633 ± 2253 | 9272 ± 1921 | 4134 ± 566 |
| Data | 14391 | 8781 | 3897 |

Table 6. Number of observed and predicted events in the dilepton sample after applying all selection requirements of the PLR method. All MC samples have been scaled to a luminosity of 2.3 fb^{-1} . The uncertainties include the uncertainties on the luminosity and the cross sections. The TCHEL operating point has been used for the b-jet tagging requirement. The component “ $t\bar{t}$ signal” stands for the dilepton events. The component “ $t\bar{t}$ other” contains the events in all other decay channels.

| Processes | Channel ee | Channel $\mu\mu$ | Channel $e\mu$ |
|-----------------------------------|-----------------|------------------|------------------|
| Without b-jet tagging requirement | | | |
| $t\bar{t}$ signal | 971 ± 147 | 1275 ± 182 | 3453 ± 521 |
| $t\bar{t}$ other | 11.5 ± 5.7 | 3.3 ± 1.7 | 23.6 ± 11.8 |
| Single top | 48.7 ± 14.6 | 62.7 ± 18.9 | 163.7 ± 49.0 |
| Di-bosons | 22.3 ± 6.7 | 29.2 ± 8.8 | 49.4 ± 14.8 |
| Z+jets | 409 ± 204 | 545 ± 273 | 200 ± 100 |
| W+jets | 12.0 ± 6.0 | < 0.5 | 11.4 ± 5.7 |
| Total prediction | 1475 ± 259 | 1915 ± 343 | 3902 ± 512 |
| Data | 1442 | 1773 | 3898 |
| With ≥ 1 b-tagged jets | | | |
| Total prediction | 1088 ± 170 | 1429 ± 218 | 3390 ± 475 |
| Data | 1080 | 1364 | 3375 |
| With ≥ 2 b-tagged jets | | | |
| Total prediction | 529 ± 73 | 697 ± 97 | 1827 ± 263 |
| Data | 554 | 686 | 1854 |

The dominant sources of uncertainty arise from the MC simulation. The uncertainty due to the modelling of the underlying event is estimated by comparing results between the main sample generated with the Z2 tune to that with the D6T tune [40]. The effect due to the scale used to match clustered jets to partons (i.e., jet-parton matching) is estimated with dedicated samples generated by varying the nominal matching p_T thresholds by factors of 2 and 1/2. Effects due to the definition of the renormalization and factorization scales used in the simulation of the signal are studied with dedicated MC samples with the scales varied simultaneously by factors of 2 and 1/2. The

uncertainties related to the parton distribution function (PDF) used to model the hard scattering of the proton-proton collisions are estimated by varying the parameters of the PDF by $\pm 1\sigma$ with respect to their nominal values and using the PDF4LHC prescription [13, 15]. Variations in the relative composition of the simulated samples are studied by varying the contributions of each background with respect to the signal and each other.

Several systematic uncertainties pertain to the modelling of the CMS detector in the MC simulations. Important uncertainties are the energy scales of the jets and, to a lesser extent, of the leptons, as they shift the momenta of the reconstructed objects. Similarly, the uncertainty in jet energy resolution has also been considered. The effects of the jet energy scale are taken into account by varying the energy scale of the jets according to its uncertainty [27]. A further source comes from the uncertainties associated with the measurement of the trigger and lepton selection efficiencies. The uncertainty due to pileup is evaluated by varying the mean value of the measured pileup distribution by $\pm 10\%$.

6.3 Profile likelihood ratio method

In this method, the data/MC scale factor of the b-jet tagging efficiency is measured with the PLR method using the 2-dimensional distribution of the jet multiplicity versus the b-tagged jet multiplicity in dilepton events. The uncertainties in the event yield and in the shape of the distribution are considered as nuisance parameters in the likelihood function and are then fitted during the minimization procedure. This leads to combined statistical and systematic uncertainties associated with the measurement of the scale factor.

The likelihood function for a given dilepton channel j (ee , $e\mu$ or $\mu\mu$) and a given bin i of the 2-dimensional distribution (corresponding to n jets and m b-tagged jets) is written as [41]:

$$\mathcal{L}_{i,j}(SF_b, N_{i,j}^{\text{obs}}, \{U_k\}) = \text{Poisson}(N_{i,j}^{\text{obs}}, \mu_{i,j}(SF_b, \{U_k\})) \times \prod_k \text{Gauss}(U_k, 0, 1), \quad (6.1)$$

where $N_{i,j}^{\text{obs}}$ is the number of observed events, $\mu_{i,j}$ the number of expected events, and U_k the nuisance parameters. The distribution of the number of b-tagged jets observed in data and predicted in the simulation for the TCHEL operating point for $t\bar{t}$ and background events is shown in figure 15. The likelihood function for a given channel j is then the product of the likelihood functions over all the bins of the distribution:

$$\mathcal{L}_j(SF_b, \{N_{i,j}^{\text{obs}}\}, \{U_k\}) = \prod_i \mathcal{L}_{i,j}(SF_b, N_{i,j}^{\text{obs}}, \{U_k\}). \quad (6.2)$$

Since the decay channels are statistically independent, the overall likelihood function is then simply the product of the individual channel likelihoods:

$$\mathcal{L}(SF_b, \{N_{i,j}^{\text{obs}}\}, \{U_k\}) = \prod_j \mathcal{L}_j. \quad (6.3)$$

The expression of the profile likelihood ratio LR is then

$$LR(SF_b) = \frac{\mathcal{L}(SF_b, \{\hat{U}_i\})}{\mathcal{L}(\hat{SF}_b, \{\hat{U}_i\})}, \quad (6.4)$$

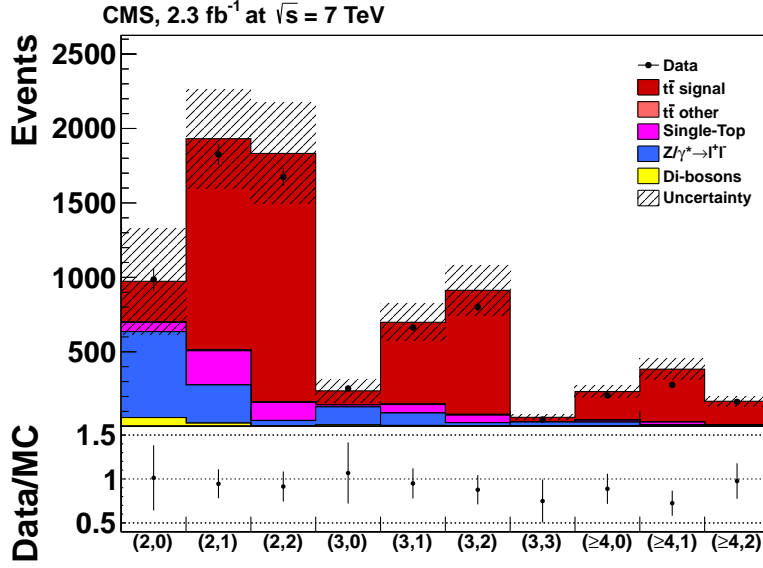


Figure 15. Number of b-tagged jets per event in the dilepton channel for the TCHEL operating point, in the data (filled circles) and the simulation (solid histograms), before the fit. The simulated distribution is normalized to an integrated luminosity of 2.3 fb^{-1} . The bin labels (m, n) refer to the number of events with m jets in the event of which n are tagged. The component “ $t\bar{t}$ signal” are the dilepton events, and the component “ $t\bar{t}$ other” contains the events in all other decay channels. The hatched area corresponds to the combined statistical and systematic uncertainty.

where \hat{U}_i represents the conditional maximum likelihood estimates of U_i obtained with the scale factor SF_b fixed while $\hat{S}F_b$ and \hat{U}_i are the estimates obtained with SF_b free.

The distribution of $-2 \ln(LR(SF_b))$ is asymptotically distributed as a χ^2 distribution with one degree of freedom (Wilk’s theorem [42]). An LR curve is obtained by scanning the values of SF_b in a given range and used to determine a 68% confidence level interval. These uncertainties are the combination of the statistical uncertainty and the systematic uncertainties considered as nuisance parameters. All the nuisance parameters are common to the three channels except the estimation of the backgrounds from data for W+jets and Z+jets. The Z+jets background is estimated from data as described in section 6.1. The small W+jets background is estimated from data using the matrix method [39].

The expected number of b-tagged jets in events with n jets of a given dilepton final state, $\mu_{i,j}$ in eq. (6.1), is derived from pre-tagged simulated events with n jets. This is carried out by applying per-jet b-jet tagging efficiencies, considering all jet tagging combinations. These efficiencies are derived as a function of p_T and η , using simulated $t\bar{t}$ events for b jets and using data samples dominated by light-parton jets. A constant scale factor SF_b is applied to the b- and c-jet efficiencies to model the b-jet tagging efficiency in data. The value of SF_b is then extracted by minimizing the LR as described above. A closure test is performed on simulated signal events to check that, for a unit scale factor, the b-tagged jet multiplicity distribution obtained with the reweighting procedure is the same as the one obtained directly from MC simulation using a requirement on the b-jet tagging discriminant.

Several uncertainties are considered as nuisance parameters in the likelihood function and are then fitted during the minimization procedure. These are the uncertainties on the energy scale of the jets and the leptons, the expected number of events of the different contributions, and the uncertainty on the light-parton jet scale factor.

Further contributions to the systematic uncertainties are estimated outside the PLR procedure. The expected input distributions to the PLR method are re-derived, using MC samples with varied parameters, and the b-jet tagging scale factors are re-measured. The relative differences of SF_b with respect to the nominal values are taken as systematic uncertainties, and added in quadrature to the total uncertainty from the fit. These uncertainties include the uncertainties on the jet-parton matching scale, the parton-shower/matrix-element threshold, and the top mass.

The factorization scale is the dominant systematic uncertainty, as it affects the jet multiplicity distribution, with a relative uncertainty of approximately 1.7% on the scale factor of the CSVL operating point. The second-largest contribution is from the uncertainty on the $t\bar{t}$ event yield, which is estimated to be 20%. It includes the uncertainties on the $t\bar{t}$ cross section, the trigger and lepton selection efficiencies, and the branching fraction of the decays of the W bosons. This results in an uncertainty of 1.4% on the scale factor of the CSVL operating point. Further, the statistical uncertainty on the b-jet tagging efficiency in the simulation was found to range between 0.4% and 1.6% depending on the operating point considered. A 1.6% systematic uncertainty on the scale factor was therefore chosen for all the operating points.

Finally, to account for a possible uncertainty coming from the fitting algorithm itself, an additional uncertainty is estimated using different choices of the likelihood minimization. This is taken as a 1% relative uncertainty.

6.4 Flavour tag consistency method

The FTC method requires consistency between the observed and expected number of tags in the lepton+jets events to study the performance of the heavy-flavour algorithms.

In a sample of $t\bar{t}$ pair candidates in the lepton+jets channel, the expected number of events with n b-tagged jets $\langle N_n \rangle$ can be written as

$$\langle N_n \rangle = L \cdot \sigma_{t\bar{t}} \cdot \varepsilon \cdot \sum_{i,j,k} F_{ijk} \sum_{i'+j'+k'=n}^{i' \leq i, j' \leq j, k' \leq k} [C_i^{i'} \varepsilon_b^{i'} (1 - \varepsilon_b)^{(i-i')} C_j^{j'} \varepsilon_c^{j'} (1 - \varepsilon_c)^{(j-j')} C_k^{k'} \varepsilon_l^{k'} (1 - \varepsilon_l)^{(k-k')}], \quad (6.5)$$

where L is the integrated luminosity, $\sigma_{t\bar{t}}$ is the $t\bar{t}$ cross section, ε is the pre-tagging selection efficiency, C_a^b is the binomial coefficient, and $\varepsilon_b, \varepsilon_c$, and ε_l are the b-, c-, and light-parton jet tagging efficiencies. The factors F_{ijk} are the fractions of events with i b jets, j c jets, and k light-parton jets. They are derived from the $t\bar{t}$ simulation in which the true flavour of the jets is known.

As an example, the F_{112} term contributes to the expected number of events with 1 b-tagged jet $\langle N_1 \rangle$ in the following way:

$$\langle N_1 \rangle \propto F_{112} \times \left(\underbrace{1 \cdot \varepsilon_b (1 - \varepsilon_c) (1 - \varepsilon_l)^2}_{\text{the b jet}} + \underbrace{1 \cdot (1 - \varepsilon_b) \varepsilon_c (1 - \varepsilon_l)^2}_{\text{the c jet}} + \underbrace{2 \cdot (1 - \varepsilon_b) (1 - \varepsilon_c) \varepsilon_l (1 - \varepsilon_l)}_{\text{the light-parton jet}} \right). \quad (6.6)$$

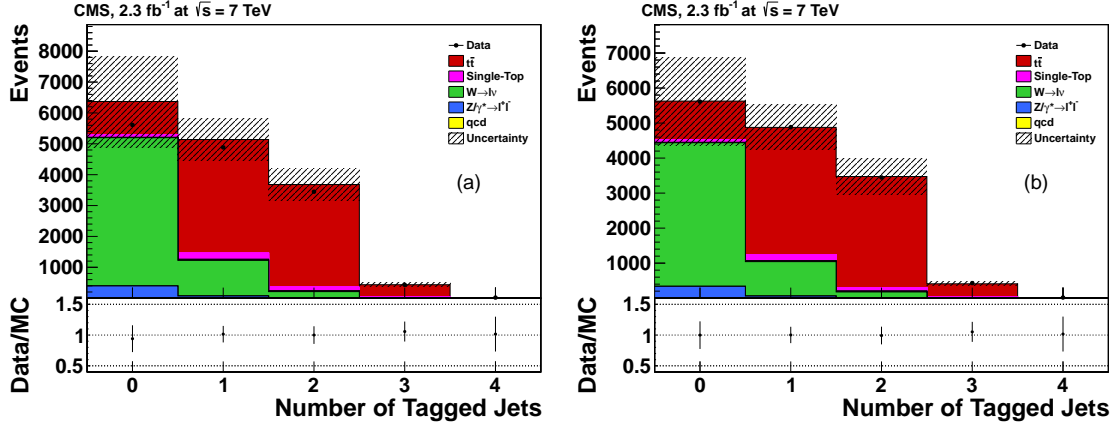


Figure 16. Number of tagged jets per event in the lepton+jet channel with the FTC method with the CSVM operating point, in the data (filled circles) and the simulation (solid histograms), (a) before and (b) after the fit. The simulated distribution is normalized to an integrated luminosity of 2.3 fb^{-1} . The hatched area corresponds to the combined statistical and systematic uncertainty.

To account for the non-negligible amount of background, eq. (6.5) is modified to include each background sample:

$$\begin{aligned}
 \langle N_n \rangle &= \langle N_n^{\text{t}\bar{\text{t}}} \rangle + \langle N_n^{\text{background}} \rangle \\
 &= L \cdot \sigma_{\text{t}\bar{\text{t}}} \cdot \epsilon_{\text{t}\bar{\text{t}}} \cdot \left[\sum_{i,j,k} F_{ijk}^{\text{t}\bar{\text{t}}} \sum_{i'+j'+k'=n}^{i' \leq i, j' \leq j, k' \leq k} (\dots) \right. \\
 &\quad \left. + \frac{\sigma_{\text{background}}}{\sigma_{\text{t}\bar{\text{t}}}} \cdot \frac{\epsilon_{\text{background}}}{\epsilon_{\text{t}\bar{\text{t}}}} \cdot \sum_{i,j,k} F_{ijk}^{\text{background}} \sum_{i'+j'+k'=n}^{i' \leq i, j' \leq j, k' \leq k} (\dots) \right], \quad (6.7)
 \end{aligned}$$

where (\dots) stands for the expression in square brackets from eq. (6.5).

The tagging efficiencies and the $\text{t}\bar{\text{t}}$ production cross section are then measured by minimizing the log-likelihood function:

$$\mathcal{L} = -2 \log \prod_n \text{Poisson}(N_n, \langle N_n \rangle), \quad (6.8)$$

where N_n is the number of observed events with n b-tagged jets. The distribution of the number of b-tagged jets observed in data and predicted in the simulation before and after the fit for $\text{t}\bar{\text{t}}$ and background events is shown in figure 16.

In the current implementation the likelihood only uses the b-tagged jet multiplicity in $\text{t}\bar{\text{t}}$ lepton+jets events with between four to seven reconstructed jets, as it emphasizes the measurement of the heavy-flavour b-jet tagging efficiency. The b-jet tagging efficiencies and $\text{t}\bar{\text{t}}$ cross section are treated as free parameters in the fit. The $\text{t}\bar{\text{t}}$ cross section determined in the fits are consistent with the published values. The c- and light-parton-jet tagging efficiencies are taken from the simulation corrected for the data/MC scale factors.

The systematic uncertainties are determined from ensembles of pseudo-experiments. In each of these pseudo-experiments, the number of signal and background events are generated using

Poisson statistics, using as mean values the number of expected events in each channel. Events are then randomly chosen in the simulated samples and the b-tagged jet multiplicity distributions are populated according to the simulated jet multiplicity in each event. The measurement is then performed as described above using the factors F_{ijk} from the nominal simulation. The average b-jet tagging efficiency is compared to the average b-jet tagging efficiency value measured in ensemble tests with the nominal samples. The difference is taken as a systematic uncertainty.

The dominant contribution is the uncertainty on the jet energy scale, with a relative uncertainty of 2.2% on the scale factor of the CSVL operating point. The second-largest uncertainty arises from the uncertainty on the production cross section of the W+heavy flavour jets, with a relative uncertainty of 0.97%. The uncertainties due to the factorization scale and the jet-parton matching are 0.41% and 0.35%, respectively, for the CSVL operating point.

6.5 Flavour tag matching method

The FTM method requires consistency between the observed and expected number of tags in dilepton events. The expected number of events with n b-tagged jets $\langle N_n \rangle$ is written as

$$\langle N_n \rangle = \sum_{k \text{ jets}=2}^{\text{all jets}} n_k \cdot P_{n,k} , \quad (6.9)$$

where n_k is the observed number of events with k jets, and $P_{n,k}$ is the probability to count n b-tagged jets in a k -jet event. These probability functions are written in terms of the tagging efficiencies and the expected jet composition.

In order to illustrate explicitly the construction of the probability functions, the exclusive two-jet multiplicity bin is used and the following expression is obtained:

$$P_{n,2} = \sum_{\substack{i \text{ jets}=0 \\ \text{from top decay}}}^2 \alpha_i \cdot P_{n,2,i} , \quad (6.10)$$

where $P_{n,2,i}$ is the probability that n b tags are observed in an event with two jets of which i jets come from $t\bar{t}$ decays.

The misassignment probabilities α_i denote the probability in the sample that i jets from the decay of the $t\bar{t}$ pair have been reconstructed and selected. These are normalized such that $\sum_i \alpha_i = 1$. For example, α_2 is the probability that both b jets from the $t\bar{t}$ decay have been selected. They take into account both the contribution from the background, which is small in the dilepton channel, and jet misassignment. Either or both of the jets from the decays of the two top quarks may not be selected, and jets from initial- and final- state radiation, or jets from the proton recoil may enter the selection, further diluting the sample.

As an example, for the case where two tagged jets are found in a two-jet event, the probabilities can be explicitly written as:

$$\begin{aligned} P_{2,2,0} &= \epsilon_q^2 && \text{if no jets are from } t\bar{t} \text{ decays;} \\ P_{2,2,1} &= 2\epsilon_b\epsilon_q && \text{if 1 jet is from } t\bar{t} \text{ decays;} \\ P_{2,2,2} &= \epsilon_b^2 && \text{if 2 jets are from } t\bar{t} \text{ decays.} \end{aligned} \quad (6.11)$$

The misidentification probability ε_q is an effective measurement of the probability of tagging gluon, light and charm quark jets in the dilepton sample. Similar expressions can easily be derived for the other jet multiplicity bins.

The misassignment probabilities are determined from data, and used in the subsequent likelihood of the b-tagged jet multiplicity distribution. In order to estimate the actual fraction of b jets from top-quark decays in the selected sample, kinematic properties of the top decay topology are used. The invariant mass of the lepton-jet pairs from a $t \rightarrow Wb$ decay have a kinematic end-point at $M_{\ell,b}^{\max} \equiv \sqrt{m_t^2 - m_W^2} \approx 156 \text{ GeV}/c^2$. The invariant mass of misassigned lepton-jet pairs exhibits a longer tail towards high mass values. The shape of the misassigned pairs can be modelled by mixing lepton-jet pairs from different events or randomly changing the lepton momentum direction. The fraction of jets from $t \rightarrow Wb$ decays can thus be measured normalizing the spectrum obtained from the combinatorial model to the number of pairs observed in the tail (i.e. $M_{\ell,b} > 180 \text{ GeV}/c^2$). This is estimated independently for each dilepton channel and for each jet-multiplicity bin. The procedure is checked and found to be unbiased from MC pseudo-experiments. Taking into account the expected contribution of $t\bar{t}$ and single-top events to the final sample, the sample composition in terms of events with 2, 1, or 0 correctly reconstructed and selected b jets is estimated.

The b-jet tagging efficiency ε_b can then be measured by maximizing the likelihood function:

$$\mathcal{L}(\varepsilon_b, \varepsilon_q, \alpha_i) = \prod_{n=0}^{\text{all jets}} \text{Poisson}(N_n, \langle N_n \rangle), \quad (6.12)$$

where N_n is the observed number of events with n b-tagged jets.

The likelihood only uses the b tagged jet multiplicity in $t\bar{t}$ dilepton events with two and three reconstructed jets. Gaussian constraints are added for the effective c- and light-parton jet tagging efficiency ε_q and the misassignment probabilities:

$$\mathcal{L} = \prod_{n=0}^{\text{all jets}} \text{Poisson}(N_n, \langle N_n \rangle) \cdot \prod_i \text{Gauss}(\alpha_i, \hat{\alpha}_i, \sigma_{\alpha_i}) \cdot \text{Gauss}(\varepsilon_q, \hat{\varepsilon}_q, \sigma_{\varepsilon_q}). \quad (6.13)$$

The central value $\hat{\varepsilon}_q$ and width σ_{ε_q} of ε_q are determined from the simulation. For the misassignment probabilities α_i , the central values $\hat{\alpha}_i$ are taken from the measurement described above, and the width σ_{α_i} derived from the uncertainty of the expected contribution of $t\bar{t}$ and single-top events to the final sample.

The systematic uncertainties affect the measurement of the b-jet tagging probability through their effect on the parameters of the fit, namely the measured misassignment probabilities and the misidentification probability for non-b jets. The effect on the measured misassignment probabilities is determined from ensembles of pseudo-experiments, where, for each source of uncertainty, the bias on the probabilities is determined. Most sources of uncertainties such as jet energy scale and resolution, and pileup have little effect. This is because the method used to derive the misassignment probabilities is based on templates for the lepton-jet invariant mass obtained from control samples in data. Other sources, which might affect the contribution from top-quark decays and from initial- and final-state radiation jets to the final sample, are evaluated using samples where the QCD factorisation and renormalisation scales and the jet-parton matching scales are varied. In the pseudo-experiments the standard $t\bar{t}$ sample is substituted by each of these samples and the process is repeated.

This bias is then used to shift the measured misassignment probabilities. The likelihood fit of the data is repeated with the modified values. The difference with respect to the nominal result is taken as the systematic uncertainty. The same procedure is applied to evaluate the uncertainty on the misidentification probability for non-b jets.

The final uncertainty is dominated by factors which tend to increase the contamination of background or alter the jet environment. The main uncertainties are the factorization scale, and to a smaller extent, the jet-parton matching with relative uncertainties on the scale factor of 2.3% and 1.4% respectively, for the CSVL operating point. The second-largest uncertainty arises from the 1.5% uncertainty on the light-parton jet tagging efficiency.

6.6 Efficiency measurement from a b-enriched jet sample

In this method, the b-jet tagging efficiency is measured from a sample enriched with b jets (bSample) in lepton+jets events. The contamination of this sample due to light-parton jets is estimated from data and subtracted.

In order to select the correct jets originating from the decay of the top quarks, a χ^2 is calculated for each jet-parton combination based on the masses of the reconstructed W boson m_{qq} and the hadronically decaying top quark m_{bqq} :

$$\chi^2 = \left(\frac{m_{bqq} - m_t}{\sigma_t} \right)^2 + \left(\frac{m_{qq} - m_W}{\sigma_W} \right)^2. \quad (6.14)$$

The mean masses and widths are obtained from the $t\bar{t}$ simulation using a Gaussian fit to the mass distributions of the combination with the correct jet-to-quark assignment. The mean and width of the reconstructed top-quark mass distribution are $172.5 \text{ GeV}/c^2$ and $16.3 \text{ GeV}/c^2$, respectively. The mean and width of the reconstructed W-boson distribution are $82.9 \text{ GeV}/c^2$ and $9.5 \text{ GeV}/c^2$, respectively. Using the four leading jets, with transverse momenta above $30 \text{ GeV}/c$, there are 12 combinations to pair the four reconstructed jets with the quarks from $t\bar{t}$ decay. The combination with the lowest χ^2 is selected to represent the event topology. The event is rejected if the lowest χ^2 is above 90.

A generic b-candidate sample is constructed by taking the jet assigned to the lepton. This sample is further subdivided into b-enriched and b-depleted subsamples by using the invariant mass of that jet and the muon (called the jet-muon mass, $m_{\mu j}$). The distribution of this variable is shown in figure 17. For the b-enriched subsample, the jet-muon mass is required to be in the range $80 < m_{\mu j} < 150 \text{ GeV}/c^2$. For the b-depleted subsample the jet-muon mass is required to be in the range $150 < m_{\mu j} < 250 \text{ GeV}/c^2$. Based on the simulation, the purities of the two subsamples are 45% and 16%, respectively.

The distribution of the discriminators of the taggers for true b jets, $\hat{\Delta}_b^{\text{enr}}$, is obtained by subtracting the discriminator distribution of the b-depleted subsample, Δ_b^{depl} from the discriminator distribution of the b-enriched subsample, Δ_b^{enr} :

$$\hat{\Delta}_b^{\text{enr}} = \Delta_b^{\text{enr}} - F \times \Delta_b^{\text{depl}}. \quad (6.15)$$

The factor F represents the ratio of the number of non-b jets in the b-enriched and b-depleted subsamples. It is measured from a background dominated sample composed mainly of light-flavour

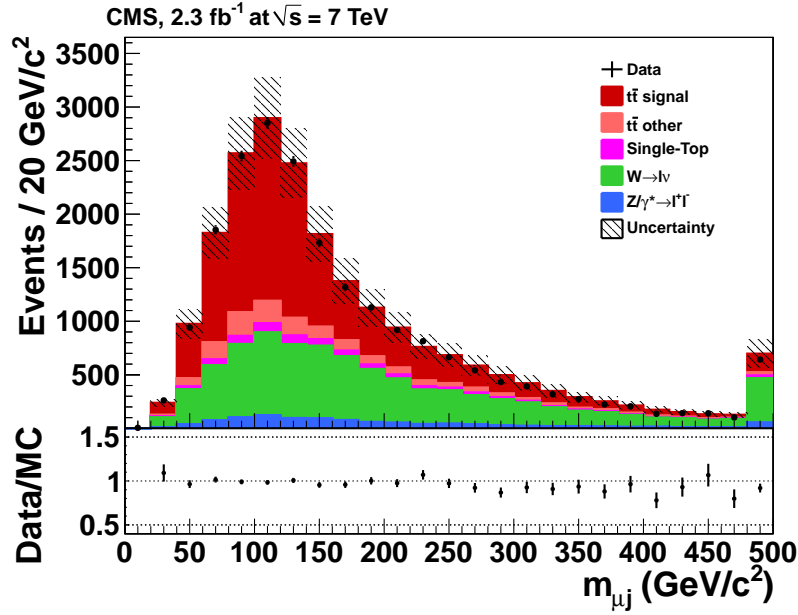


Figure 17. Distribution of the jet-muon mass in the data (filled circles) and the simulation (solid histograms). The simulated distribution is normalized to an integrated luminosity of 2.3 fb^{-1} . The component “ $t\bar{t}$ signal” stands for the lepton+jet events. The component “ $t\bar{t}$ other” contains the events in all other decay channels. The hatched area corresponds to the combined statistical and systematic uncertainty. Overflow entries are added to the last bin.

quark jets. This sample is obtained by using the jets attributed to the decay of the W boson and ensuring that they both fail the b-jet tagging requirements of the TCHEM operating point. Both jets are used to construct a jet-muon mass distribution, and the same subsamples are defined as for the signal sample. The purity of light-flavour quark jets is 92% in the region $80 < m_{\mu j} < 150 \text{ GeV}/c^2$ and 95% in the region $150 < m_{\mu j} < 250 \text{ GeV}/c^2$. To match the shape of the jet-muon mass distribution of this background sample to that of the signal sample, the jets in the background sample are reweighted according to the (p_T, η) of the signal sample. After this reweighting, the two samples have similar jet-muon mass distribution. The factor F is taken as the ratio of the number of events in the $80 < m_{\mu j} < 150 \text{ GeV}/c^2$ and the $150 < m_{\mu j} < 250 \text{ GeV}/c^2$ regions in the background sample, and is found to be 1.16 ± 0.02 .

A small correlation between the jet-muon mass and the discriminators has to be corrected for. This correlation is attributed to the correlation between the transverse momentum of the jet and the jet-muon mass. This correlation distorts the distribution of the discriminants of the b-jet tagging algorithms in the b-depleted subsample with respect to the distribution of the non-b jets in the b-enhanced subsample. This effect is corrected by reweighting the jets in the b-depleted subsample according to the transverse momentum distribution of the jets in the b-enhanced subsample.

The systematic uncertainties for the b-jet tagging efficiency and the scale factors are the absolute differences between the nominal simulation sample and the sample with modified parameters. Additionally, a systematic uncertainty is assigned based on tests of the method in simulation. The tests show no bias in the method with an uncertainty driven by statistical uncertainties on available

Table 7. Data/MC scale factors SF_b as measured using the PtRel, System8, and LT methods and their combination. Results are given for jet p_T between 80 and 120 GeV/c. The first uncertainty on SF_b is statistical and the second is systematic. For the combination the total uncertainty is quoted.

| b tagger | SF_b (PtRel) | SF_b (System8) | SF_b (LT) | SF_b (comb.) |
|----------|--------------------------|--------------------------|--------------------------|-----------------|
| JPL | $0.98 \pm 0.01 \pm 0.03$ | $1.00 \pm 0.02 \pm 0.07$ | $1.00 \pm 0.01 \pm 0.04$ | 0.99 ± 0.03 |
| JBPL | $0.99 \pm 0.01 \pm 0.02$ | $0.98 \pm 0.02 \pm 0.04$ | $1.01 \pm 0.01 \pm 0.04$ | 0.99 ± 0.02 |
| TCHL | $0.99 \pm 0.01 \pm 0.02$ | $0.97 \pm 0.02 \pm 0.05$ | $1.00 \pm 0.01 \pm 0.01$ | 1.00 ± 0.01 |
| CSVL | $1.00 \pm 0.01 \pm 0.02$ | $1.01 \pm 0.02 \pm 0.06$ | $0.98 \pm 0.01 \pm 0.02$ | 0.99 ± 0.02 |
| JPM | $0.90 \pm 0.01 \pm 0.03$ | $0.93 \pm 0.03 \pm 0.06$ | $0.99 \pm 0.01 \pm 0.05$ | 0.92 ± 0.03 |
| JBPM | $0.92 \pm 0.01 \pm 0.02$ | $0.96 \pm 0.03 \pm 0.08$ | $0.99 \pm 0.01 \pm 0.05$ | 0.91 ± 0.03 |
| TCHM | $0.94 \pm 0.01 \pm 0.03$ | $0.99 \pm 0.03 \pm 0.07$ | $0.98 \pm 0.01 \pm 0.03$ | 0.95 ± 0.02 |
| TCHPM | $0.95 \pm 0.01 \pm 0.03$ | $0.94 \pm 0.02 \pm 0.09$ | $0.97 \pm 0.01 \pm 0.02$ | 0.96 ± 0.02 |
| SSVHEM | $0.92 \pm 0.01 \pm 0.02$ | $0.92 \pm 0.03 \pm 0.05$ | $0.97 \pm 0.01 \pm 0.02$ | 0.95 ± 0.02 |
| CSVM | $0.93 \pm 0.01 \pm 0.02$ | $0.97 \pm 0.03 \pm 0.06$ | $0.97 \pm 0.01 \pm 0.03$ | 0.95 ± 0.02 |
| JPT | $0.82 \pm 0.01 \pm 0.05$ | $0.85 \pm 0.03 \pm 0.07$ | $0.96 \pm 0.01 \pm 0.07$ | 0.87 ± 0.05 |
| JBPT | $0.83 \pm 0.01 \pm 0.06$ | $0.89 \pm 0.03 \pm 0.11$ | $0.96 \pm 0.01 \pm 0.08$ | 0.87 ± 0.06 |
| TCHPT | $0.87 \pm 0.01 \pm 0.05$ | $0.91 \pm 0.03 \pm 0.10$ | $0.94 \pm 0.01 \pm 0.04$ | 0.91 ± 0.04 |
| SSVHPT | $0.87 \pm 0.01 \pm 0.03$ | $0.84 \pm 0.03 \pm 0.10$ | $0.96 \pm 0.01 \pm 0.03$ | 0.92 ± 0.03 |
| CSVT | $0.86 \pm 0.01 \pm 0.04$ | $0.92 \pm 0.03 \pm 0.07$ | $0.94 \pm 0.01 \pm 0.04$ | 0.90 ± 0.03 |

samples. For the CSVL operating point, the relative uncertainty is 3.1%. The jet energy scale and resolution have a small contribution from the change in the mean masses and widths used for the χ^2 . For the CSVL operating point, the relative uncertainties on the scale factor are 1.4% and 2.2%, respectively. A small uncertainty of 0.5% is due to the choice of the boundaries of the b-depleted region. The high tail of the jet-muon mass distribution is composed mainly of background events and wrongly combined jets that do not reflect the kinematics of the signal events. The effect of imposing an upper limit on the region is assessed by varying the boundary between 200 and 300 GeV/c².

7 Efficiency measurement results

7.1 Results from multijet events

The methods described in section 5 cover a large range of jet transverse momenta. The PtRel and the System8 methods provide precise measurements for the lower part of the spectrum. The IP3D and the LT methods have been designed for high jet p_T . The measured data/MC scale factors are given in table 7 for jets with low p_T from 80 to 120 GeV/c, and in table 8 for jets with high p_T , from 160 to 320 GeV/c. In these ranges the methods give compatible results within the quoted uncertainties. While some of the methods measure the efficiencies and scale factors only for muon jets, and not inclusive b jets, simulation studies have shown that the difference in tagging efficiencies between the two are only a few percent. We assume that these small differences have no significant effect on the scale factors, which are relative data/MC measurements.

Table 8. Data/MC scale factors SF_b as measured using the IP3D and LT methods and their combination. Results are given for jet p_T between 160 and 320 GeV/c. The first uncertainty on SF_b is statistical and the second is systematic. For the combination the total uncertainty is quoted.

| b tagger | SF_b (IP3D) | SF_b (LT) | SF_b (comb.) |
|----------|--------------------------|--------------------------|-----------------|
| JPL | $0.99 \pm 0.01 \pm 0.01$ | $1.00 \pm 0.01 \pm 0.06$ | 0.99 ± 0.02 |
| JBPL | $1.00 \pm 0.01 \pm 0.01$ | $1.00 \pm 0.01 \pm 0.05$ | 1.00 ± 0.02 |
| TCHL | $1.00 \pm 0.01 \pm 0.02$ | $1.00 \pm 0.01 \pm 0.02$ | 1.00 ± 0.02 |
| CSVL | $0.98 \pm 0.02 \pm 0.01$ | $0.96 \pm 0.01 \pm 0.04$ | 0.97 ± 0.03 |
| JPM | $0.93 \pm 0.02 \pm 0.03$ | $0.99 \pm 0.01 \pm 0.06$ | 0.95 ± 0.04 |
| JBPM | $0.97 \pm 0.02 \pm 0.03$ | $0.99 \pm 0.01 \pm 0.06$ | 0.97 ± 0.04 |
| TCHM | $0.96 \pm 0.02 \pm 0.03$ | $0.97 \pm 0.01 \pm 0.03$ | 0.96 ± 0.03 |
| TCHPM | $0.97 \pm 0.02 \pm 0.03$ | $0.97 \pm 0.01 \pm 0.02$ | 0.97 ± 0.02 |
| SSVHEM | $0.98 \pm 0.02 \pm 0.04$ | $0.98 \pm 0.01 \pm 0.07$ | 0.98 ± 0.04 |
| CSVM | $0.95 \pm 0.02 \pm 0.04$ | $0.97 \pm 0.01 \pm 0.06$ | 0.96 ± 0.04 |
| JPT | $0.89 \pm 0.02 \pm 0.04$ | $0.95 \pm 0.01 \pm 0.10$ | 0.91 ± 0.05 |
| JBPT | $0.91 \pm 0.02 \pm 0.03$ | $0.96 \pm 0.01 \pm 0.11$ | 0.92 ± 0.05 |
| TCHPT | $0.89 \pm 0.02 \pm 0.03$ | $0.94 \pm 0.01 \pm 0.04$ | 0.92 ± 0.04 |
| SSVHPT | $0.92 \pm 0.02 \pm 0.04$ | $0.96 \pm 0.01 \pm 0.05$ | 0.94 ± 0.04 |
| CSVT | $0.90 \pm 0.02 \pm 0.07$ | $0.94 \pm 0.01 \pm 0.09$ | 0.92 ± 0.07 |

The results have been combined to provide the best measurements of the data/MC scale factors for $30 < p_T < 670$ GeV/c. For each jet p_T range the most precise results have been used: the PtRel and System8 methods for $p_T < 120$ GeV/c, the IP3D method for $p_T > 120$ GeV/c and the LT method for the full momentum range.

The combination is based on a weighted mean of the scale factors in each jet p_T bin [43]. However, there are a significant number of jets from QCD dijet and multijet events (with at least one muon associated to a jet) which are shared between the methods. The shared fraction of jets varies with jet p_T . Typical values are 10–25% between the LT and PtRel/IP3D methods, 40–50% between the PtRel and System8 methods, and 20–50% between the System8 and LT methods. This overlap has been taken into account in the combination.

Several sources of systematic uncertainties are common for all methods: the effects due to pileup, gluon splitting, and the selection criteria for muons. The muon PtRel and IP3D methods have the same sensitivity to the choice of the away-jet tagger. The corresponding uncertainties were assumed to be fully correlated or anticorrelated according to the sign of the variations observed for the different methods. All other systematic effects are specific to individual methods and have been treated as uncorrelated. A conservative value for the uncertainty is used if the χ^2 from the fit exceeds the number of degrees of freedom, in which case the uncertainty is scaled by the square root of the normalised χ^2 . Summaries for the individual and combined scale factor measurements for the JPL and the CSVM taggers are shown in figure 18. Also shown are the parameterizations of the combined scale factor of the form $SF_b(p_T) = \alpha(1 + \beta p_T)/(1 + \gamma p_T)$. Combined values for a low and a high jet p_T range are shown in the right hand columns of tables 7 and 8, respectively. The same studies have been performed separately for muon jets with $|\eta| < 1.2$ and $1.2 < |\eta| < 2.4$. Compatible scale factor values are obtained in both regions.

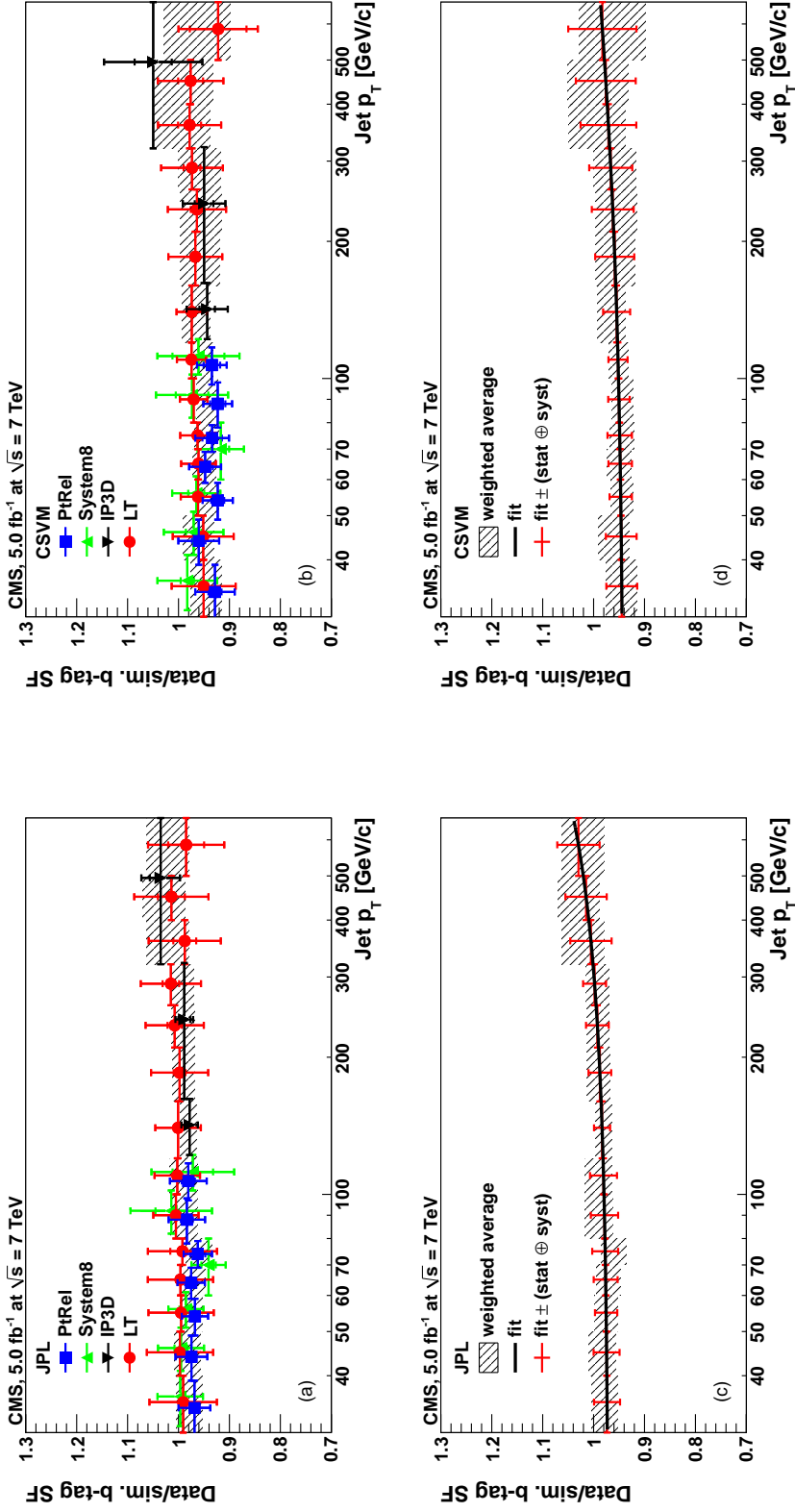


Figure 18. Individual and combined measurements of the ratio of the b-jet tagging efficiencies of the data to that in simulation for the (a, c) JPL and (b, d) CSVm taggers. Figures (a) and (b) show the individual measurements from the muon p_T^{rel} (“PtRel”), System8 (“System8”), muon IP (“IP3D”), and lifetime tagger (“LT”) methods. The inner and outer error bars indicate the statistical and the combined uncertainties, respectively. The hatched areas represent the combined measurements. In figures (c) and (d) the combined measurements have been parameterized by functions of the form $SF_b(p_T) = \alpha(1 + \beta p_T)/(1 + \gamma p_T)$. The error bars attached to the function have the same size as the uncertainties from the combined measurement in each bin.

Table 9. The scale factors SF_b as measured using the PLR, FTC, FTM and bSample methods, and the weighted mean (WM). The uncertainties are the combined statistical and systematic uncertainty.

| b tagger | PLR | FTC | FTM | bSample | WM |
|----------|-----------------|-----------------|-----------------|-----------------|-----------------|
| JPL | 0.96 ± 0.03 | 0.99 ± 0.03 | 0.96 ± 0.03 | 0.96 ± 0.05 | 0.97 ± 0.03 |
| JBPL | 0.97 ± 0.03 | 1.00 ± 0.05 | 0.96 ± 0.03 | 0.97 ± 0.05 | 0.98 ± 0.03 |
| TCHL | 0.96 ± 0.03 | 0.94 ± 0.04 | 0.95 ± 0.03 | 0.92 ± 0.05 | 0.95 ± 0.03 |
| CSVL | 1.00 ± 0.03 | 1.03 ± 0.03 | 0.99 ± 0.04 | 0.97 ± 0.05 | 1.01 ± 0.03 |
| JPM | 0.95 ± 0.03 | 0.95 ± 0.04 | 0.93 ± 0.03 | 0.94 ± 0.06 | 0.95 ± 0.03 |
| JBPM | 0.93 ± 0.03 | 0.95 ± 0.04 | 0.91 ± 0.03 | 0.93 ± 0.06 | 0.94 ± 0.03 |
| TCHM | 0.96 ± 0.03 | 0.97 ± 0.04 | 0.96 ± 0.03 | 0.93 ± 0.06 | 0.96 ± 0.03 |
| TCHPM | 0.94 ± 0.03 | 0.93 ± 0.04 | 0.95 ± 0.04 | 0.92 ± 0.06 | 0.93 ± 0.03 |
| SSVHEM | 0.95 ± 0.03 | 0.98 ± 0.04 | 0.98 ± 0.04 | 0.95 ± 0.07 | 0.96 ± 0.03 |
| CSVM | 0.97 ± 0.03 | 0.98 ± 0.04 | 0.97 ± 0.04 | 0.95 ± 0.06 | 0.97 ± 0.03 |
| JPT | 0.90 ± 0.03 | 0.89 ± 0.05 | 0.90 ± 0.03 | 0.95 ± 0.07 | 0.90 ± 0.03 |
| JBPT | 0.90 ± 0.03 | 0.88 ± 0.05 | 0.90 ± 0.03 | 0.90 ± 0.07 | 0.89 ± 0.03 |
| TCHPT | 0.93 ± 0.03 | 0.92 ± 0.05 | 0.94 ± 0.04 | 0.91 ± 0.07 | 0.93 ± 0.03 |
| SSVHPT | 0.95 ± 0.03 | 0.95 ± 0.04 | 0.96 ± 0.04 | 0.89 ± 0.07 | 0.95 ± 0.03 |
| CSVT | 0.95 ± 0.03 | 0.97 ± 0.05 | 0.96 ± 0.03 | 0.95 ± 0.06 | 0.96 ± 0.03 |

7.2 Results from $t\bar{t}$ events

The statistical properties of the four methods presented in sections 6.3 to 6.6 have been studied using ensembles of pseudo-experiments based on the expected numbers of signal and background events. The distributions of the estimated values and their uncertainties show that the methods are unbiased. This is shown by the pull distributions, which have mean values close to zero and standard deviations close to one.

The scale factors $SF_b = \epsilon_b^{\text{meas}} / \epsilon_b^{\text{MC}}$ measured with the different algorithms are shown in table 9 using data with an integrated luminosity of 2.3 fb^{-1} . The scale factors were stable over the whole data-taking period and can be applied to the full dataset. The measured b-jet tagging efficiencies and scale factors for the CSV algorithm are shown in figure 19.

The PLR and FTC methods are used to calculate a combined scale factor for use in analyses, by taking the weighted mean of the scale factors from each method. The two methods are chosen because each has the smallest uncertainty among the analyses in its respective decay channel. By choosing one analysis in the dilepton channel and one in the lepton+jets channel, there is no statistical correlation between the two measurements as the samples are mutually exclusive. Based on the statistical and systematic uncertainties of the PLR and FTC methods, the uncertainty of the resulting scale factor is ± 0.03 for all operating points.

A continuous function for the scale factors is required in physics analyses that use b-jet tagging discriminators with multivariate methods. The function is obtained from a linear fit to the distribution of the scale factors measured with the FTC method. This is offset vertically to match the weighted mean of the medium operating point, as illustrated in figure 20.

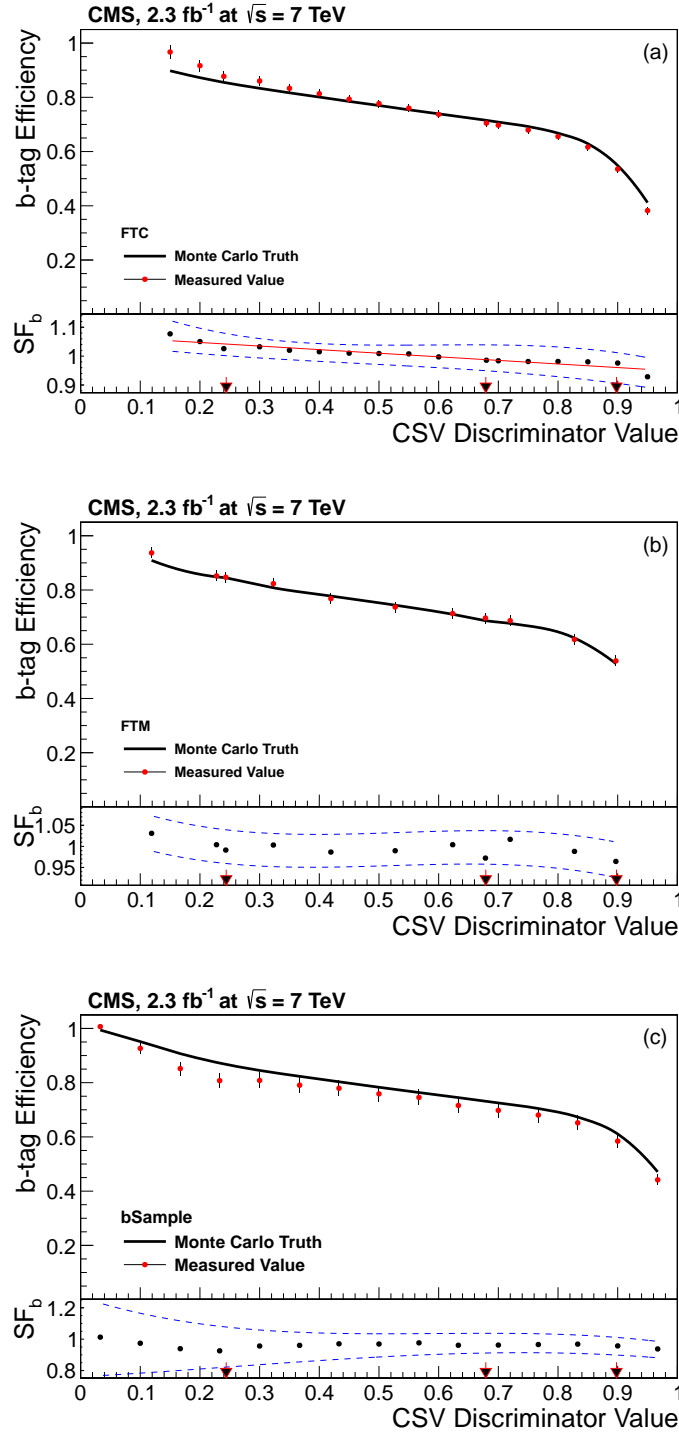


Figure 19. Measured b-jet tagging efficiency as a function of the flavour discriminator threshold for the CSV algorithm, measured with the (a) FTC method, (b) FTM method and (c) bSample method. The absolute b-jet tagging efficiencies measured from data and predicted from simulation are shown in the upper histograms of each panel. The scale factors SF_b are shown in the lower histogram, where the blue dashed lines represent the combined statistical and systematic uncertainty. The arrows indicate the standard operating points. For the FTC method, the red line represents a linear function fitted on the distribution of the scale factors.

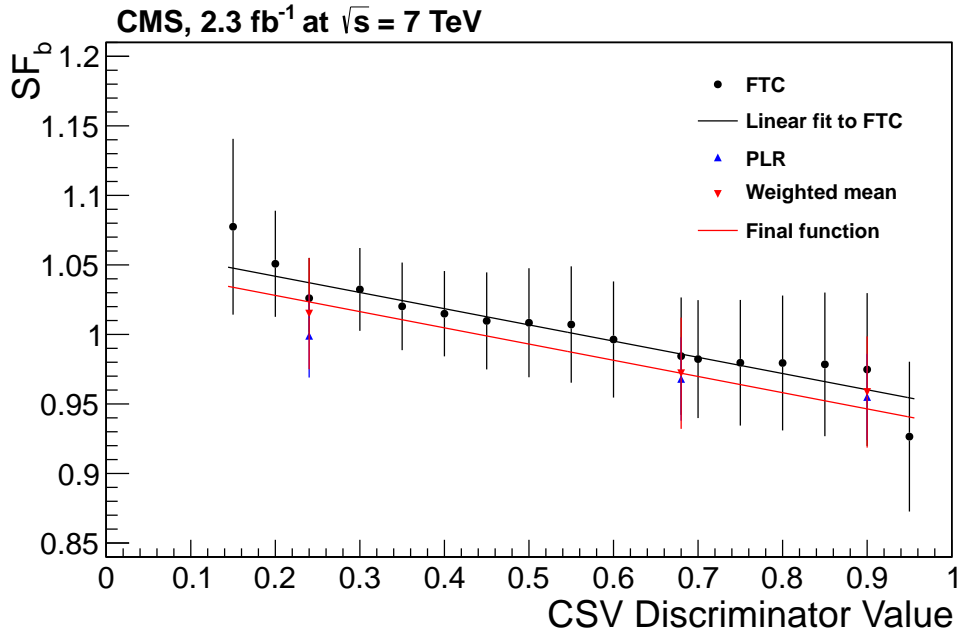


Figure 20. Scale factors measured with the PLR and FTC methods and weighted mean as a function of the discriminator threshold for the CSV algorithm. The black function is derived from a fit to the values measured with the FTC method. The red function labelled “Final function” corresponds to the same function offset vertically to match the weighted mean of the medium operating point. The uncertainties are the combined statistical and systematic uncertainty.

7.3 Comparison of results

The p_T -dependent scale factors measured in dijet and multijet events have been compared by reweighted them to match the jet p_T spectrum observed in $t\bar{t}$ events. The results are shown in table 10 and are in good agreement with each other. This justifies the assumption that the scale factors for the muon jets and inclusive jets are compatible.

8 Misidentification probability measurement

The measurement of the misidentification probability for light-parton jets relies on the definition of inverted tagging algorithms, selecting non- b jets using the same variables and techniques as the standard versions. These “negative taggers” can be used in the same way as the regular b -jet tagging algorithms both in data and in the simulation. As the negative-tagged jets are enriched in light flavours, the misidentification probability can be measured from data, with the simulation used to extract a correction factor.

The misidentification probability is evaluated from tracks with a negative impact parameter or from secondary vertices with a negative decay length (see section 4). When a negative tagger is applied to jets of any flavour, the corresponding tagging efficiency is denoted “negative tag rate”. The negative and positive b -jet tagging discriminator distributions in data are compared with the simulation in figure 21. The events are selected by requiring jet triggers with a p_T threshold of

Table 10. The efficiency scale factors SF_b , and their uncertainties, obtained in multijet and $t\bar{t}$ events for b jets in the expected p_T range of $t\bar{t}$ events.

| b tagger | SF_b in multijet events | SF_b in $t\bar{t}$ events |
|----------|---------------------------|-----------------------------|
| JPL | 0.98 ± 0.02 | 0.97 ± 0.03 |
| JBPL | 0.98 ± 0.02 | 0.98 ± 0.03 |
| TCHL | 0.98 ± 0.02 | 0.95 ± 0.03 |
| CSVL | 0.99 ± 0.02 | 1.01 ± 0.03 |
| JPM | 0.92 ± 0.03 | 0.95 ± 0.03 |
| JBPM | 0.92 ± 0.03 | 0.94 ± 0.03 |
| TCHEM | 0.95 ± 0.03 | 0.96 ± 0.03 |
| TCHPM | 0.94 ± 0.03 | 0.93 ± 0.03 |
| SSVHEM | 0.95 ± 0.03 | 0.96 ± 0.03 |
| CSVM | 0.95 ± 0.03 | 0.97 ± 0.03 |
| JPT | 0.87 ± 0.04 | 0.90 ± 0.03 |
| JBPT | 0.87 ± 0.05 | 0.89 ± 0.03 |
| TCHPT | 0.91 ± 0.04 | 0.93 ± 0.03 |
| SSVHPT | 0.92 ± 0.03 | 0.95 ± 0.03 |
| CSVT | 0.91 ± 0.03 | 0.96 ± 0.03 |

30 GeV/c, corresponding to an average p_T over all jets in the events of 44 GeV/c. For all b-jet tagging algorithms, the data and simulation are found to be in agreement to within about $\pm 20\%$. Similar results are found for a sample of events selected by requiring jet triggers with a p_T threshold of 300 GeV/c, in which the average p_T is 213 GeV/c. Depending on the prescales applied, the data correspond to an integrated luminosity of up to 5.0 fb^{-1} .

The misidentification probability is evaluated as:

$$\epsilon_{\text{data}}^{\text{misid}} = \epsilon_{\text{data}}^- \cdot R_{\text{light}}, \quad (8.1)$$

where ϵ_{data}^- is the negative tag rate as measured in jet data, defined as the fraction of jets that are negatively tagged. $R_{\text{light}} = \epsilon_{\text{MC}}^{\text{misid}} / \epsilon_{\text{MC}}^-$, a correction factor taken from simulation, is the ratio of the misidentification probability for light-parton jets to the negative tag rate for jets of all flavours in the simulation.

The rate ϵ_{data}^- depends on the numbers of c and b quarks in the negative-tagged jets (which tend to decrease R_{light}), on the residual differences between light-flavour quark and gluon jets, the number of tracks from other displaced processes (such as K_S^0 and Λ decays, and interactions in the detector material), and mismeasured tracks (which tend to increase R_{light}). Due to these contributions the simulation predicts ranges of R_{light} , for the different algorithms and jet p_T values, of about 1.1 to 1.4, 1 to 2, and 1 to 4, for the loose, medium, and tight operating points, respectively.

To compare the measured misidentification probability to that predicted by the simulation, a scale factor SF_{light} is defined:

$$SF_{\text{light}} = \epsilon_{\text{data}}^{\text{misid}} / \epsilon_{\text{MC}}^{\text{misid}}. \quad (8.2)$$

The following systematic effects on the misidentification probability based on negative tags are considered:

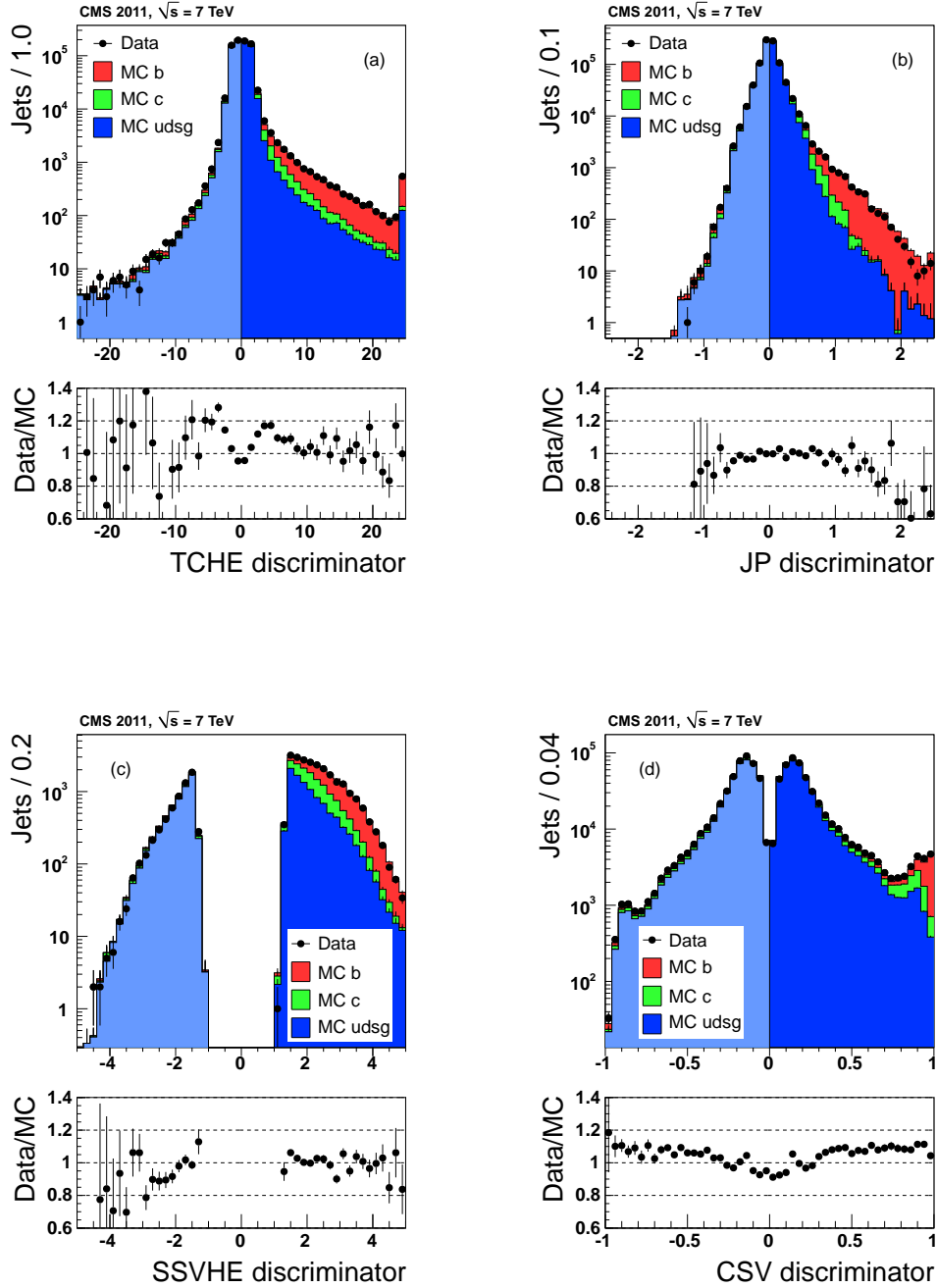


Figure 21. Signed b-jet tagging discriminators in data (dots) and simulation for light-parton jets (blue histogram, with a lighter colour for the negative discriminators), c jets (green histogram), and b jets (red histogram) for the (a) TCHE, (b) JP, (c) SSVHE, and (d) CSV algorithms. A jet-trigger p_T threshold of 30 GeV/c is required for both data and simulation. The simulation is normalized to the number of entries in the data. Underflow and overflow entries are added to the first and last bins, respectively.

- **b and c fractions:** the fraction of b-flavour jets has been measured in CMS to agree with the simulation within a $\pm 20\%$ uncertainty [44]. A $\pm 20\%$ uncertainty is conservatively estimated for the overall fraction of b and c jets. The b- and c-flavour fraction is varied in the QCD multijet simulation, from which a systematic uncertainty on R_{light} is inferred.
- **Gluon fraction:** this affects both the misidentification probability in simulation and the overall negative tag rates. The average fraction of gluon jets depends on the details of the parton density and hadronization functions used in the simulation. An uncertainty of $\pm 20\%$ is extracted from the comparison of simulation with data [45].
- **Long-lived K_S^0 and Λ decays:** the amount of reconstructed K_S^0 and Λ are found to be larger in the data than in the simulation [46]. To estimate the uncertainty on R_{light} due to the K_S^0 and Λ contribution, the simulated jets are reweighted by factors of 1.3 ± 0.3 and 1.5 ± 0.5 , respectively, in order to match the observed yield of K_S^0 and Λ in the data. The quoted uncertainties on the factors account for the p_T dependence. The yield is varied accordingly and the inferred variation on R_{light} is taken as a systematic uncertainty.
- **Photon conversion and nuclear interactions:** the rate of secondary interactions in the pixel detector layers has been measured with $\pm 5\%$ precision [28, 47]. The corresponding variation implies a systematic uncertainty on R_{light} .
- **Mismeasured tracks:** according to the simulation, jets with a reconstructed track not associated with a genuine charged particle also present an excess of positive over negative tags. To correct for residual mismeasurement effects, a $\pm 50\%$ variation on this contribution is taken into account in the systematic uncertainty on R_{light} .
- **Sign flip:** small differences in the angle between a track and the jet axis can lead to a change of the sign of the impact parameter (“sign flip”) and modify the negative tag rate. In order to quantify this effect the ratio of the number of negative to positive tagged jets is computed in a muon jet sample similar to the one described in section 5, with a larger than 80% b purity. Data and simulation are found to be in good agreement. From the statistical uncertainty on the comparison, the absolute uncertainty on this ratio is estimated as 2%, 1%, and 0.5% for loose, medium, and tight operating points, respectively. This sign flip uncertainty can be translated into a systematic uncertainty on R_{light} .
- **Pileup:** the misidentification probability depends on the pileup model used in the simulation. The simulated events are reweighted in order to match the pileup rate in the data. Differences between R_{light} values obtained for different running periods are used to estimate the systematic uncertainty, which is about $\pm 1\%$ for all taggers.
- **Event sample:** physics analyses use jets from different event topologies. For a given jet p_T , the misidentification probability is different for the leading jet or if there are other jets with higher p_T values in the same event. Measured misidentification scale factors for leading and subleading jets have a dispersion of about 7%. In addition, misidentification scale factors vary by 2–7%, depending on the tagger, for different running periods. These two uncertainties are added in quadrature to account for an uncertainty due to sample dependence. This is the dominant contribution to the overall systematic uncertainty on the misidentification probability.

Table 11. Relative systematic uncertainties on SF_{light} for jet p_T in the range 80–120 GeV/c. The columns correspond to the different sources of systematics in the order described in the text.

| b tagger | b and c jets | gluon | V^0 and 2^{nd} int. | mismeas. | sign flip | MC stat | pileup and evt. sample | total |
|----------|-----------------|-------|-----------------------------------|----------|-----------|---------|---------------------------|-------|
| JPM | 8.6% | 0.8% | 7.9% | 1.0% | 6.4% | 0.9% | 9.4% | 16.5% |
| JBPM | 6.2% | 1.2% | 6.9% | 0.5% | 1.6% | 0.9% | 9.0% | 13.2% |
| TCHEM | 4.5% | 0.8% | 6.2% | 1.2% | 5.1% | 0.7% | 8.0% | 12.4% |
| TCHPM | 1.6% | 1.0% | 3.0% | 0.6% | 2.5% | 0.6% | 9.2% | 10.3% |
| SSVHEM | 1.0% | 0.9% | 3.2% | 1.9% | 2.9% | 0.7% | 7.3% | 9.0% |
| CSVM | 3.2% | 1.8% | 4.4% | 0.7% | 4.6% | 0.7% | 7.4% | 10.6% |

Table 12. Misidentification probabilities and the corresponding data/MC scale factors SF_{light} for different algorithms and operating points for jet p_T in the range 80–120 GeV/c. The statistical uncertainties are quoted for the misidentification probabilities, while both the statistical and the systematic uncertainties are given for the scale factors.

| b tagger | misidentification probability | SF_{light} |
|----------|-------------------------------|--------------------------|
| JPL | 0.1000 ± 0.0004 | $0.99 \pm 0.01 \pm 0.10$ |
| JBPL | 0.1019 ± 0.0004 | $0.96 \pm 0.01 \pm 0.09$ |
| TCHEL | 0.1989 ± 0.0005 | $1.10 \pm 0.01 \pm 0.09$ |
| CSVL | 0.1020 ± 0.0004 | $1.10 \pm 0.01 \pm 0.09$ |
| JPM | 0.0107 ± 0.0001 | $1.03 \pm 0.01 \pm 0.17$ |
| JBPM | 0.0110 ± 0.0001 | $0.95 \pm 0.01 \pm 0.13$ |
| TCHEM | 0.0282 ± 0.0003 | $1.21 \pm 0.01 \pm 0.15$ |
| TCHPM | 0.0304 ± 0.0003 | $1.24 \pm 0.01 \pm 0.13$ |
| SSVHEM | 0.0208 ± 0.0002 | $0.94 \pm 0.01 \pm 0.08$ |
| CSVM | 0.0151 ± 0.0002 | $1.11 \pm 0.01 \pm 0.12$ |
| JPT | 0.00116 ± 0.00005 | $1.03 \pm 0.04 \pm 0.25$ |
| JBPT | 0.00117 ± 0.00004 | $0.95 \pm 0.04 \pm 0.19$ |
| TCHPT | 0.00284 ± 0.00009 | $1.26 \pm 0.04 \pm 0.21$ |
| SSVHPT | 0.00207 ± 0.00009 | $1.02 \pm 0.04 \pm 0.17$ |
| CSVT | 0.00120 ± 0.00005 | $1.17 \pm 0.05 \pm 0.21$ |

The systematic uncertainties are detailed in table 11 for the various algorithms and for the example of the medium operating points in the jet p_T range between 80 and 120 GeV/c.

The measured misidentification probabilities and data/MC scale factors are presented in figures 22 and 23 as a function of the jet p_T for the JPL and CSVM taggers. For a jet p_T of about 80 GeV/c the misidentification probabilities are close to 10% and 1% for the loose (JPL) and medium (CSVM) selections, respectively. Both algorithms show an increase of the misidentification probability with jet p_T that can be explained by the higher track densities in collimated jets. The simulation reproduces this dependence to a large extent. The observed scale factors are close to one with a decrease of $\sim 10\%$ toward the highest jet p_T . The misidentification probabilities measured with data and the data/MC scale factors are given in table 12 for jets with p_T between

80 and 120 GeV/c. The scale factors for the misidentification probability have also been measured as a function of the jet p_T for jets in several pseudorapidity intervals: $|\eta| < 0.5$, $0.5 \leq |\eta| < 1.0$, $1.0 \leq |\eta| < 1.5$ and $1.5 \leq |\eta| < 2.4$ for the loose operating points and $|\eta| < 0.8$, $0.8 \leq |\eta| < 1.6$ and $1.6 \leq |\eta| < 2.4$ for the medium operating points. For each b-tagging algorithm, the scale factors are compatible within about 10%. These pseudorapidity-dependent scale factors for the misidentification probabilities are used in physics analyses.

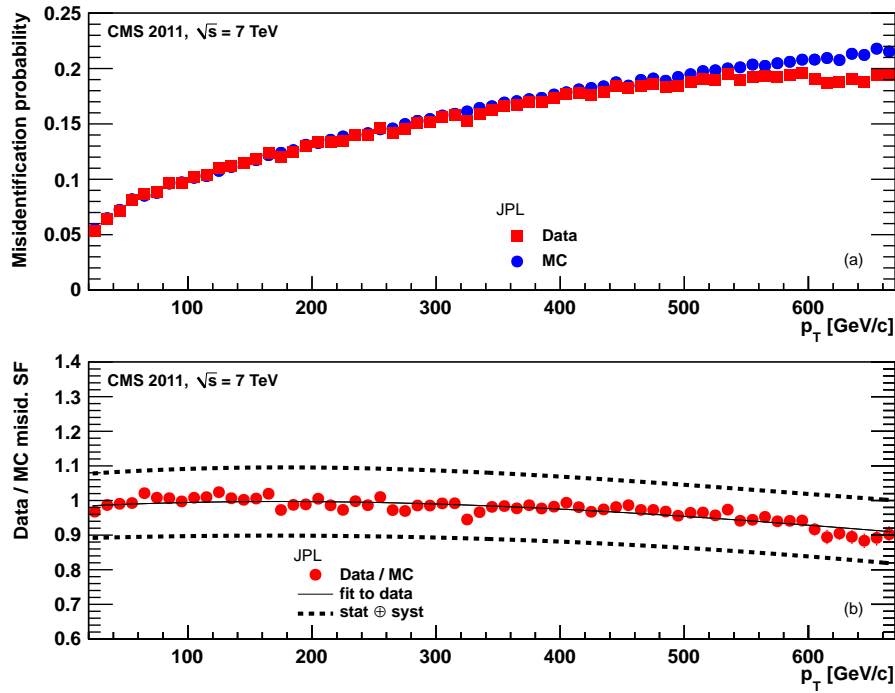


Figure 22. For the JPL tagger: (a) misidentification probability in data (red squares) and simulation (blue dots); (b) scale factor for the misidentification probability. The last p_T bin in each plot includes all jets with $p_T > 670$ GeV/c. The solid curve is the result of a polynomial fit to the data points. The dashed curves represent the overall statistical and systematic uncertainties on the measurements.

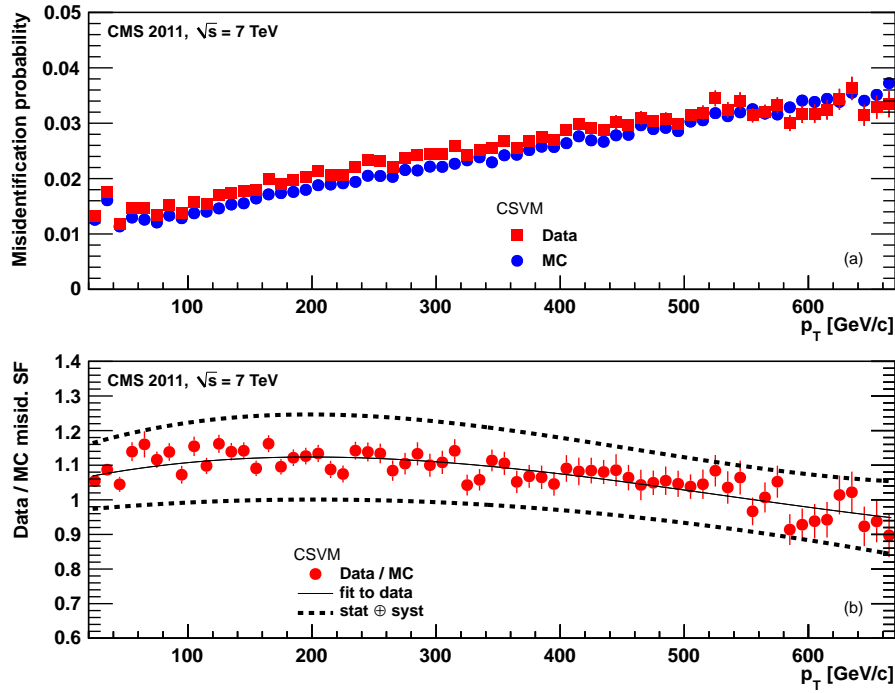


Figure 23. Same as figure 22 but for the CSVM tagger.

9 Conclusions

The CMS collaboration has developed a variety of algorithms that are used to identify jets that arise from the hadronization of bottom quarks. Early analyses relied on simple and robust techniques, based on the second or third highest impact parameter significance of the tracks associated to a jet, or the flight distance measured using a reconstructed secondary vertex. More recent analyses use algorithms with better performance that define a powerful discriminant from the combination of several variables. The use of these more advanced algorithms is made possible by the high degree of agreement achieved between data and simulation, and by the robustness of the algorithms against variations in the running conditions.

The algorithms provide selections at several operating points. The efficiencies of the algorithms at these operating points have been measured with a number of methods using multijet and $t\bar{t}$ events. A differential measurement of the efficiency as a function of jet p_T , from 30 to 670 GeV/c, has been carried out with the multijet sample. This information is used in analyses that require knowledge of the performance of b-jet tagging over a wide range of transverse momenta. The information is also helpful for analyses such as the measurement of the $t\bar{t}$ cross section in order to avoid the strong correlations that can occur if the efficiencies are inferred from the $t\bar{t}$ event sample itself.

The $t\bar{t}$ sample provides inclusive results, which are suitable for measurements of top-quark properties and for the analysis of standard model processes with similar jet momentum spectra and multiplicities. The misidentification probability, that a light-parton jet is mistaken as a b-quark jet, has been measured by applying inverted tagging algorithms to the multijet events.

The most effective algorithm is the Combined Secondary Vertex tagger. Using a loose selection, CMS achieves b-jet tagging efficiencies of about 85%, for a light-parton misidentification probability of 10%. This selection is suited for $t\bar{t}$ analyses. In analyses requiring higher b-jet purity, such as searches for supersymmetric particles, approximately 70% b-jet tagging efficiency is achieved, for a light-parton misidentification probability of only 1.5%. These values apply for jet transverse momenta typically observed in $t\bar{t}$ events.

The measured b-jet tagging performance is quantified and implemented in CMS analyses by using scale factor corrections to the MC simulation. These scale factors have been used extensively to enable studies over a wide range of event topologies that would otherwise not be possible due to limited statistics. The scale factors for the b-jet tagging efficiencies are measured with uncertainties of 2–4%, and 3–8%, in the jet p_T range 30–320 GeV/ c and 320–670 GeV/ c respectively. The maximum deviation of these scale factors from unity is approximately 10%. The scale factors for light-parton jet misidentification probabilities are measured to a precision of 8–17% over the full p_T range, and differ from unity by at most 25%. The scale factors for c-jet tagging efficiency are assumed to be the same as for b jets, with the corresponding uncertainty conservatively doubled.

The b-jet identification techniques discussed in this paper have been used in more than 40 analyses published by CMS, including measurements of top-quark properties, the Higgs boson, and searches for signals of physics beyond the standard model. The reduction of the uncertainties on the b-jet tagging scale factors has enabled the CMS experiment to decrease the light-parton background to unprecedented levels while maintaining high b-jet tagging efficiency for a wide range of processes containing heavy-flavour jets.

Acknowledgments

We congratulate our colleagues in the CERN accelerator departments for the excellent performance of the LHC machine. We thank the technical and administrative staff at CERN and other CMS institutes. This work was supported by the Austrian Federal Ministry of Science and Research; the Belgium Fonds de la Recherche Scientifique, and Fonds voor Wetenschappelijk Onderzoek; the Brazilian Funding Agencies (CNPq, CAPES, FAPERJ, and FAPESP); the Bulgarian Ministry of Education and Science; CERN; the Chinese Academy of Sciences, Ministry of Science and Technology, and National Natural Science Foundation of China; the Colombian Funding Agency (COLCIENCIAS); the Croatian Ministry of Science, Education and Sport; the Research Promotion Foundation, Cyprus; the Ministry of Education and Research, Recurrent financing contract SF0690030s09 and European Regional Development Fund, Estonia; the Academy of Finland, Finnish Ministry of Education and Culture, and Helsinki Institute of Physics; the Institut National de Physique Nucléaire et de Physique des Particules / CNRS, and Commissariat à l'Énergie Atomique et aux Énergies Alternatives / CEA, France; the Bundesministerium für Bildung und Forschung, Deutsche Forschungsgemeinschaft, and Helmholtz-Gemeinschaft Deutscher Forschungszentren, Germany; the General Secretariat for Research and Technology, Greece; the National Scientific Research Foundation, and National Office for Research and Technology, Hungary; the Department of Atomic Energy and the Department of Science and Technology, India; the Institute for Studies in Theoretical Physics and Mathematics, Iran; the Science Foundation, Ireland; the Istituto Nazionale di Fisica Nucleare, Italy; the Korean Ministry of Education, Science and

Technology and the World Class University program of NRF, Korea; the Lithuanian Academy of Sciences; the Mexican Funding Agencies (CINVESTAV, CONACYT, SEP, and UASLP-FAI); the Ministry of Science and Innovation, New Zealand; the Pakistan Atomic Energy Commission; the Ministry of Science and Higher Education and the National Science Centre, Poland; the Fundação para a Ciência e a Tecnologia, Portugal; JINR (Armenia, Belarus, Georgia, Ukraine, Uzbekistan); the Ministry of Education and Science of the Russian Federation, the Federal Agency of Atomic Energy of the Russian Federation, Russian Academy of Sciences, and the Russian Foundation for Basic Research; the Ministry of Science and Technological Development of Serbia; the Secretaría de Estado de Investigación, Desarrollo e Innovación and Programa Consolider-Ingenio 2010, Spain; the Swiss Funding Agencies (ETH Board, ETH Zurich, PSI, SNF, UniZH, Canton Zurich, and SER); the National Science Council, Taipei; the Scientific and Technical Research Council of Turkey, and Turkish Atomic Energy Authority; the Science and Technology Facilities Council, UK; the US Department of Energy, and the US National Science Foundation.

Individuals have received support from the Marie-Curie programme and the European Research Council (European Union); the Leventis Foundation; the A. P. Sloan Foundation; the Alexander von Humboldt Foundation; the Austrian Science Fund (FWF); the Belgian Federal Science Policy Office; the Fonds pour la Formation à la Recherche dans l'Industrie et dans l'Agriculture (FRIA-Belgium); the Agentschap voor Innovatie door Wetenschap en Technologie (IWT-Belgium); the Council of Science and Industrial Research, India; the Compagnia di San Paolo (Torino); and the HOMING PLUS programme of Foundation for Polish Science, cofinanced from European Union, Regional Development Fund.

References

- [1] CMS collaboration, *Measurement of the $t\bar{t}$ production cross section in pp collisions at 7 TeV in lepton + jets events using b quark jet identification*, *Phys. Rev. D* **84** (2011) 092004 [[arXiv:1108.3773](#)].
- [2] CMS collaboration, *Search for supersymmetry in events with b Jets and missing transverse momentum at the LHC*, *JHEP* **07** (2011) 113 [[arXiv:1106.3272](#)].
- [3] CMS collaboration, *Measurement of the t -channel single top quark production cross section in pp collisions at $\sqrt{s} = 7$ TeV*, *Phys. Rev. Lett.* **107** (2011) 091802 [[arXiv:1106.3052](#)].
- [4] CMS collaboration, *The CMS experiment at the CERN LHC*, *2008 JINST* **3** S08004.
- [5] T. Sjöstrand, S. Mrenna and P.Z. Skands, *PYTHIA 6.4 physics and manual*, *JHEP* **05** (2006) 026 [[hep-ph/0603175](#)].
- [6] R. Field, *Early LHC Underlying Event Data - Findings and Surprises*, [arXiv:1010.3558](#).
- [7] J. Alwall, M. Herquet, F. Maltoni, O. Mattelaer and T. Stelzer, *MadGraph 5: going beyond*, *JHEP* **06** (2011) 128 [[arXiv:1106.0522](#)].
- [8] M.L. Mangano, M. Moretti, F. Piccinini and M. Treccani, *Matching matrix elements and shower evolution for top-quark production in hadronic collisions*, *JHEP* **01** (2007) 013 [[hep-ph/0611129](#)].
- [9] N. Davidson, G. Nanava, T. Przedziński, E. Richter-Wąs and Z. Wąs, *Universal Interface of TAUOLA Technical and Physics Documentation*, *Comput. Phys. Commun.* **183** (2012) 821 [[arXiv:1002.0543](#)].

- [10] S. Frixione, P. Nason and C. Oleari, *Matching NLO QCD computations with parton shower simulations: the POWHEG method*, *JHEP* **11** (2007) 070 [[arXiv:0709.2092](#)].
- [11] J.M. Campbell and R.K. Ellis, *MC_{FM} for the Tevatron and the LHC*, *Nucl. Phys. Proc. Suppl.* **205-206** (2010) 10 [[arXiv:1007.3492](#)].
- [12] A.D. Martin, W. Stirling, R. Thorne and G. Watt, *Uncertainties on α_s in global parton distribution functions analyses and implications for predicted hadronic cross sections*, *Eur. Phys. J. C* **64** (2009) 653 [[arXiv:0905.3531](#)].
- [13] H.-L. Lai, J. Huston, Z. Li, P. Nadolsky, J. Pumplin, et al., *Uncertainty induced by QCD coupling in the CTEQ global analysis of parton distributions*, *Phys. Rev. D* **82** (2010) 054021 [[arXiv:1004.4624](#)].
- [14] F. Demartin, S. Forte, E. Mariani, J. Rojo and A. Vicini, *The impact of PDF and α_s uncertainties on Higgs Production in gluon fusion at hadron colliders*, *Phys. Rev. D* **82** (2010) 014002 [[arXiv:1004.0962](#)].
- [15] M. Botje et al., *The PDF4LHC Working Group Interim Recommendations*, [arXiv:1101.0538](#).
- [16] J.M. Campbell, R. Frederix, F. Maltoni and F. Tramontano, *Next-to-Leading-Order Predictions for t -Channel Single-Top Production at Hadron Colliders*, *Phys. Rev. Lett.* **102** (2009) 182003 [[arXiv:0903.0005](#)].
- [17] J.M. Campbell and F. Tramontano, *Next-to-leading order corrections to Wt production and decay*, *Nucl. Phys. B* **726** (2005) 109 [[hep-ph/0506289](#)].
- [18] J.M. Campbell, R.K. Ellis and F. Tramontano, *Single top production and decay at next-to-leading order*, *Phys. Rev. D* **70** (2004) 094012 [[hep-ph/0408158](#)].
- [19] N. Kidonakis, *Two-loop soft anomalous dimensions for single top quark associated production with a W^- or H^-* , *Phys. Rev. D* **82** (2010) 054018 [[arXiv:1005.4451](#)].
- [20] N. Kidonakis, *Next-to-next-to-leading logarithm resummation for s -channel single top quark production*, *Phys. Rev. D* **81** (2010) 054028 [[arXiv:1001.5034](#)].
- [21] K. Melnikov and F. Petriello, *Electroweak gauge boson production at hadron colliders through $O(\alpha_s^2)$* , *Phys. Rev. D* **74** (2006) 114017 [[hep-ph/0609070](#)].
- [22] PARTICLE DATA GROUP, J. Beringer et al., *Review of Particle Physics (RPP)*, *Phys. Rev. D* **86** (2012) 010001.
- [23] GEANT4 collaboration, S. Agostinelli et al., *GEANT4 — a simulation toolkit*, *Nucl. Instrum. Meth. A* **506** (2003) 250.
- [24] CMS collaboration, *Particle-Flow Event Reconstruction in CMS and Performance for Jets, Taus and MET*, CMS Physics Analysis Summary [CMS-PAS-PFT-09-001](#).
- [25] CMS collaboration, *Commissioning of the Particle-Flow reconstruction in Minimum-Bias and Jet Events from pp Collisions at 7 TeV*, CMS Physics Analysis Summary [CMS-PAS-PFT-10-002](#).
- [26] M. Cacciari, G.P. Salam and G. Soyez, *The Anti- k_t jet clustering algorithm*, *JHEP* **04** (2008) 063 [[arXiv:0802.1189](#)].
- [27] CMS collaboration, *Determination of jet energy calibration and transverse momentum resolution in CMS*, *2011 JINST* **6** P11002 [[arXiv:1107.4277](#)].
- [28] CMS collaboration, *CMS Tracking performance results from early LHC Operation*, *Eur. Phys. J. C* **70** (2010) 1165 [[arXiv:1007.1988](#)].

- [29] CMS collaboration, *Performance of CMS muon reconstruction in pp collision events at $\sqrt{s} = 7$ TeV*, [2012 JINST 7 P10002](#) [[arXiv:1206.4071](#)].
- [30] R. Frühwirth, W. Waltenberger and P. Vanlaer, *Adaptive vertex fitting*, [J. Phys. G 34 \(2007\) N343](#).
- [31] ALEPH collaboration, D. Buskulic et al., *A precise measurement of $\Gamma_{Z \rightarrow b\bar{b}} / \Gamma_{Z \rightarrow \text{hadrons}}$* , [Phys. Lett. B 313 \(1993\) 535](#).
- [32] G. Borisov and C. Mariotti, *Fine tuning of track impact parameter resolution of the DELPHI detector*, [Nucl. Instrum. Meth. A 372 \(1996\) 181](#).
- [33] V. Blobel, *Software alignment for tracking detectors*, [Nucl. Instrum. Meth. A 566 \(2006\) 5](#).
- [34] G. Flucke, P. Schleper, G. Steinbrück and M. Stoye, *CMS silicon tracker alignment strategy with the Millepede II algorithm*, [2008 JINST 3 P09002](#).
- [35] UA1 collaboration, C. Albajar et al., *Study of heavy flavor production in events with a muon accompanied by jet(s) at the CERN proton-antiproton collider*, [Z. Phys. C 37 \(1988\) 489](#).
- [36] B. Clément, *Electroweak production of the top quark in the Run II of the D0 experiment*, Ph.D. thesis, IPHC, Université de Strasbourg, France, 2006, <http://scd-theses.u-strasbg.fr/1103/>.
- [37] D0 collaboration, V. Abazov et al., *b-Jet Identification in the D0 Experiment*, [Nucl. Instrum. Meth. A 620 \(2010\) 490](#) [[arXiv:1002.4224](#)].
- [38] CMS collaboration, *Measurement of $B\bar{B}$ angular correlations based on secondary vertex reconstruction at $\sqrt{s} = 7$ TeV*, [JHEP 03 \(2011\) 136](#) [[arXiv:1102.3194](#)].
- [39] CMS collaboration, *Measurement of the $t\bar{t}$ production cross section in the dilepton channel in pp collisions at $\sqrt{s} = 7$ TeV*, [JHEP 11 \(2012\) 067](#) [[arXiv:1208.2671](#)].
- [40] R. Field, *Studying the underlying event at CDF and the LHC*, proceedings of the *First International Workshop, Multiple Partonic Interactions at the LHC (MPI'08)*, Perugia, Italy, October 27-31, 2008 [[arXiv:1003.4220](#) 12].
- [41] F. James, *Statistical Methods in Experimental Physics*, World Scientific, 2nd edition, 2006.
- [42] S.S. Wilks, *The Large-Sample Distribution of the Likelihood Ratio for Testing Composite Hypotheses*, [Ann. Math. Statist. 9 \(1938\) 60](#).
- [43] L. Lyons, D. Gibaut and P. Clifford, *How to combine correlated estimates of a single physical quantity*, [Nucl. Instrum. Meth. A 270 \(1988\) 110](#).
- [44] CMS collaboration, *Inclusive b-jet production in pp collisions at $\sqrt{s} = 7$ TeV*, [JHEP 04 \(2012\) 084](#) [[arXiv:1202.4617](#)].
- [45] CMS collaboration, *Measurement of the Inclusive Jet Cross Section in pp Collisions at $\sqrt{s} = 7$ TeV*, [Phys. Rev. Lett. 107 \(2011\) 132001](#) [[arXiv:1106.0208](#)].
- [46] CMS collaboration, *Strange particle production in pp collisions at $\sqrt{s} = 0.9$ and 7 TeV*, [JHEP 05 \(2011\) 064](#) [[arXiv:1102.4282](#)].
- [47] CMS collaboration, *Studies of Tracker Material*, CMS Physics Analysis Summary [CMS-PAS-TRK-10-003](#).

Glossary

- bSample** Method to measure the b-jet tagging efficiency in $t\bar{t}$ events from a b-enriched sample
- CSVL** Combined Secondary Vertex algorithm at the loose operating point
- CSVM** Combined Secondary Vertex algorithm at the medium operating point
- CSVT** Combined Secondary Vertex algorithm at the tight operating point
- FTC** Flavour Tag Consistency method for the measurement of the b-jet tagging efficiency in $t\bar{t}$ events
- FTM** Flavour Tag Matching method for the measurement of the b-jet tagging efficiency in $t\bar{t}$ events
- IP3D (method)** Method for the measurement of the b-jet tagging efficiency in multijet events based on the impact parameters of muons
- IP** Impact parameter of a track
- JBPL** Jet B Probability algorithm at the loose operating point
- JBPM** Jet B Probability algorithm at the medium operating point
- JBPT** Jet B Probability algorithm at the tight operating point
- JPL** Jet Probability algorithm at the loose operating point
- JPM** Jet Probability algorithm at the medium operating point
- JPT** Jet Probability algorithm at the tight operating point
- LT (method)** Lifetime Tagging method for the measurement of the b-jet tagging efficiency in multijet events
- PLR** Profile Likelihood Ratio method for the measurement of the b-jet tagging efficiency in $t\bar{t}$ events
- PtRel (method)** Method for the measurement of the b-jet tagging efficiency in multijet events based on the transverse momenta of muons w.r.t. the jet axis
- PV** Primary Vertex (proton-proton interaction point)
- SIP** Significance of the impact parameter of a track
- SSVHEM** Simple Secondary Vertex High Efficiency algorithm at the medium operating point
- SSVHPT** Simple Secondary Vertex High Purity algorithm at the tight operating point
- SV** Secondary Vertex (decay vertex of a long-lived particle)
- TC** Track Counting (TCHE and TCHP) algorithms
- TCHEL** Track Counting High Efficiency algorithm at the loose operating point
- TCHEM** Track Counting High Efficiency algorithm at the medium operating point
- TCHPM** Track Counting High Purity algorithm at the medium operating point
- TCHPT** Track Counting High Purity algorithm at the tight operating point

The CMS collaboration

Yerevan Physics Institute, Yerevan, Armenia

S. Chatrchyan, V. Khachatryan, A.M. Sirunyan, A. Tumasyan

Institut für Hochenergiephysik der OeAW, Wien, Austria

W. Adam, E. Aguilo, T. Bergauer, M. Dragicevic, J. Erö, C. Fabjan¹, M. Friedl, R. Frühwirth¹, V.M. Ghete, J. Hammer, N. Hörmann, J. Hrubec, M. Jeitler¹, W. Kiesenhofer, V. Knünz, M. Krammer¹, I. Krätschmer, D. Liko, I. Mikulec, M. Pernicka[†], B. Rahbaran, C. Rohringer, H. Rohringer, R. Schöfbeck, J. Strauss, A. Taurok, W. Waltenberger, G. Walzel, E. Widl, C.-E. Wulz¹

National Centre for Particle and High Energy Physics, Minsk, Belarus

V. Mossolov, N. Shumeiko, J. Suarez Gonzalez

Universiteit Antwerpen, Antwerpen, Belgium

M. Bansal, S. Bansal, T. Cornelis, E.A. De Wolf, X. Janssen, S. Luyckx, L. Mucibello, S. Ochesanu, B. Roland, R. Rougny, M. Selvaggi, Z. Staykova, H. Van Haevermaet, P. Van Mechelen, N. Van Remortel, A. Van Spilbeeck

Vrije Universiteit Brussel, Brussel, Belgium

F. Blekman, S. Blyweert, J. D'Hondt, R. Gonzalez Suarez, A. Kalogeropoulos, M. Maes, A. Olbrechts, W. Van Doninck, P. Van Mulders, G.P. Van Onsem, I. Villella

Université Libre de Bruxelles, Bruxelles, Belgium

B. Clerbaux, G. De Lentdecker, V. Dero, A.P.R. Gay, T. Hreus, A. Léonard, P.E. Marage, A. Mohammadi, T. Reis, L. Thomas, G. Vander Marcken, C. Vander Velde, P. Vanlaer, J. Wang

Ghent University, Ghent, Belgium

V. Adler, K. Beernaert, A. Cimmino, S. Costantini, G. Garcia, M. Grunewald, B. Klein, J. Lellouch, A. Marinov, J. McCartin, A.A. Ocampo Rios, D. Ryckbosch, N. Strobbe, F. Thyssen, M. Tytgat, P. Verwilligen, S. Walsh, E. Yazgan, N. Zaganidis

Université Catholique de Louvain, Louvain-la-Neuve, Belgium

S. Basegmez, G. Bruno, R. Castello, L. Ceard, C. Delaere, T. du Pree, D. Favart, L. Forthomme, A. Giammanco², J. Hollar, V. Lemaître, J. Liao, O. Militaru, C. Nuttens, D. Pagano, A. Pin, K. Piotrkowski, N. Schul, J.M. Vizan Garcia

Université de Mons, Mons, Belgium

N. Bely, T. Caebergs, E. Daubie, G.H. Hammad

Centro Brasileiro de Pesquisas Fisicas, Rio de Janeiro, Brazil

G.A. Alves, M. Correa Martins Junior, D. De Jesus Damiao, T. Martins, M.E. Pol, M.H.G. Souza

Universidade do Estado do Rio de Janeiro, Rio de Janeiro, Brazil

W.L. Aldá Júnior, W. Carvalho, A. Custódio, E.M. Da Costa, C. De Oliveira Martins, S. Fonseca De Souza, D. Matos Figueiredo, L. Mundim, H. Nogima, V. Oguri, W.L. Prado Da Silva, A. Santoro, L. Soares Jorge, A. Sznajder

Instituto de Fisica Teorica^a, Universidade Estadual Paulista^b, Sao Paulo, Brazil

T.S. Anjos^{b,3}, C.A. Bernardes^{b,3}, F.A. Dias^{a,4}, T.R. Fernandez Perez Tomei^a, E.M. Gregores^{b,3}, C. Lagana^a, F. Marinho^a, P.G. Mercadante^{b,3}, S.F. Novaes^a, Sandra S. Padula^a

Institute for Nuclear Research and Nuclear Energy, Sofia, Bulgaria

V. Genchev⁵, P. Iaydjiev⁵, S. Piperov, M. Rodozov, S. Stoykova, G. Sultanov, V. Tcholakov, R. Trayanov, M. Vutova

University of Sofia, Sofia, Bulgaria

A. Dimitrov, R. Hadjiiska, V. Kozhuharov, L. Litov, B. Pavlov, P. Petkov

Institute of High Energy Physics, Beijing, China

J.G. Bian, G.M. Chen, H.S. Chen, C.H. Jiang, D. Liang, S. Liang, X. Meng, J. Tao, J. Wang, X. Wang, Z. Wang, H. Xiao, M. Xu, J. Zang, Z. Zhang

State Key Lab. of Nucl. Phys. and Tech., Peking University, Beijing, China

C. Asawatangtrakuldee, Y. Ban, S. Guo, Y. Guo, W. Li, S. Liu, Y. Mao, S.J. Qian, H. Teng, D. Wang, L. Zhang, B. Zhu, W. Zou

Universidad de Los Andes, Bogota, Colombia

C. Avila, J.P. Gomez, B. Gomez Moreno, A.F. Osorio Oliveros, J.C. Sanabria

Technical University of Split, Split, Croatia

N. Godinovic, D. Lelas, R. Plestina⁶, D. Polic, I. Puljak⁵

University of Split, Split, Croatia

Z. Antunovic, M. Kovac

Institute Rudjer Boskovic, Zagreb, Croatia

V. Brigljevic, S. Duric, K. Kadija, J. Luetic, S. Morovic

University of Cyprus, Nicosia, Cyprus

A. Attikis, M. Galanti, G. Mavromanolakis, J. Mousa, C. Nicolaou, F. Ptochos, P.A. Razis

Charles University, Prague, Czech Republic

M. Finger, M. Finger Jr.

Academy of Scientific Research and Technology of the Arab Republic of Egypt, Egyptian Network of High Energy Physics, Cairo, Egypt

Y. Assran⁷, S. Elgammal⁸, A. Ellithi Kamel⁹, M.A. Mahmoud¹⁰, A. Radi^{11,12}

National Institute of Chemical Physics and Biophysics, Tallinn, Estonia

M. Kadastik, M. Müntel, M. Raidal, L. Rebane, A. Tiko

Department of Physics, University of Helsinki, Helsinki, Finland

P. Eerola, G. Fedi, M. Voutilainen

Helsinki Institute of Physics, Helsinki, Finland

J. Härkönen, A. Heikkinen, V. Karimäki, R. Kinnunen, M.J. Kortelainen, T. Lampén, K. Lassila-Perini, S. Lehti, T. Lindén, P. Luukka, T. Mäenpää, T. Peltola, E. Tuominen, J. Tuominiemi, E. Tuovinen, D. Ungaro, L. Wendland

Lappeenranta University of Technology, Lappeenranta, Finland

K. Banzuzi, A. Karjalainen, A. Korpela, T. Tuuva

DSM/IRFU, CEA/Saclay, Gif-sur-Yvette, France

M. Besancon, S. Choudhury, M. Dejardin, D. Denegri, B. Fabbro, J.L. Faure, F. Ferri, S. Ganjour, A. Givernaud, P. Gras, G. Hamel de Monchenault, P. Jarry, E. Locci, J. Malcles, L. Millischer, A. Nayak, J. Rander, A. Rosowsky, I. Shreyber, M. Titov

Laboratoire Leprince-Ringuet, Ecole Polytechnique, IN2P3-CNRS, Palaiseau, France

S. Baffioni, F. Beaudette, L. Benhabib, L. Bianchini, M. Bluj¹³, C. Broutin, P. Busson, C. Charlot, N. Daci, T. Dahms, L. Dobrzynski, R. Granier de Cassagnac, M. Haguenaue, P. Miné, C. Mironov, I.N. Naranjo, M. Nguyen, C. Ochando, P. Paganini, D. Sabes, R. Salerno, Y. Sirois, C. Veelken, A. Zabi

Institut Pluridisciplinaire Hubert Curien, Université de Strasbourg, Université de Haute Alsace Mulhouse, CNRS/IN2P3, Strasbourg, France

J.-L. Agram¹⁴, J. Andrea, D. Bloch, D. Bodin, J.-M. Brom, M. Cardaci, E.C. Chabert, C. Collard, E. Conte¹⁴, F. Drouhin¹⁴, C. Ferro, J.-C. Fontaine¹⁴, D. Gelé, U. Goerlach, P. Juillot, A.-C. Le Bihan, P. Van Hove

Centre de Calcul de l'Institut National de Physique Nucleaire et de Physique des Particules, CNRS/IN2P3, Villeurbanne, France, Villeurbanne, France

F. Fassi, D. Mercier

Université de Lyon, Université Claude Bernard Lyon 1, CNRS-IN2P3, Institut de Physique Nucléaire de Lyon, Villeurbanne, France

S. Beauceron, N. Beaupere, O. Bondu, G. Boudoul, J. Chasserat, R. Chierici⁵, D. Contardo, P. Depasse, H. El Mamouni, J. Fay, S. Gascon, M. Gouzevitch, B. Ille, T. Kurca, M. Lethuillier, L. Mirabito, S. Perries, V. Sordini, Y. Tschudi, P. Verdier, S. Viret

Institute of High Energy Physics and Informatization, Tbilisi State University, Tbilisi, Georgia

Z. Tsamalaidze¹⁵

RWTH Aachen University, I. Physikalisches Institut, Aachen, Germany

G. Anagnostou, S. Beranek, M. Edelhoff, L. Feld, N. Heracleous, O. Hindrichs, R. Jussen, K. Klein, J. Merz, A. Ostapchuk, A. Perieanu, F. Raupach, J. Sammet, S. Schael, D. Sprenger, H. Weber, B. Wittmer, V. Zhukov¹⁶

RWTH Aachen University, III. Physikalisches Institut A, Aachen, Germany

M. Ata, J. Caudron, E. Dietz-Laursonn, D. Duchardt, M. Erdmann, R. Fischer, A. Güth, T. Hebbeker, C. Heidemann, K. Hoepfner, D. Klingebiel, P. Kreuzer, C. Magass, M. Merschmeyer, A. Meyer, M. Olschewski, P. Papacz, H. Pieta, H. Reithler, S.A. Schmitz, L. Sonnenschein, J. Steggemann, D. Teyssier, M. Weber

RWTH Aachen University, III. Physikalisches Institut B, Aachen, Germany

M. Bontenackels, V. Cherepanov, Y. Erdogan, G. Flügge, H. Geenen, M. Geisler, W. Haj Ahmad, F. Hoehle, B. Kargoll, T. Kress, Y. Kuessel, A. Nowack, L. Perchalla, O. Pooth, P. Sauerland, A. Stahl

Deutsches Elektronen-Synchrotron, Hamburg, Germany

M. Aldaya Martin, J. Behr, W. Behrenhoff, U. Behrens, M. Bergholz¹⁷, A. Bethani, K. Borras, A. Burgmeier, A. Cakir, L. Calligaris, A. Campbell, E. Castro, F. Costanza, D. Dammann, C. Diez Pardos, G. Eckert, D. Eckstein, G. Flucke, A. Geiser, I. Glushkov, P. Gunnellini, S. Habib, J. Hauk, G. Hellwig, H. Jung, M. Kasemann, P. Katsas, C. Kleinwort, H. Kluge, A. Knutsson, M. Krämer, D. Krücker, E. Kuznetsova, W. Lange, W. Lohmann¹⁷, B. Lutz, R. Mankel, I. Marfin, M. Marienfeld, I.-A. Melzer-Pellmann, A.B. Meyer, J. Mnich, A. Mussgiller, S. Naumann-Emme, J. Olzem, H. Perrey, A. Petrukhin, D. Pitzl, A. Raspereza, P.M. Ribeiro Cipriano, C. Riedl, E. Ron, M. Rosin, J. Salfeld-Nebgen, R. Schmidt¹⁷, T. Schoerner-Sadenius, N. Sen, A. Spiridonov, M. Stein, R. Walsh, C. Wissing

University of Hamburg, Hamburg, Germany

C. Autermann, V. Blobel, J. Draeger, H. Enderle, J. Erfle, U. Gebbert, M. Görner, T. Hermanns, R.S. Höing, K. Kaschube, G. Kaussen, H. Kirschenmann, R. Klanner, J. Lange, B. Mura, F. Nowak, T. Peiffer, N. Pietsch,

D. Rathjens, C. Sander, H. Schettler, P. Schleper, E. Schlieckau, A. Schmidt, M. Schröder, T. Schum, M. Seidel, V. Sola, H. Stadie, G. Steinbrück, J. Thomsen, L. Vanelderden

Institut für Experimentelle Kernphysik, Karlsruhe, Germany

C. Barth, J. Berger, C. Böser, T. Chwalek, W. De Boer, A. Descroix, A. Dierlamm, M. Feindt, M. Guthoff⁵, C. Hackstein, F. Hartmann, T. Hauth⁵, M. Heinrich, H. Held, K.H. Hoffmann, S. Honc, I. Katkov¹⁶, J.R. Komaragiri, P. Lobelle Pardo, D. Martschei, S. Mueller, Th. Müller, M. Niegel, A. Nürnberg, O. Oberst, A. Oehler, J. Ott, G. Quast, K. Rabbertz, F. Ratnikov, N. Ratnikova, S. Röcker, A. Scheurer, F.-P. Schilling, G. Schott, H.J. Simonis, F.M. Stober, D. Troendle, R. Ulrich, J. Wagner-Kuhr, S. Wayand, T. Weiler, M. Zeise

Institute of Nuclear Physics "Demokritos", Aghia Paraskevi, Greece

G. Daskalakis, T. Gerasis, S. Kesisoglou, A. Kyriakis, D. Loukas, I. Manolagos, A. Markou, C. Markou, C. Mavrommatis, E. Ntomari

University of Athens, Athens, Greece

L. Gouskos, T.J. Mertzimekis, A. Panagiotou, N. Saoulidou

University of Ioánnina, Ioánnina, Greece

I. Evangelou, C. Foudas, P. Kokkas, N. Manthos, I. Papadopoulos, V. Patras

KFKI Research Institute for Particle and Nuclear Physics, Budapest, Hungary

G. Bencze, C. Hajdu, P. Hidas, D. Horvath¹⁸, F. Sikler, V. Veszpremi, G. Vesztergombi¹⁹

Institute of Nuclear Research ATOMKI, Debrecen, Hungary

N. Beni, S. Czellar, J. Molnar, J. Palinkas, Z. Szillasi

University of Debrecen, Debrecen, Hungary

J. Karacsi, P. Raics, Z.L. Trocsanyi, B. Ujvari

Panjab University, Chandigarh, India

S.B. Beri, V. Bhatnagar, N. Dhingra, R. Gupta, M. Kaur, M.Z. Mehta, N. Nishu, L.K. Saini, A. Sharma, J.B. Singh

University of Delhi, Delhi, India

Ashok Kumar, Arun Kumar, S. Ahuja, A. Bhardwaj, B.C. Choudhary, S. Malhotra, M. Naimuddin, K. Ranjan, V. Sharma, R.K. Shivpuri

Saha Institute of Nuclear Physics, Kolkata, India

S. Banerjee, S. Bhattacharya, S. Dutta, B. Gomber, Sa. Jain, Sh. Jain, R. Khurana, S. Sarkar, M. Sharan

Bhabha Atomic Research Centre, Mumbai, India

A. Abdulsalam, R.K. Choudhury, D. Dutta, S. Kailas, V. Kumar, P. Mehta, A.K. Mohanty⁵, L.M. Pant, P. Shukla

Tata Institute of Fundamental Research - EHEP, Mumbai, India

T. Aziz, S. Ganguly, M. Guchait²⁰, M. Maity²¹, G. Majumder, K. Mazumdar, G.B. Mohanty, B. Parida, K. Sudhakar, N. Wickramage

Tata Institute of Fundamental Research - HECR, Mumbai, India

S. Banerjee, S. Dugad

Institute for Research in Fundamental Sciences (IPM), Tehran, Iran

H. Arfaei, H. Bakhshiansohi²², S.M. Etesami²³, A. Fahim²², M. Hashemi, H. Hesari, A. Jafari²², M. Khakzad, M. Mohammadi Najafabadi, S. Paktinat Mehdiabadi, B. Safarzadeh²⁴, M. Zeinali²³

INFN Sezione di Bari ^a, Università di Bari ^b, Politecnico di Bari ^c, Bari, Italy

M. Abbrescia^{a,b}, L. Barbone^{a,b}, C. Calabria^{a,b,5}, S.S. Chhibra^{a,b}, A. Colaleo^a, D. Creanza^{a,c}, N. De Filippis^{a,c,5}, M. De Palma^{a,b}, L. Fiore^a, G. Iaselli^{a,c}, L. Lusito^{a,b}, G. Maggi^{a,c}, M. Maggi^a, B. Marangelli^{a,b}, S. My^{a,c}, S. Nuzzo^{a,b}, N. Pacifico^{a,b}, A. Pompili^{a,b}, G. Pugliese^{a,c}, G. Selvaggi^{a,b}, L. Silvestris^a, G. Singh^{a,b}, R. Venditti^{a,b}, G. Zito^a

INFN Sezione di Bologna ^a, Università di Bologna ^b, Bologna, Italy

G. Abbiendi^a, A.C. Benvenuti^a, D. Bonacorsi^{a,b}, S. Braibant-Giacomelli^{a,b}, L. Brigliadori^{a,b}, P. Capiluppi^{a,b}, A. Castro^{a,b}, F.R. Cavallo^a, M. Cuffiani^{a,b}, G.M. Dallavalle^a, F. Fabbri^a, A. Fanfani^{a,b}, D. Fasanella^{a,b,5}, P. Giacomelli^a, C. Grandi^a, L. Guiducci^{a,b}, S. Marcellini^a, G. Masetti^a, M. Meneghelli^{a,b,5}, A. Montanari^a, F.L. Navarria^{a,b}, F. Odorici^a, A. Perrotta^a, F. Primavera^{a,b}, A.M. Rossi^{a,b}, T. Rovelli^{a,b}, G.P. Siroli^{a,b}, R. Travaglini^{a,b}

INFN Sezione di Catania ^a, Università di Catania ^b, Catania, Italy

S. Albergo^{a,b}, G. Cappello^{a,b}, M. Chiorboli^{a,b}, S. Costa^{a,b}, R. Potenza^{a,b}, A. Tricomi^{a,b}, C. Tuve^{a,b}

INFN Sezione di Firenze ^a, Università di Firenze ^b, Firenze, Italy

G. Barbagli^a, V. Ciulli^{a,b}, C. Civinini^a, R. D'Alessandro^{a,b}, E. Focardi^{a,b}, S. Frosali^{a,b}, E. Gallo^a, S. Gonzi^{a,b}, M. Meschini^a, S. Paoletti^a, G. Sguazzoni^a, A. Tropiano^a

INFN Laboratori Nazionali di Frascati, Frascati, Italy

L. Benussi, S. Bianco, S. Colafranceschi²⁵, F. Fabbri, D. Piccolo

INFN Sezione di Genova ^a, Università di Genova ^b, Genova, Italy

P. Fabbriatore^a, R. Musenich^a, S. Tosi^{a,b}

INFN Sezione di Milano-Bicocca ^a, Università di Milano-Bicocca ^b, Milano, Italy

A. Benaglia^{a,b,5}, F. De Guio^{a,b}, L. Di Matteo^{a,b,5}, S. Fiorendi^{a,b}, S. Gennai^{a,5}, A. Ghezzi^{a,b}, S. Malvezzi^a, R.A. Manzoni^{a,b}, A. Martelli^{a,b}, A. Massironi^{a,b,5}, D. Menasce^a, L. Moroni^a, M. Paganoni^{a,b}, D. Pedrini^a, S. Ragazzi^{a,b}, N. Redaelli^a, S. Sala^a, T. Tabarelli de Fatis^{a,b}

INFN Sezione di Napoli ^a, Università di Napoli "Federico II" ^b, Napoli, Italy

S. Buontempo^a, C.A. Carrillo Montoya^a, N. Cavallo^{a,26}, A. De Cosa^{a,b,5}, O. Dogangun^{a,b}, F. Fabozzi^{a,26}, A.O.M. Iorio^a, L. Lista^a, S. Meola^{a,27}, M. Merola^{a,b}, P. Paolucci^{a,5}

INFN Sezione di Padova ^a, Università di Padova ^b, Università di Trento (Trento) ^c, Padova, Italy

P. Azzi^a, N. Bacchetta^{a,5}, D. Bisello^{a,b}, A. Branca^{a,b,5}, R. Carlin^{a,b}, P. Checchia^a, T. Dorigo^a, U. Dosselli^a, F. Gasparini^{a,b}, U. Gasparini^{a,b}, A. Gozzelino^a, K. Kanishchev^{a,c}, S. Lacaprara^a, I. Lazzizzera^{a,c}, M. Margoni^{a,b}, A.T. Meneguzzo^{a,b}, J. Pazzini^{a,b}, N. Pozzobon^{a,b}, P. Ronchese^{a,b}, F. Simonetto^{a,b}, E. Torassa^a, M. Tosi^{a,b,5}, S. Vanini^{a,b}, P. Zotto^{a,b}, G. Zumerle^{a,b}

INFN Sezione di Pavia ^a, Università di Pavia ^b, Pavia, Italy

M. Gabusi^{a,b}, S.P. Ratti^{a,b}, C. Riccardi^{a,b}, P. Torre^{a,b}, P. Vitulo^{a,b}

INFN Sezione di Perugia ^a, Università di Perugia ^b, Perugia, Italy

M. Biasini^{a,b}, G.M. Bilei^a, L. Fanò^{a,b}, P. Lariccia^{a,b}, A. Lucaroni^{a,b,5}, G. Mantovani^{a,b}, M. Menichelli^a, A. Nappi^{a,b†}, F. Romeo^{a,b}, A. Saha^a, A. Santocchia^{a,b}, A. Spiezia^{a,b}, S. Taroni^{a,b}

INFN Sezione di Pisa ^a, Università di Pisa ^b, Scuola Normale Superiore di Pisa ^c, Pisa, Italy

P. Azzurri^{a,c}, G. Bagliesi^a, J. Bernardini^a, T. Boccali^a, G. Broccolo^{a,c}, R. Castaldi^a, R.T. D'Agnolo^{a,c}, R. Dell'Orso^a, F. Fiori^{a,b,5}, L. Foà^{a,c}, A. Giassi^a, A. Kraan^a, F. Ligabue^{a,c}, T. Lomtadze^a, L. Martini^{a,28},

A. Messineo^{a,b}, F. Palla^a, A. Rizzi^{a,b}, A.T. Serban^{a,29}, P. Spagnolo^a, P. Squillacioti^{a,5}, R. Tenchini^a, G. Tonelli^{a,b,5}, A. Venturi^a, P.G. Verdini^a

INFN Sezione di Roma ^a, Università di Roma ^b, Roma, Italy

L. Barone^{a,b}, F. Cavallari^a, D. Del Re^{a,b}, M. Diemoz^a, C. Fanelli^{a,b}, M. Grassi^{a,b,5}, E. Longo^{a,b}, P. Meridiani^{a,5}, F. Micheli^{a,b}, S. Nourbakhsh^{a,b}, G. Organtini^{a,b}, R. Paramatti^a, S. Rahatlou^{a,b}, M. Sigamani^a, L. Soffi^{a,b}

INFN Sezione di Torino ^a, Università di Torino ^b, Università del Piemonte Orientale (Novara) ^c, Torino, Italy

N. Amapane^{a,b}, R. Arcidiacono^{a,c}, S. Argiro^{a,b}, M. Arneodo^{a,c}, C. Biino^a, N. Cartiglia^a, M. Costa^{a,b}, N. Demaria^a, C. Mariotti^{a,5}, S. Maselli^a, G. Mazza^a, E. Migliore^{a,b}, V. Monaco^{a,b}, M. Musich^{a,5}, M.M. Obertino^{a,c}, N. Pastrone^a, M. Pelliccioni^a, A. Potenza^{a,b}, A. Romero^{a,b}, R. Sacchi^{a,b}, A. Solano^{a,b}, A. Staiano^a, A. Vilela Pereira^a

INFN Sezione di Trieste ^a, Università di Trieste ^b, Trieste, Italy

S. Belforte^a, V. Candelise^{a,b}, F. Cossutti^a, G. Della Ricca^{a,b}, B. Gobbo^a, M. Marone^{a,b,5}, D. Montanino^{a,b,5}, A. Penzo^a, A. Schizzi^{a,b}

Kangwon National University, Chunchon, Korea

S.G. Heo, T.Y. Kim, S.K. Nam

Kyungpook National University, Daegu, Korea

S. Chang, D.H. Kim, G.N. Kim, D.J. Kong, H. Park, S.R. Ro, D.C. Son, T. Son

Chonnam National University, Institute for Universe and Elementary Particles, Kwangju, Korea

J.Y. Kim, Zero J. Kim, S. Song

Korea University, Seoul, Korea

S. Choi, D. Gyun, B. Hong, M. Jo, H. Kim, T.J. Kim, K.S. Lee, D.H. Moon, S.K. Park

University of Seoul, Seoul, Korea

M. Choi, J.H. Kim, C. Park, I.C. Park, S. Park, G. Ryu

Sungkyunkwan University, Suwon, Korea

Y. Cho, Y. Choi, Y.K. Choi, J. Goh, M.S. Kim, E. Kwon, B. Lee, J. Lee, S. Lee, H. Seo, I. Yu

Vilnius University, Vilnius, Lithuania

M.J. Bilinskas, I. Grigelionis, M. Janulis, A. Juodagalvis

Centro de Investigacion y de Estudios Avanzados del IPN, Mexico City, Mexico

H. Castilla-Valdez, E. De La Cruz-Burelo, I. Heredia-de La Cruz, R. Lopez-Fernandez, R. Magaña Villalba, J. Martínez-Ortega, A. Sánchez-Hernández, L.M. Villaseñor-Cendejas

Universidad Iberoamericana, Mexico City, Mexico

S. Carrillo Moreno, F. Vazquez Valencia

Benemerita Universidad Autonoma de Puebla, Puebla, Mexico

H.A. Salazar Ibarguen

Universidad Autónoma de San Luis Potosí, San Luis Potosí, Mexico

E. Casimiro Linares, A. Morelos Pineda, M.A. Reyes-Santos

University of Auckland, Auckland, New Zealand

D. Krofcheck

University of Canterbury, Christchurch, New Zealand

A.J. Bell, P.H. Butler, R. Doesburg, S. Reucroft, H. Silverwood

National Centre for Physics, Quaid-I-Azam University, Islamabad, Pakistan

M. Ahmad, M.H. Ansari, M.I. Asghar, H.R. Hoorani, S. Khalid, W.A. Khan, T. Khurshid, S. Qazi, M.A. Shah, M. Shoaib

National Centre for Nuclear Research, Swierk, Poland

H. Bialkowska, B. Boimska, T. Frueboes, R. Gokieli, M. Górski, M. Kazana, K. Nawrocki, K. Romanowska-Rybinska, M. Szeleper, G. Wrochna, P. Zalewski

Institute of Experimental Physics, Faculty of Physics, University of Warsaw, Warsaw, Poland

G. Brona, K. Bunkowski, M. Cwiok, W. Dominik, K. Doroba, A. Kalinowski, M. Konecki, J. Krolikowski

Laboratório de Instrumentação e Física Experimental de Partículas, Lisboa, Portugal

N. Almeida, P. Bargassa, A. David, P. Faccioli, P.G. Ferreira Parracho, M. Gallinaro, J. Seixas, J. Varela, P. Vischia

Joint Institute for Nuclear Research, Dubna, Russia

I. Belotelov, P. Bunin, M. Gavrilenko, I. Golutvin, I. Gorbunov, A. Kamenev, V. Karjavin, G. Kozlov, A. Lanev, A. Malakhov, P. Moisenz, V. Palichik, V. Perelygin, S. Shmatov, V. Smirnov, A. Volodko, A. Zarubin

Petersburg Nuclear Physics Institute, Gatchina (St. Petersburg), Russia

S. Evstyukhin, V. Golovtsov, Y. Ivanov, V. Kim, P. Levchenko, V. Murzin, V. Oreshkin, I. Smirnov, V. Sulimov, L. Uvarov, S. Vavilov, A. Vorobyev, An. Vorobyev

Institute for Nuclear Research, Moscow, Russia

Yu. Andreev, A. Dermenev, S. Gninenko, N. Golubev, M. Kirsanov, N. Krasnikov, V. Matveev, A. Pashenkov, D. Tlisov, A. Toropin

Institute for Theoretical and Experimental Physics, Moscow, Russia

V. Epshteyn, M. Erofeeva, V. Gavrilov, M. Kossov, N. Lychkovskaya, V. Popov, G. Safronov, S. Semenov, V. Stolin, E. Vlasov, A. Zhokin

Moscow State University, Moscow, RussiaA. Belyaev, E. Boos, M. Dubinin⁴, L. Dudko, A. Ershov, A. Gribushin, A. Kaminskiy³⁰, V. Klyukhin, O. Kodolova, I. Lokhtin, A. Markina, S. Obraztsov, M. Perfilov, S. Petrushanko, A. Popov, L. Sarycheva[†], V. Savrin**P.N. Lebedev Physical Institute, Moscow, Russia**

V. Andreev, M. Azarkin, I. Dremin, M. Kirakosyan, A. Leonidov, G. Mesyats, S.V. Rusakov, A. Vinogradov

State Research Center of Russian Federation, Institute for High Energy Physics, Protvino, RussiaI. Azhgirey, I. Bayshev, S. Bitioukov, V. Grishin⁵, V. Kachanov, D. Konstantinov, A. Korablev, V. Krychkine, V. Petrov, R. Ryutin, A. Sobol, L. Tourtchanovitch, S. Troshin, N. Tyurin, A. Uzunian, A. Volkov**University of Belgrade, Faculty of Physics and Vinca Institute of Nuclear Sciences, Belgrade, Serbia**P. Adzic³¹, M. Djordjevic, M. Ekmedzic, D. Krpic³¹, J. Milosevic

Centro de Investigaciones Energéticas Medioambientales y Tecnológicas (CIEMAT), Madrid, Spain

M. Aguilar-Benitez, J. Alcaraz Maestre, P. Arce, C. Battilana, E. Calvo, M. Cerrada, M. Chamizo Llatas, N. Colino, B. De La Cruz, A. Delgado Peris, D. Domínguez Vázquez, C. Fernandez Bedoya, J.P. Fernández Ramos, A. Ferrando, J. Flix, M.C. Fouz, P. Garcia-Abia, O. Gonzalez Lopez, S. Goy Lopez, J.M. Hernandez, M.I. Josa, G. Merino, J. Puerta Pelayo, A. Quintario Olmeda, I. Redondo, L. Romero, J. Santaolalla, M.S. Soares, C. Willmott

Universidad Autónoma de Madrid, Madrid, Spain

C. Albajar, G. Codispoti, J.F. de Trocóniz

Universidad de Oviedo, Oviedo, Spain

H. Brun, J. Cuevas, J. Fernandez Menendez, S. Folgueras, I. Gonzalez Caballero, L. Lloret Iglesias, J. Piedra Gomez

Instituto de Física de Cantabria (IFCA), CSIC-Universidad de Cantabria, Santander, Spain

J.A. Brochero Cifuentes, I.J. Cabrillo, A. Calderon, S.H. Chuang, J. Duarte Campderros, M. Felcini³², M. Fernandez, G. Gomez, J. Gonzalez Sanchez, A. Graziano, C. Jorda, A. Lopez Virto, J. Marco, R. Marco, C. Martinez Rivero, F. Matorras, F.J. Munoz Sanchez, T. Rodrigo, A.Y. Rodríguez-Marrero, A. Ruiz-Jimeno, L. Scodellaro, M. Sobron Sanudo, I. Vila, R. Vilar Cortabitarte

CERN, European Organization for Nuclear Research, Geneva, Switzerland

D. Abbaneo, E. Auffray, G. Auzinger, P. Baillon, A.H. Ball, D. Barney, J.F. Benitez, C. Bernet⁶, G. Bianchi, P. Bloch, A. Bocci, A. Bonato, C. Botta, H. Breuker, T. Camporesi, G. Cerminara, T. Christiansen, J.A. Coarasa Perez, D. D'Enterria, A. Dabrowski, A. De Roeck, S. Di Guida, M. Dobson, N. Dupont-Sagorin, A. Elliott-Peisert, B. Frisch, W. Funk, G. Georgiou, M. Giffels, D. Gigi, K. Gill, D. Giordano, M. Giunta, F. Glege, R. Gomez-Reino Garrido, P. Govoni, S. Gowdy, R. Guida, M. Hansen, P. Harris, C. Hartl, J. Harvey, B. Hegner, A. Hinzmann, V. Innocente, P. Janot, K. Kaadze, E. Karavakis, K. Kousouris, P. Lecoq, Y.-J. Lee, P. Lenzi, C. Lourenço, T. Mäki, M. Malberti, L. Malgeri, M. Mannelli, L. Masetti, F. Meijers, S. Mersi, E. Meschi, R. Moser, M.U. Mozer, M. Mulders, P. Musella, E. Nesvold, T. Orimoto, L. Orsini, E. Palencia Cortezon, E. Perez, L. Perrozzi, A. Petrilli, A. Pfeiffer, M. Pierini, M. Pimiä, D. Piparo, G. Polese, L. Quertenmont, A. Racz, W. Reece, J. Rodrigues Antunes, G. Rolandi³³, C. Rovelli³⁴, M. Rovere, H. Sakulin, F. Santanastasio, C. Schäfer, C. Schwick, I. Segoni, S. Sekmen, A. Sharma, P. Siegrist, P. Silva, M. Simon, P. Sphicas³⁵, D. Spiga, A. Tsirou, G.I. Veres¹⁹, J.R. Vlimant, H.K. Wöhri, S.D. Worm³⁶, W.D. Zeuner

Paul Scherrer Institut, Villigen, Switzerland

W. Bertl, K. Deiters, W. Erdmann, K. Gabathuler, R. Horisberger, Q. Ingram, H.C. Kaestli, S. König, D. Kotlinski, U. Langenegger, F. Meier, D. Renker, T. Rohe, J. Sibille³⁷

Institute for Particle Physics, ETH Zurich, Zurich, Switzerland

L. Bäni, P. Bortignon, M.A. Buchmann, B. Casal, N. Chanon, A. Deisher, G. Dissertori, M. Dittmar, M. Donegà, M. Dünser, J. Eugster, K. Freudenreich, C. Grab, D. Hits, P. Lecomte, W. Lustermann, A.C. Marini, P. Martinez Ruiz del Arbol, N. Mohr, F. Moortgat, C. Nägeli³⁸, P. Nef, F. Nessi-Tedaldi, F. Pandolfi, L. Pape, F. Pauss, M. Peruzzi, F.J. Ronga, M. Rossini, L. Sala, A.K. Sanchez, A. Starodumov³⁹, B. Stieger, M. Takahashi, L. Tauscher[†], A. Thea, K. Theofilatos, D. Treille, C. Urscheler, R. Wallny, H.A. Weber, L. Wehrli

Universität Zürich, Zurich, Switzerland

C. AMSLER, V. Chiochia, S. De Visscher, C. Favaro, M. Ivova Rikova, B. Millan Mejias, P. Otiougova, P. Robmann, H. Snoek, S. Tuppeuti, M. Verzetti

National Central University, Chung-Li, Taiwan

Y.H. Chang, K.H. Chen, C.M. Kuo, S.W. Li, W. Lin, Z.K. Liu, Y.J. Lu, D. Mekterovic, A.P. Singh, R. Volpe, S.S. Yu

National Taiwan University (NTU), Taipei, Taiwan

P. Bartalini, P. Chang, Y.H. Chang, Y.W. Chang, Y. Chao, K.F. Chen, C. Dietz, U. Grundler, W.-S. Hou, Y. Hsiung, K.Y. Kao, Y.J. Lei, R.-S. Lu, D. Majumder, E. Petrakou, X. Shi, J.G. Shiu, Y.M. Tzeng, X. Wan, M. Wang

Cukurova University, Adana, Turkey

A. Adiguzel, M.N. Bakirci⁴⁰, S. Cerci⁴¹, C. Dozen, I. Dumanoglu, E. Eskut, S. Girgis, G. Gokbulut, E. Gurpinar, I. Hos, E.E. Kangal, T. Karaman, G. Karapinar⁴², A. Kayis Topaksu, G. Onengut, K. Ozdemir, S. Ozturk⁴³, A. Polatoz, K. Sogut⁴⁴, D. Sunar Cerci⁴¹, B. Tali⁴¹, H. Topakli⁴⁰, L.N. Vergili, M. Vergili

Middle East Technical University, Physics Department, Ankara, Turkey

I.V. Akin, T. Aliev, B. Bilin, S. Bilmis, M. Deniz, H. Gamsizkan, A.M. Guler, K. Ocalan, A. Ozpineci, M. Serin, R. Sever, U.E. Surat, M. Yalvac, E. Yildirim, M. Zeyrek

Bogazici University, Istanbul, Turkey

E. Gülmez, B. Isildak⁴⁵, M. Kaya⁴⁶, O. Kaya⁴⁶, S. Ozkorucuklu⁴⁷, N. Sonmez⁴⁸

Istanbul Technical University, Istanbul, Turkey

K. Cankocak

National Scientific Center, Kharkov Institute of Physics and Technology, Kharkov, Ukraine

L. Levchuk

University of Bristol, Bristol, United Kingdom

F. Bostock, J.J. Brooke, E. Clement, D. Cussans, H. Flacher, R. Frazier, J. Goldstein, M. Grimes, G.P. Heath, H.F. Heath, L. Kreczko, S. Metson, D.M. Newbold³⁶, K. Nirunpong, A. Poll, S. Senkin, V.J. Smith, T. Williams

Rutherford Appleton Laboratory, Didcot, United Kingdom

L. Basso⁴⁹, K.W. Bell, A. Belyaev⁴⁹, C. Brew, R.M. Brown, D.J.A. Cockerill, J.A. Coughlan, K. Harder, S. Harper, J. Jackson, B.W. Kennedy, E. Olaiya, D. Petyt, B.C. Radburn-Smith, C.H. Shepherd-Themistocleous, I.R. Tomalin, W.J. Womersley

Imperial College, London, United Kingdom

R. Bainbridge, G. Ball, R. Beuselinck, O. Buchmuller, D. Colling, N. Cripps, M. Cutajar, P. Dauncey, G. Davies, M. Della Negra, W. Ferguson, J. Fulcher, D. Futyan, A. Gilbert, A. Guneratne Bryer, G. Hall, Z. Hatherell, J. Hays, G. Iles, M. Jarvis, G. Karapostoli, L. Lyons, A.-M. Magnan, J. Marrouche, B. Mathias, R. Nandi, J. Nash, A. Nikitenko³⁹, A. Papageorgiou, J. Pela, M. Pesaresi, K. Petridis, M. Pioppi⁵⁰, D.M. Raymond, S. Rogerson, A. Rose, M.J. Ryan, C. Seez, P. Sharp[†], A. Sparrow, M. Stoye, A. Tapper, M. Vazquez Acosta, T. Virdee, S. Wakefield, N. Wardle, T. Whyntie

Brunel University, Uxbridge, United Kingdom

M. Chadwick, J.E. Cole, P.R. Hobson, A. Khan, P. Kyberd, D. Leggat, D. Leslie, W. Martin, I.D. Reid, P. Symonds, L. Teodorescu, M. Turner

Baylor University, Waco, USA

K. Hatakeyama, H. Liu, T. Scarborough

The University of Alabama, Tuscaloosa, USA

O. Charaf, C. Henderson, P. Rumerio

Boston University, Boston, USA

A. Avetisyan, T. Bose, C. Fantasia, A. Heister, J. St. John, P. Lawson, D. Lazic, J. Rohlf, D. Sperka, L. Sulak

Brown University, Providence, USA

J. Alimena, S. Bhattacharya, D. Cutts, A. Ferapontov, U. Heintz, S. Jabeen, G. Kukartsev, E. Laird, G. Landsberg, M. Luk, M. Narain, D. Nguyen, M. Segala, T. Sinthuprasith, T. Speer, K.V. Tsang

University of California, Davis, Davis, USA

R. Breedon, G. Breto, M. Calderon De La Barca Sanchez, S. Chauhan, M. Chertok, J. Conway, R. Conway, P.T. Cox, J. Dolen, R. Erbacher, M. Gardner, R. Houtz, W. Ko, A. Kopecky, R. Lander, T. Miceli, D. Pellett, F. Ricci-Tam, B. Rutherford, M. Searle, J. Smith, M. Squires, M. Tripathi, R. Vasquez Sierra

University of California, Los Angeles, Los Angeles, USA

V. Andreev, D. Cline, R. Cousins, J. Duris, S. Erhan, P. Everaerts, C. Farrell, J. Hauser, M. Ignatenko, C. Jarvis, C. Plager, G. Rakness, P. Schlein[†], P. Traczyk, V. Valuev, M. Weber

University of California, Riverside, Riverside, USA

J. Babb, R. Clare, M.E. Dinardo, J. Ellison, J.W. Gary, F. Giordano, G. Hanson, G.Y. Jeng⁵¹, H. Liu, O.R. Long, A. Luthra, H. Nguyen, S. Paramesvaran, J. Sturdy, S. Sumowidagdo, R. Wilken, S. Wimpenny

University of California, San Diego, La Jolla, USA

W. Andrews, J.G. Branson, G.B. Cerati, S. Cittolin, D. Evans, F. Golf, A. Holzner, R. Kelley, M. Lebourgeois, J. Letts, I. Macneill, B. Mangano, S. Padhi, C. Palmer, G. Petrucciani, M. Pieri, M. Sani, V. Sharma, S. Simon, E. Sudano, M. Tadel, Y. Tu, A. Vartak, S. Wasserbaech⁵², F. Würthwein, A. Yagil, J. Yoo

University of California, Santa Barbara, Santa Barbara, USA

D. Barge, R. Bellan, C. Campagnari, M. D'Alfonso, T. Danielson, K. Flowers, P. Geffert, J. Incandela, C. Justus, P. Kalavase, S.A. Koay, D. Kovalskyi, V. Krutelyov, S. Lowette, N. Mccoll, V. Pavlunin, F. Rebassoo, J. Ribnik, J. Richman, R. Rossin, D. Stuart, W. To, C. West

California Institute of Technology, Pasadena, USA

A. Apresyan, A. Bornheim, Y. Chen, E. Di Marco, J. Duarte, M. Gataullin, Y. Ma, A. Mott, H.B. Newman, C. Rogan, M. Spiropulu, V. Timciuc, J. Veverka, R. Wilkinson, S. Xie, Y. Yang, R.Y. Zhu

Carnegie Mellon University, Pittsburgh, USA

B. Akgun, V. Azzolini, A. Calamba, R. Carroll, T. Ferguson, Y. Iiyama, D.W. Jang, Y.F. Liu, M. Paulini, H. Vogel, I. Vorobiev

University of Colorado at Boulder, Boulder, USA

J.P. Cumalat, B.R. Drell, C.J. Edelmaier, W.T. Ford, A. Gaz, B. Heyburn, E. Luigi Lopez, J.G. Smith, K. Stenson, K.A. Ulmer, S.R. Wagner

Cornell University, Ithaca, USA

J. Alexander, A. Chatterjee, N. Eggert, L.K. Gibbons, B. Heltsley, A. Khukhunaishvili, B. Kreis, N. Mirman, G. Nicolas Kaufman, J.R. Patterson, A. Ryd, E. Salvati, W. Sun, W.D. Teo, J. Thom, J. Thompson, J. Tucker, J. Vaughan, Y. Weng, L. Winstrom, P. Wittich

Fairfield University, Fairfield, USA

D. Winn

Fermi National Accelerator Laboratory, Batavia, USA

S. Abdullin, M. Albrow, J. Anderson, L.A.T. Bauerdick, A. Beretvas, J. Berryhill, P.C. Bhat, I. Bloch, K. Burkett, J.N. Butler, V. Chetluru, H.W.K. Cheung, F. Chlebana, V.D. Elvira, I. Fisk, J. Freeman, Y. Gao, D. Green, O. Gutsche, J. Hanlon, R.M. Harris, J. Hirschauer, B. Hooberman, S. Jindariani, M. Johnson, U. Joshi, B. Kilminster, B. Klima, S. Kunori, S. Kwan, C. Leonidopoulos, J. Linacre, D. Lincoln, R. Lipton, J. Lykken, K. Maeshima, J.M. Marraffino, S. Maruyama, D. Mason, P. McBride, K. Mishra, S. Mrenna, Y. Musienko⁵³, C. Newman-Holmes, V. O'Dell, O. Prokofyev, E. Sexton-Kennedy, S. Sharma, W.J. Spalding, L. Spiegel, P. Tan, L. Taylor, S. Tkaczyk, N.V. Tran, L. Uplegger, E.W. Vaandering, R. Vidal, J. Whitmore, W. Wu, F. Yang, F. Yumiceva, J.C. Yun

University of Florida, Gainesville, USA

D. Acosta, P. Avery, D. Bourilkov, M. Chen, T. Cheng, S. Das, M. De Gruttola, G.P. Di Giovanni, D. Dobur, A. Drozdetskiy, R.D. Field, M. Fisher, Y. Fu, I.K. Furic, J. Gartner, J. Hugon, B. Kim, J. Konigsberg, A. Korytov, A. Kropivnitskaya, T. Kypreos, J.F. Low, K. Matchev, P. Milenovic⁵⁴, G. Mitselmakher, L. Muniz, R. Remington, A. Rinkevicius, P. Sellers, N. Skhirtladze, M. Snowball, J. Yelton, M. Zakaria

Florida International University, Miami, USA

V. Gaultney, S. Hewamanage, L.M. Lebolo, S. Linn, P. Markowitz, G. Martinez, J.L. Rodriguez

Florida State University, Tallahassee, USA

T. Adams, A. Askew, J. Bochenek, J. Chen, B. Diamond, S.V. Gleyzer, J. Haas, S. Hagopian, V. Hagopian, M. Jenkins, K.F. Johnson, H. Prosper, V. Veeraraghavan, M. Weinberg

Florida Institute of Technology, Melbourne, USA

M.M. Baarmand, B. Dorney, M. Hohlmann, H. Kalakhety, I. Vodopyanov

University of Illinois at Chicago (UIC), Chicago, USA

M.R. Adams, I.M. Anghel, L. Apanasevich, Y. Bai, V.E. Bazterra, R.R. Betts, I. Bucinskaite, J. Callner, R. Cavanaugh, C. Dragoiu, O. Evdokimov, L. Gauthier, C.E. Gerber, D.J. Hofman, S. Khalatyan, F. Lacroix, M. Malek, C. O'Brien, C. Silkworth, D. Strom, N. Varelas

The University of Iowa, Iowa City, USA

U. Akgun, E.A. Albayrak, B. Bilki⁵⁵, W. Clarida, F. Duru, S. Griffiths, J.-P. Merlo, H. Mermerkaya⁵⁶, A. Mestvirishvili, A. Moeller, J. Nachtman, C.R. Newsom, E. Norbeck, Y. Onel, F. Ozok, S. Sen, E. Tiras, J. Wetzel, T. Yetkin, K. Yi

Johns Hopkins University, Baltimore, USA

B.A. Barnett, B. Blumenfeld, S. Bolognesi, D. Fehling, G. Giurgiu, A.V. Gritsan, Z.J. Guo, G. Hu, P. Maksimovic, S. Rappoccio, M. Swartz, A. Whitbeck

The University of Kansas, Lawrence, USA

P. Baringer, A. Bean, G. Benelli, O. Grachov, R.P. Kenny Iii, M. Murray, D. Noonan, S. Sanders, R. Stringer, G. Tinti, J.S. Wood, V. Zhukova

Kansas State University, Manhattan, USA

A.F. Barfuss, T. Bolton, I. Chakaberia, A. Ivanov, S. Khalil, M. Makouski, Y. Maravin, S. Shrestha, I. Svintradze

Lawrence Livermore National Laboratory, Livermore, USA

J. Gronberg, D. Lange, D. Wright

University of Maryland, College Park, USA

A. Baden, M. Boutemur, B. Calvert, S.C. Eno, J.A. Gomez, N.J. Hadley, R.G. Kellogg, M. Kirn, T. Kolberg, Y. Lu, M. Marionneau, A.C. Mignerey, K. Pedro, A. Peterman, A. Skuja, J. Temple, M.B. Tonjes, S.C. Tonwar, E. Twedt

Massachusetts Institute of Technology, Cambridge, USA

A. Apyan, G. Bauer, J. Bendavid, W. Busza, E. Butz, I.A. Cali, M. Chan, V. Dutta, G. Gomez Ceballos, M. Goncharov, K.A. Hahn, Y. Kim, M. Klute, K. Krajczar⁵⁷, W. Li, P.D. Luckey, T. Ma, S. Nahn, C. Paus, D. Ralph, C. Roland, G. Roland, M. Rudolph, G.S.F. Stephans, F. Stöckli, K. Sumorok, K. Sung, D. Velicanu, E.A. Wenger, R. Wolf, B. Wyslouch, M. Yang, Y. Yilmaz, A.S. Yoon, M. Zanetti

University of Minnesota, Minneapolis, USA

S.I. Cooper, B. Dahmes, A. De Benedetti, G. Franzoni, A. Gude, S.C. Kao, K. Klapoetke, Y. Kubota, J. Mans, N. Pastika, R. Rusack, M. Sasseville, A. Singovsky, N. Tambe, J. Turkewitz

University of Mississippi, Oxford, USA

L.M. Cremaldi, R. Kroeger, L. Perera, R. Rahmat, D.A. Sanders

University of Nebraska-Lincoln, Lincoln, USA

E. Avdeeva, K. Bloom, S. Bose, J. Butt, D.R. Claes, A. Dominguez, M. Eads, J. Keller, I. Kravchenko, J. Lazo-Flores, H. Malbouissou, S. Malik, G.R. Snow

State University of New York at Buffalo, Buffalo, USA

U. Baur, A. Godshalk, I. Iashvili, S. Jain, A. Kharchilava, A. Kumar, S.P. Shipkowski, K. Smith

Northeastern University, Boston, USA

G. Alverson, E. Barberis, D. Baumgartel, M. Chasco, J. Haley, D. Nash, D. Trocino, D. Wood, J. Zhang

Northwestern University, Evanston, USA

A. Anastassov, A. Kubik, N. Mucia, N. Odell, R.A. Ofierzynski, B. Pollack, A. Pozdnyakov, M. Schmitt, S. Stoynev, M. Velasco, S. Won

University of Notre Dame, Notre Dame, USA

L. Antonelli, D. Berry, A. Brinkerhoff, M. Hildreth, C. Jessop, D.J. Karmgard, J. Kolb, K. Lannon, W. Luo, S. Lynch, N. Marinelli, D.M. Morse, T. Pearson, M. Planer, R. Ruchti, J. Slaunwhite, N. Valls, M. Wayne, M. Wolf

The Ohio State University, Columbus, USA

B. Bylsma, L.S. Durkin, C. Hill, R. Hughes, R. Hughes, K. Kotov, T.Y. Ling, D. Puigh, M. Rodenburg, C. Vuosalo, G. Williams, B.L. Winer

Princeton University, Princeton, USA

N. Adam, E. Berry, P. Elmer, D. Gerbaudo, V. Halyo, P. Hebda, J. Hegeman, A. Hunt, P. Jindal, D. Lopes Pegna, P. Lujan, D. Marlow, T. Medvedeva, M. Mooney, J. Olsen, P. Piroué, X. Quan, A. Raval, B. Safdi, H. Saka, D. Stickland, C. Tully, J.S. Werner, A. Zuranski

University of Puerto Rico, Mayaguez, USA

J.G. Acosta, E. Brownson, X.T. Huang, A. Lopez, H. Mendez, S. Oliveros, J.E. Ramirez Vargas, A. Zatserklyaniy

Purdue University, West Lafayette, USA

E. Alagoz, V.E. Barnes, D. Benedetti, G. Bolla, D. Bortoletto, M. De Mattia, A. Everett, Z. Hu, M. Jones, O. Koybasi, M. Kress, A.T. Laasanen, N. Leonardo, V. Maroussov, P. Merkel, D.H. Miller, N. Neumeister, I. Shipsey, D. Silvers, A. Svyatkovskiy, M. Vidal Marono, H.D. Yoo, J. Zablocki, Y. Zheng

Purdue University Calumet, Hammond, USA

S. Guragain, N. Parashar

Rice University, Houston, USA

A. Adair, C. Boulahouache, K.M. Ecklund, F.J.M. Geurts, B.P. Padley, R. Redjimi, J. Roberts, J. Zabel

University of Rochester, Rochester, USA

B. Betchart, A. Bodek, Y.S. Chung, R. Covarelli, P. de Barbaro, R. Demina, Y. Eshaq, A. Garcia-Bellido, P. Goldenzweig, J. Han, A. Harel, D.C. Miner, D. Vishnevskiy, M. Zielinski

The Rockefeller University, New York, USA

A. Bhatti, R. Ciesielski, L. Demortier, K. Goulianos, G. Lungu, S. Malik, C. Mesropian

Rutgers, the State University of New Jersey, Piscataway, USA

S. Arora, A. Barker, J.P. Chou, C. Contreras-Campana, E. Contreras-Campana, D. Duggan, D. Ferencek, Y. Gershtein, R. Gray, E. Halkiadakis, D. Hidas, A. Lath, S. Panwalkar, M. Park, R. Patel, V. Rekovic, J. Robles, K. Rose, S. Salur, S. Schnetzer, C. Seitz, S. Somalwar, R. Stone, S. Thomas

University of Tennessee, Knoxville, USA

G. Cerizza, M. Hollingsworth, S. Spanier, Z.C. Yang, A. York

Texas A&M University, College Station, USA

R. Eusebi, W. Flanagan, J. Gilmore, T. Kamon⁵⁸, V. Khotilovich, R. Montalvo, I. Osipenko, Y. Pakhotin, A. Perloff, J. Roe, A. Safonov, T. Sakuma, S. Sengupta, I. Suarez, A. Tatarinov, D. Toback

Texas Tech University, Lubbock, USA

N. Akchurin, J. Damgov, P.R. Duder, C. Jeong, K. Kovitanggoon, S.W. Lee, T. Libeiro, Y. Roh, I. Volobouev

Vanderbilt University, Nashville, USA

E. Appelt, A.G. Delannoy, C. Florez, S. Greene, A. Gurrola, W. Johns, C. Johnston, P. Kurt, C. Maguire, A. Melo, M. Sharma, P. Sheldon, B. Snook, S. Tuo, J. Velkovska

University of Virginia, Charlottesville, USA

M.W. Arenton, M. Balazs, S. Boutle, B. Cox, B. Francis, J. Goodell, R. Hirosky, A. Ledovskoy, C. Lin, C. Neu, J. Wood, R. Yohay

Wayne State University, Detroit, USA

S. Gollapinni, R. Harr, P.E. Karchin, C. Kottachchi Kankanamge Don, P. Lamichhane, A. Sakharov

University of Wisconsin, Madison, USA

M. Anderson, M. Bachtis, D. Belknap, L. Borrello, D. Carlsmith, M. Cepeda, S. Dasu, E. Friis, L. Gray, K.S. Grogg, M. Grothe, R. Hall-Wilton, M. Herndon, A. Hervé, P. Klabbers, J. Klukas, A. Lanaro, C. Lazaridis, J. Leonard, R. Loveless, A. Mohapatra, I. Ojalvo, F. Palmonari, G.A. Pierro, I. Ross, A. Savin, W.H. Smith, J. Swanson

†: Deceased

1: Also at Vienna University of Technology, Vienna, Austria

2: Also at National Institute of Chemical Physics and Biophysics, Tallinn, Estonia

3: Also at Universidade Federal do ABC, Santo Andre, Brazil

4: Also at California Institute of Technology, Pasadena, USA

5: Also at CERN, European Organization for Nuclear Research, Geneva, Switzerland

- 6: Also at Laboratoire Leprince-Ringuet, Ecole Polytechnique, IN2P3-CNRS, Palaiseau, France
- 7: Also at Suez Canal University, Suez, Egypt
- 8: Also at Zewail City of Science and Technology, Zewail, Egypt
- 9: Also at Cairo University, Cairo, Egypt
- 10: Also at Fayoum University, El-Fayoum, Egypt
- 11: Also at British University in Egypt, Cairo, Egypt
- 12: Now at Ain Shams University, Cairo, Egypt
- 13: Also at National Centre for Nuclear Research, Swierk, Poland
- 14: Also at Université de Haute-Alsace, Mulhouse, France
- 15: Now at Joint Institute for Nuclear Research, Dubna, Russia
- 16: Also at Moscow State University, Moscow, Russia
- 17: Also at Brandenburg University of Technology, Cottbus, Germany
- 18: Also at Institute of Nuclear Research ATOMKI, Debrecen, Hungary
- 19: Also at Eötvös Loránd University, Budapest, Hungary
- 20: Also at Tata Institute of Fundamental Research - HECR, Mumbai, India
- 21: Also at University of Visva-Bharati, Santiniketan, India
- 22: Also at Sharif University of Technology, Tehran, Iran
- 23: Also at Isfahan University of Technology, Isfahan, Iran
- 24: Also at Plasma Physics Research Center, Science and Research Branch, Islamic Azad University, Tehran, Iran
- 25: Also at Facoltà Ingegneria, Università di Roma, Roma, Italy
- 26: Also at Università della Basilicata, Potenza, Italy
- 27: Also at Università degli Studi Guglielmo Marconi, Roma, Italy
- 28: Also at Università degli Studi di Siena, Siena, Italy
- 29: Also at University of Bucharest, Faculty of Physics, Bucuresti-Magurele, Romania
- 30: Also at INFN Sezione di Padova; Università di Padova; Università di Trento (Trento), Padova, Italy
- 31: Also at Faculty of Physics of University of Belgrade, Belgrade, Serbia
- 32: Also at University of California, Los Angeles, Los Angeles, USA
- 33: Also at Scuola Normale e Sezione dell'INFN, Pisa, Italy
- 34: Also at INFN Sezione di Roma; Università di Roma, Roma, Italy
- 35: Also at University of Athens, Athens, Greece
- 36: Also at Rutherford Appleton Laboratory, Didcot, United Kingdom
- 37: Also at The University of Kansas, Lawrence, USA
- 38: Also at Paul Scherrer Institut, Villigen, Switzerland
- 39: Also at Institute for Theoretical and Experimental Physics, Moscow, Russia
- 40: Also at Gaziosmanpasa University, Tokat, Turkey
- 41: Also at Adiyaman University, Adiyaman, Turkey
- 42: Also at Izmir Institute of Technology, Izmir, Turkey
- 43: Also at The University of Iowa, Iowa City, USA
- 44: Also at Mersin University, Mersin, Turkey
- 45: Also at Ozyegin University, Istanbul, Turkey
- 46: Also at Kafkas University, Kars, Turkey
- 47: Also at Suleyman Demirel University, Isparta, Turkey
- 48: Also at Ege University, Izmir, Turkey
- 49: Also at School of Physics and Astronomy, University of Southampton, Southampton, United Kingdom
- 50: Also at INFN Sezione di Perugia; Università di Perugia, Perugia, Italy
- 51: Also at University of Sydney, Sydney, Australia
- 52: Also at Utah Valley University, Orem, USA
- 53: Also at Institute for Nuclear Research, Moscow, Russia
- 54: Also at University of Belgrade, Faculty of Physics and Vinca Institute of Nuclear Sciences, Belgrade, Serbia
- 55: Also at Argonne National Laboratory, Argonne, USA
- 56: Also at Erzincan University, Erzincan, Turkey
- 57: Also at KFKI Research Institute for Particle and Nuclear Physics, Budapest, Hungary
- 58: Also at Kyungpook National University, Daegu, Korea